Preparation, Processing and Characterization of Noble Metal Nanoparticle-based Aerogels

Dissertation

zur Erlangung des akademischen Grades

Doctor rerum naturalium
(Dr. rer. nat.)

vorgelegt

der Fakultät Mathematik und Naturwissenschaften
der Technischen Universität Dresden

von

M.Sc. Anne-Kristin Herrmann

geboren am 03. Juni 1986 in Altdöbern

Tag der Verteidigung: 10.07.2014

Gutachter: Prof. Dr. rer. nat. habil. Alexander Eychmüller
              Prof. Dr. rer. nat. habil. Stefan Kaskel

Contents

Bibliography   **110**

Danksagung   **121**

Erklärung   **123**

Abbreviations

ADF . . . . annular dark field
APTMS . . . . (3-aminopropyl)trimethoxysilane
BET . . . . Brunauer-Emmett-Teller
BF . . . . bright-field
BJH . . . . Barrett-Joyner-Halenda
DFT . . . . density functional theory
DMAP 4-dimethylaminopyridine
EAXFS . . . . extended X-ray absorption fine structure
EDTA . . . . ethylenediaminetetraacetic acid
EDX . . . . energy-dispersive X-ray spectroscopy
EELS . . . . electron energy-loss spectroscopy
EFTEM . . . . energy-filtered transmission electron microscopy
EM . . . . electron microscopy
FIB . . . . focused ion beam
HAADF . . . . high angle annular dark field
HRTEM . . . . high resolution transmission electron microscopy
MMA . . . . methyl methacrylate
MPA . . . . 3-mercaptopropionic acid
MWCO . . . . molecular weight cut off
NP . . . . nanoparticle
PDDA . . . . polydiallyldimethylammonium chloride
QSDFT . . . . quenched solid density functional theory
SEM . . . . scanning electron microscopy
SERS . . . . surface-enhanced Raman scattering
SLS . . . . Swiss Light Source
SPR . . . . surface plasmon resonance
STEM . . . . scanning transmission electron microscopy
TEM . . . . transmission electron microscopy
TGA . . . . thermogravimetric analysis
XAFS . . . . X-ray absorption fine structure
XANES . . . . X-ray absorption near-edge structure
XAS . . . . X-ray absorption spectrum
XRD . . . . X-ray diffraction
ZT . . . . dimensionless figure of merit

List of Figures

List of Tables

Introduction

"There's plenty of room at the bottom" was the title of a famous talk given by RICHARD FEYNMAN in 1959 at the annual meeting of the American Physical Society.[1] There he talked about "the problem of manipulating and controlling things on a small scale" and he describes it as "a field, in which little has been done, but in which an enormous amount can be done in principle". His vision and "invitation to open up a new field of physics" has turned out to be impressively pioneering since nowadays the relatively young nanosciences are a versatile and extremely fast growing, multidisciplinary research field which leads to the development of new and innovative ideas.

One of the underlying basic tools of nanotechnology is the bottom up approach where the system develops from smaller building blocks to bigger and more complex structures. Particles in the small size of several nanometers are thereby produced through the chemical reaction of a limited number of molecular, atomic, or ionic entities under suitable conditions.[2] Numerous properties of the resulting nanoparticles (NPs) strongly depend on their composition, size, shape, functionalization, and crystallinity.[3,4] Hence, huge effort is made to manipulate and control these parameters by synthesis conditions and predict the properties of the resulting particles. In a next step these particles themselves can act as building blocks for two-dimensional or even three-dimensional assemblies. This is of great interest since synergetic collective properties and new possibilities for application can be created by the aligning of nanosized particles into ordered or nonordered superstructures. Nanocrystal superlattices and close packed nanocrystal solids obtained from NP assembly were first described in 1989 by BENTZON et al.[5] and became an intensively studied research field.[6–9] Moreover, attention is attracted by the investigation of self-organization based on electrostatic interaction,[10] nanocrystal formation via oriented attachment[11] and dynamic NP assemblies.[12]

Within this new class of materials three-dimensional porous nanostructures consisting of various functional metals are in the focus of research due to their high surface area, low relative density, size-effect-enhanced catalytic activity and plasmonic behavior as well as their electrical conductivity and gas permeability.[13,14] The exceptional performance of porous and nonordered nanoarchitectures in heterogeneous catalysis and electrocatalysis has already been discussed in the literature.[14,15] Further possible application fields are sensors, optical absorbing layers, surface-enhanced Raman scattering (SERS) substrates, conductive coatings, thermoelectric, microfluidic, and hydrogen storage materials. Hence, considerable challenges in the field of metallic nanomaterials arise in the development and improvement of techniques for the building up of complex multiscale architectures and their integration into usable devices. For these reasons, the present work focuses on the formation of monometallic and multimetallic, porous, three-dimensional networks by a template-free self-assembly process. Nanochains are formed by the controlled coalescence of noble metal NPs in aqueous media. Their interconnection and

interpenetration lead to the formation of a self-supporting network named hydrogel. Supercritical drying technique is used in order to transfer the materials into solid aerogels. Owing to the unique combination of nano and macro dimensions in one structure, gels and aerogels are supposed to have physicochemical properties different from their building blocks and from the corresponding bulk materials.

The variety of the state of the art techniques for the preparation of porous metals is summarized and discussed in Chapter 1. Moreover, the scope of NP-based aerogels, their evolution, material diversity and striking applications are presented. In order to underline their unique properties, metallic aerogels are classified and compared to other porous metals regarding inner surface area, density and pore size. Apart from monometallic nanostructures especially multimetallic, porous materials are of great importance and interest for many application fields. It is known from various examples that the combination of different metals leads to synergetic effects which could play a major role, for example, regarding the catalytic activity.[16–19] Due to these aspects the synthesis of multimetallic gels and investigation of their structural peculiarities are in the focus of the work presented in the following. The next part of the work (Chapter 2) aims on the development of different preparation pathways for metallic aerogels and the optimization of synthesis conditions, respectively. The nanostructure and morphology of the resulting materials are characterized by means of electron microscopy. The requirements for synthesis development and further tasks to be addressed by future research form the frame of this chapter.

Chapter 3 gives deeper insight concerning the pore structure and porosity of metallic aerogels by evaluation of N_2 physisorption. Moreover, the influence of thermal treatments on the structure of metallic aerogels is discussed. In the main part of this section the results of several complementary techniques which were applied to investigate the elemental distribution and phase composition of bimetallic aerogels are displayed. It is expected that an increased understanding of the crystal structure and the elemental distribution gives hints on the process of gel formation. Indeed, the appearance and distribution of alloyed and/or segregated metallic phases within the nanostructures of the gel are crucial factors for various material properties and application purposes.

The results presented in Chapter 4 promote the field of metallic aerogels by addressing the challenging issue of processability and device integration. Therefore, hybridization with organic polymers, preparation of transparent thin-films and conductive coatings are in the focus of research. Furthermore, physical properties such as the electrical conductivity and the Seebeck coefficients of different metallic gel structures are determined by various techniques and the applicability of NP-based aerogels for development of thermoelectric materials is discussed.

Chapter 1.

Three-dimensional, porous, metallic nanostructures and nanoparticle-based aerogels[*]

For the preparation of three-dimensional, porous metals a variety of different approaches is established. Several examples are described in the following and compared to each other with respect to their preparation pathway as well as to the inner surface area, the density and the pore size of the resulting porous, metallic structures. It shall be underlined that this discussion is focused on three-dimensional nanostructures. Beyond that, a huge variety of preparation methods and investigations are published in the field of one-dimensional and two-dimensional metallic nanomaterials and networks and it should be taken into account that stacking, arranging and linking of these structures may also lead to three-dimensional materials.

Porous metals which show structuring on the nanometer scale can be produced by two main approaches. On the one hand a pre-developed pattern, array or structure named as template which controls, determines, guides or at least manipulates the shape, morphology and arrangement of the resulting materials can be applied. The template may either stay part of the final structure or will be removed after formation of the desired configuration. By the use of hard or soft templates mainly porous metals with a relatively low surface area are produced. However, established templates and tools for their manufacturing are impressively manifold.[21–28] On the other hand promising alternatives are displayed by template-free methods which also cover a broad range of concepts. Among these approaches famous examples are the directed self-assembly of NPs[29] and the use of the interaction between specific kinds of molecules which act as linkers. For instance the use of long-chain dithiol ligands for the self-assembly of metal NPs in order to build up more complex structures was described.[30,31] Further suitable approaches for the formation of porous metallic nanomaterials are selective dealloying,[32–35] combustion synthesis,[13,36] hydrothermal processes in the presence of dextran,[37] controlling the aggregation of metal NPs in organic media by varying the dielectric constant of the medium,[38] and consolidation of dendrimer-encapsulated NPs.[39] In addition, metallic nanosponges are produced by pH triggered linear aggregation and cross-linking of NPs[40] or even by mixing metal precursors and reducing agent in an appropriate ratio.[41,42] Moreover, a multistep procedure can combine several approaches as for example gold shells with a hierarchical pore structures are obtained by the template-assisted preparation of hollow Au/Ag shells and subsequent dealloying.[43] In many cases serious drawbacks have to be overcome as for instance a limitation of the obtained surface area. Furthermore, many strategies suffer from time consuming multistep procedures or the need of complex suit-

---

[*]Parts of this chapter have already been published.[20]

able linker systems or nanoscaled templates. Besides this, the use of templates is often connected to their subsequent removal which may stay incomplete or require harsh methods. In addition, the restriction of macroscopic dimensions of porous monoliths and films could lead to serious limitations concerning further application and processing. Moreover, several of these approaches lack in adaptability for different classes of materials or preparation conditions. At the same time the sol-gel approach for the formation of porous nanostructures has the potential to overcome the above-mentioned drawbacks. Indeed, this method leads to fine gel-like superstructures without the help of templates, external fields or linker systems. During the process, sol particles are either dispersed in solution or formed by chemical reaction from dissolved precursors. Subsequent condensation reactions lead to the formation of an irregular three-dimensional branched network. Since this process normally occurs in aqueous media and the created pores are filled with water this state of condensation is named hydrogel. In order to obtain a solid material supercritical drying should be applied. This drying technique stands out due to the prevention of a direct phase transition of the solvent from the liquid to the gas phase. Hence, the forces leading to a collapse of the fragile pores inside the structure are minimized and the porosity of the network is mainly retained during the removal of the solvent.[44] The resulting porous monoliths are named aerogels. They are known for their outstanding physical and chemical properties, e.g. extremely low densities, very effective thermal and acoustic insulation and low refractive indices.[44,45]

colloidal solution   gel formation   *hydrogel*   supercritical drying   *aerogel*
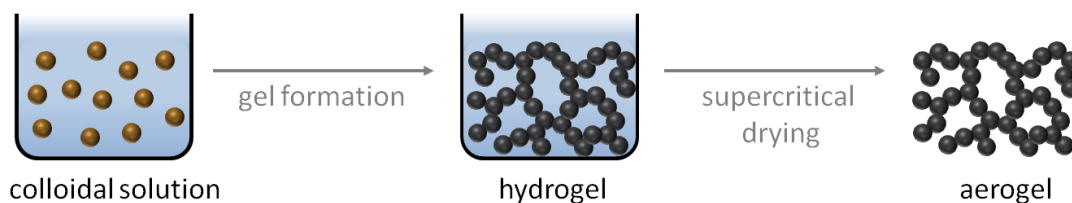
Figure 1.1.: *Formation of gels and aerogels from individual NPs*

The production of aerogels based on the sol-gel approach was first developed in the 1930s for metaloxides such as silica and aluminia.[46,47] Since then preparation techniques have been remarkably improved and even application fields in industry and research have been explored.[45] To further extend the properties and functionality of aerogel materials they were modified with polymers[48,49] and preformed aerogels were used as passive porous matrix for incorporation of metals[50–52] and even NPs.[53–55] Nonnoble metal aerogels have been developed by carbothermal conversion of interpenetrated metal oxide/resorcinol-formaldehyde networks.[56,57] Even superparamagnetic aerogels were processed by the use of crystalline iron oxide.[58] However, the choice of suitable inorganic materials is mainly limited to metal oxides and carbon. In order to overcome this restriction a new approach was required. The story of NP-based aerogels started in 2004 and further attention was attracted by a publication of MOHANAN et al. in *Sci-*

4

ence reporting on the preparation of oxide-free aerogels by the use of semiconductor nanocrystals.[59–61] The general principles of the transition from colloidal NPs through hydrogels to aerogels is summarized in Figure 1.1. On the basis of these pioneering publications many investigations were initiated and several preparation modifications were proposed.[62–74] In addition, the general approach could be transferred to semiconductor NPs synthesized in aqueous media leading to highly luminescent monoliths.[75,76] Furthermore, gels and aerogels are build up from tetrazole stabilized NPs by the help of cation-bridging.[77,78] Quantum dot hydrogels are also used for enzyme encapsulation and their functionality as biosensors was shown.[79,80] Moreover, mixed aerogels from Au and CdTe NPs were fabricated and characterized concerning their optical and structural properties.[81,82] Material aspects and application perspectives of several of the colloidal NP-based aerogels have been summarized and discussed by us in a recent review.[83] As the general approach of NP based aerogels is not only limited to semiconductor nanocrystals it also opens up an innovative possibility for the preparation of highly porous nanostructured metals. The first report on solely metallic NP based aerogels published in 2009 originates from our group.[84] It was followed by the fabrication of monometallic and multimetallic structures built from noble metal NPs[20,85,86] as well as from metal nanoshells.[87] The resulting materials are highly porous, extremely low-weighted, sponge-like, and macroscopic solids which show structuring on the nanometer scale. Indeed, metallic aerogels straddle a previously unoccupied area in the density/pore size parameter space as shown in Figure 1.2. With pore systems in the submicrometer (< 1000 nm) range and relative densities below 0.2 % they offer properties which are not reached by other methods suitable for the preparation of porous, low density metals.
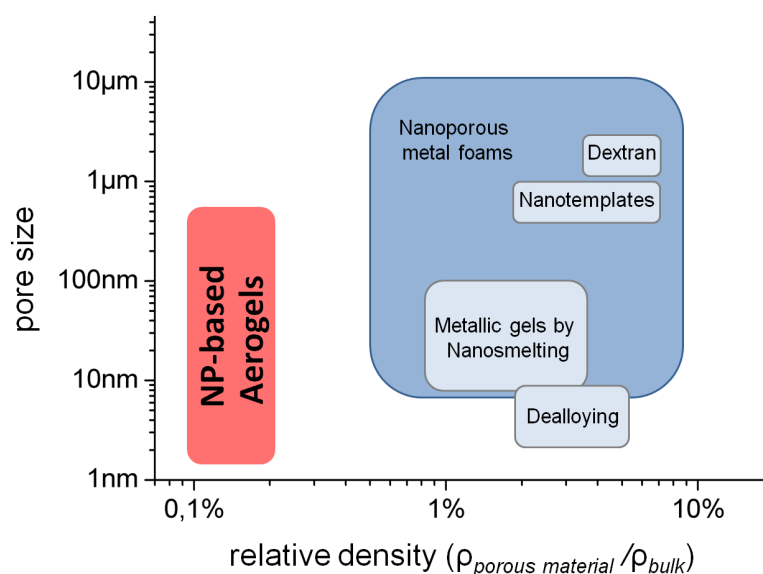
Figure 1.2.: *Density/pore size parameter space. Design of the diagram and data for comparison are adapted from TAPPAN et al.[13] The image was adapted with permission from reference.[20] Copyright 2014 American Chemical Society.*

Table 1.1.: *Surface area values of porous noble metals prepared by several techniques.*

Material	surface area [m^2/g]	surface area [m^2/mol]
dextran-templated Ag sponge [21]	0.5	55
hollow, hierarchical porous Au shells by use of templates and subsequent dealloying [43]	1.6	315
macroporous Ag framework by use of Triton X-114/silica sol as sacrificial template [22]	1.9	205
porous Ag made from 80-nm Ag superspheres [30]	8	860
nanoporous Au foam by electrochemical dealloying of Ag$_{75}$Au$_{25}$ [88]	10...15	1970...2955
Pd nanowires synthesized in hexagonal mesophases [28]	12	1275
mesoporous Au sponge by template-free assembly of glucose stabilized NPs [40]	12	2365
noble metal (Au, Pd) foams by combustion synthesis with metal bistetrazolamine complexes [13]	11...37	2030...3900
interconnected hierarchical porous Pd nanostructures by controlled aggregation in organic media [38]	24	2555
commercially available Pt black [89]	24...29	4680...5655
commercially available Pt black [data sheet from Sigma-Aldrich]	25	4880
3D bimetallic alloy (Pd:Pt = 50:50) nanosponge by reduction in the absence of capping agents [42]	19	2885
Au-Pd bimetallic foams via hydrothermal process [37]	20	3035
noble metal (Au, Ag, Pt, Pd) nanosponges by kinetically controlled reduction process [41]	16...81	1730...8620
polycrystalline Pt nanowires synthesized in a 2-phase system [27]	53	10340
mesoporous Pd$_{0.9}$Rh$_{0.1}$ alloy by partial consolidation of dendrimer- encapsulated NPs [39]	68	7190
commercially available Pd black [data sheet from Sigma-Aldrich]	40...60	4240...6360
bimetallic aerogels formed by self-assembly of metal nanoshells [87]	32...42	4300...6900
Ag-Pt bimetallic NP based aerogel [84]	**46**	**6970**
Au-Ag bimetallic NP based aerogel [84]	**48**	**7020**
Au-Pd bimetallic NP based aerogel [20]	**57**	**8380**
Pt-Pd bimetallic NP based aerogel [20]	**79**	**10900**
β-Cyclodextrin modified Pd aerogel [90]	**92**	**16640**
Pd aerogels with Ca^{2+}-ion growth control [91]	**40...108**	**4250...11490**

In Table 1.1 several approaches for the preparation of porous noble metals and their resulting inner surface areas are summarized. It is pointed out that noble metal NP based aerogels are among the top positions of this ranking and show exceptional high surface areas. Due to their exceptional properties the potential areas of application for metallic aerogels lay in the field of heterogeneous catalysis and electrocatalysis, conductive coating, optical absorbing layers, sensors, SERS, and hydrogen storage. Several studies have already proven their enormous potential and remarkable performance in electrocatalysis. For example, cyclodextrin-modified Pd NP-based aerogels showed extremely high electrocatalytic activity used as anode material in the oxidation of ethanol in alkaline media.[90,92] PdNi aerogels prepared from ligand-free particles synthesized by co-reduction of both metals show promising results in the electrooxidation of methanol in alkaline media.[93] Bimetallic aerogels were also used as a new class of electrocatalysts in the oxygen reduction reaction and the advantages of these support-free, extended, porous metallic nanostructures concerning their electrocatalytic activity and long-term stability under fuel-cell conditions were discussed in detail.[94] Recently, Pd aerogels co-immobilized with glucose oxidase were used for bioelectrocatalytic oxidation of glucose[91] and even the first membraneless glucose/O_2 biofuel cell using Pd-aerogels as electrode material for biocathode and bioanode was established.[95]

Chapter 2.

Synthetic strategies for metallic aerogels

For the preparation of NP-based metallic aerogels two main approaches have been developed and published so far. On the one hand a spontaneous gelation method for the synthesis of Pd hydrogels and aerogels via the reduction of metal precursor salt in the presence of cyclodextrin molecules was established.[90] The cyclodextrin modified Pd hydrogels are formed spontaneously without any further destabilization treatment. Moreover, monometallic and bimetallic gel structures containing Pt and/or Pd have also been fabricated via the one-step gelation approach by reduction of the corresponding metal precursors in the absence of any stabilizing agent.[94] This preparation pathway stands out due to its straightforward and facile synthesis that can be realized without a time-consuming procedure of increasing the particle concentration, which is highly advantageous regarding up-scaling issues. Nevertheless, several washing steps in order to remove reactants residuals and solvent exchange in preparation for the supercritical drying still remain necessary. On the other hand a two-step gel preparation approach was developed.[20,84,91] Here, the gelation process starts from preformed, stable colloidal solutions. In a second step the nanocrystals in solutions are destabilized in a controlled manner and thereby are forming a self-supporting network of interconnected and branched nanochains. The usage of a stable colloidal solution as an intermediate state opens up a great variety of possibilities since the building blocks of the gel can be adjusted individually. Particles of different size, shape, crystal structure and composition as well as even more complex structures like for example core-shell nanocrystals or hollow spheres could be used. Moreover, different kinds of NPs can be combined in one structure by mixing of preformed colloidal solutions and performing of a joint gel formation. This is possible even if the initial syntheses follow different routes or require different conditions. Based in this idea NPs from metals, oxides and semiconductors but even nanocrystals from metals with different reduction potentials can be combined in one network structure. In addition, preceded selection processes for example in order to improve the size distribution of the NPs can be applied. Hence, the approach gains improved flexibility and versatility as well as the possibility to ensure properties of building blocks first before gel formation occurs which may improve monitoring and control of reproducibility. However, challenges of this method arise in the development of conditions for the controlled destabilization of nanocrystal solutions which need to be adjusted for each individual system. It shall be noted that the present work focuses on the two-step gelation process for the preparation of multimetallic nanostructures with only one exception described in Chapter 2.3.

Even though the basic principle of the synthesis of aerogels by the use of noble metal NPs as building blocks has already been established there are many requirements for the prepa-

ration which still remain challenging. Important goals to be addressed by variation and control of synthesis conditions are the following: reach reproducibility of the preparation process and of the properties of the resulting materials; choose appropriate conditions and methods for the controlled destabilization of NPs which is the main step to induce the gel formation; explore possibilities for up-scaling and preparation of large amounts of material since this is a limiting factor for use and development in several application fields; shorten the preparation time and maximize the yield of material; find methods which are applicable to several kinds and mixtures of NPs since this may extend the range and versatility of materials available. In addition the influence of synthesis parameters on structural features of the gel network as for example porosity, pore size distribution and hierarchical pore systems, as well as density of branching, and diameter of the nanochains needs to be understood and thereby become controllable. In the case of multimetallic gels the control of composition and distribution of elements emerges as further requirements. It becomes important, since the ratio of components, and moreover interdiffusion, alloying and segregation behavior will considerably influence the properties and application performance of the respective materials. In order to address some of the requirements listed above several methods for the preparation of noble metal aerogels are developed. Their basic principles and advantages as well as the optimization of synthesis conditions are discussed in the following. The resulting materials are investigated by means of electron microscopy and compared in detail.

2.1. Temperature-controlled gel formation*

2.1.1. Preparation procedure and optimization of synthesis conditions

The general approach for the formation of gels from spherical noble metal NPs has already been topic of several former research investigations and publications.[20,84–86,96,97] The preparation pathway is summarized in the following: NPs from the noble metals Au, Ag, Pt, and Pd are synthesized in aqueous media using citrate as the stabilizing agent and sodium borohydride for the reduction of the respective metals salt. The resulting NPs have diameters of 3 to 6 nm and a bimodal distribution in the case of Ag NPs with additional particles in the size range of 8 to 15 nm as it was shown in former publications of our group.[26,84,98] The particle concentration of the initial solution is quite low and needs to be increased in order to initiate the assembly process. Centrifugation filtration is used in order to stepwise remove the solvent. In contrast to the evaporation of the solvent the centrifugation filtration allows to remove the dissolved ions and thereby avoid a strong rise of the ionic strength of the solution. The stepwise increase of particle concentration is shown in Figure 1 using the example of an Au NP solution. The highly concentrated NP solution is subsequently washed with pure water for several times by the use of the centrifugation filtration technique. In the resulting aqueous solution containing a high concentration of separated, nearly spherical nanocrystals as well as a minimized concentration of stabi-

---

*Parts of this section have already been published.[20]

lizing agent the formation of the network takes places as a continuous and spontaneous process. The coalescence of particles leads to the formation of nanochains which are branching and interpenetrating and thereby are forming an interconnected, large-scale and three-dimensional network. It shall be pointed out that no linkers or templates are used to build up the self-supporting, porous structure. In order to transfer the hydrogel into a solid aerogel monolith the cold supercritical drying approach using CO_2 as a solvent is applied.[44,99] In order to ensure miscibility with liquid CO_2 the aqueous solution inside the pores is first replaced against acetone by a multistep exchange. Images of some typical hydrogel samples and aerogel monoliths can be found in Figure 2.1.
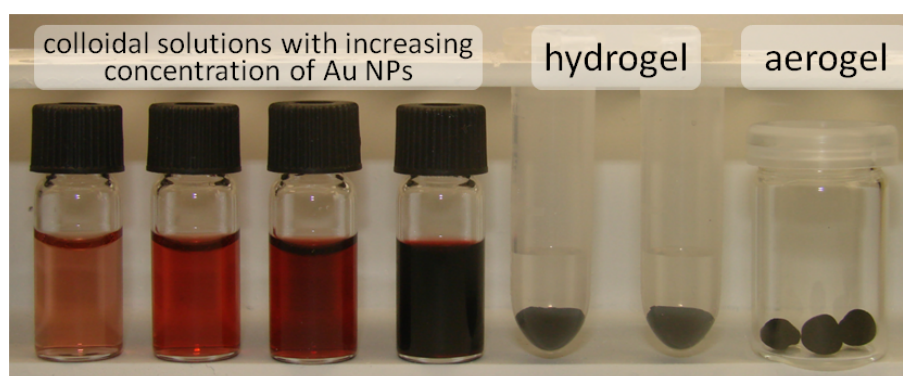
Figure 2.1.: *Stepwise increase of the particle concentration by centrifugation filtration in the case of a colloidal solution of Au NPs (left). Hydrogels with colorless supernatant and aerogel monoliths obtained after supercritical drying are shown on the right.*

The realization of a fast and reproducible preparation pathway is one of the main requirements for application purposes. Elevated temperature can be used in order to increase diffusion rates of colloidal particles and of stabilizing molecules in solution as well as the diffusion rate of atoms inside the metal crystal structure making coalescence and gelation even more efficient. Increasing the temperature during the gel formation leads to controllable acceleration of the gelation process and simultaneous strong improvement of reproducibility. The shortening of the gelation time depending on the applied temperature is displayed in Figure 2.2. In the case of a bimetallic mixture of Au and Ag NPs the complete formation and settle down of hydrogel is observed within 2-3 weeks at room temperature. By increasing the temperature to 75 °C this process is shortened to 12 hours. This effect appears for all tested solutions and a minimum gelation time of 2 hours is reached in the case of Ag-Pt hydrogels. Meanwhile, the resulting structures show no significant differences compared to those obtained at room temperature. Additional destabilization agents like H_2O_2 or ethanol were not used throughout the following studies, since they may cause undesired inclusion of organic compounds or impurities. Moreover, their effect on acceleration of gel formation and improvement of reproducibility is small compared to the improvements realized by elevated temperature. Furthermore, it shall be pointed out that, after formation of hydrogel the supernatant is a clear and colorless solution as can be seen in Figure 1. Therefore, a complete or almost complete transfer of NPs from the

highly concentrated solution into the network structure of the gel is assumed. This kind of nearly 100 % yield is highly important when dealing with expensive or rare materials like noble metals. Nevertheless, there may be certain losses of material during the solvent exchange and drying steps due to the fragile structure of the material. These losses are to be minimized by careful handling.
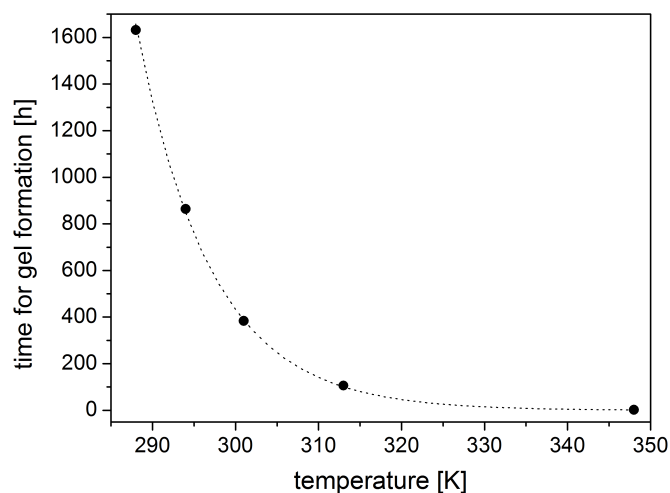
Figure 2.2.: *The gelation time is strongly shortend with increase of the applied temperature. Hence, elevated temperature is a powerful tool to reach a controllable acceleration of gel formation and thereby a strong improvement of reproducibility of the preparation pathway.*

2.1.2. Multimetallic structures and control of composition

As already mentioned this work focuses on the preparation and investigation of multimetallic nanostructures since synergetic effects are expected by the interaction of several kinds of metals. Based on the approach described above the synthesis of multimetallic structures is realized by mixing the highly concentrated solutions of different monometallic NPs and performing a joint gel formation. For the noble metals gold, silver, platinum, and palladium all conceivable combinations of either two, three or all four of these metals are realized in porous network structures. The list includes the following multimetallic hydrogels and aerogels: Au-Ag, Ag-Pt, Au-Pd, Ag-Pd, Pt-Pd, Au-Ag-Pt, Au-Pt-Pd, Ag-Pt-Pd, and Au-Ag-Pt-Pd. It is interesting to note that the only exception is the combination of gold and platinum NPs. The formation of Au-Pt aerogels is still under investigation since these materials are known for their catalytic activity regarding several reactions.[100–102] It is obvious that the control of the elemental composition of the resulting nanostructures is one of the important requirements concerning the synthetic approach. The metal ratio of the final gels is equal to the metal ratio of the initial NP solution mixture. Hence, different material composition in the gel can be reached by varying the volume ratio of the different monometallic NP solutions. In order to calculate the volume ratios needed, the elemental ratio of the initial NP solutions is first determined by energy-dispersive

X-ray spectroscopy (EDX) analysis. Furthermore, thermogravimetric analysis (TGA) in the temperature range up to 1000 °C show a mass loss of 7.1 wt % in the case of an Au-Pd aerogel and 6.4 wt % in the case of an Pt-Pd aerogel, respectively. The main part of the mass loss appears in the temperature range below 400 °C. Only the nonmetallic, organic compounds as well as water and molecules adsorbed to the surface are evaporated during this process. Hence, it should be pointed out that the aerogels prepared by the NP-based approach mainly consist of pure metal which is an important difference compared to nanoporous metals containing templates or linkers. The measurements are performed under argon atmosphere in order to avoid mass increase due to oxidation of the metals. Nevertheless, even after several steps of evacuating and flushing with argon the pores of the aerogel still may contain small amounts of air and therefore a complete removal of oxygen is challenging.

2.1.3. Electron microscopy investigations

Transmission electron microscopy (TEM), electron diffraction and scanning electron microscopy (SEM) were used to characterize the structure of the as prepared aerogels. In Figure 2.3 the results from TEM for some representative bimetallic structures are shown. It is obvious from all images that the coalescence of the initial spherical NPs leads to the formation of chainlike structures. This fundamental behavior is observed throughout all investigations but still there are slight differences concerning the appearance of the nanostructures. In the case of Au-Pd (Figure 2.3 (d)) the nanochains have a pearl necklace like structure and the nanochains formed from Pt and Pd NPs (Figure 2.3 (b)) seem less smooth and more irregular, whereas in the case of Au-Ag (Figure 2.3 (a)) the nanocrystals seem to be fused together more strongly and the initial spherical shape of NPs can hardly be recognized within the nanochains. These morphologies give a first hint about the differences of structures and the merging of particles for different metal combinations which will be investigated and discussed in detail in Chapter 3.

The diameters of the nanochains were evaluated from TEM images taking into account more than 250 measurements, respectively. The results for some bimetallic aerogels are summarized in Figure 2.4. Since the nanochains have a similar diameter like the initial NPs, it can be concluded that no preagglomeration or formation of secondary particles occurs. Both TEM image (Figure 2.3 (c)) and diameter distribution (Figure 2.4) of Ag-Pd aerogel display also segments of the nanochains with a larger diameter. This may be caused by the bimodal size distribution of the initial silver NPs which tend to form particles with a diameter of about 5 nm but also some bigger nanocrystals in the size of 8 to 15 nm. Hence, also in the case of Ag-Pd no preagglomeration of particles is assumed during the gel formation process. In general, the particles used in a typical experiment have diameters less than 10 nm. It shall be noted that the use of larger nanocrystals also leads to the formation of networks. However, it should be taken into account that for larger NPs sedimentation is the dominant process interfering with the three-dimensional network formation.
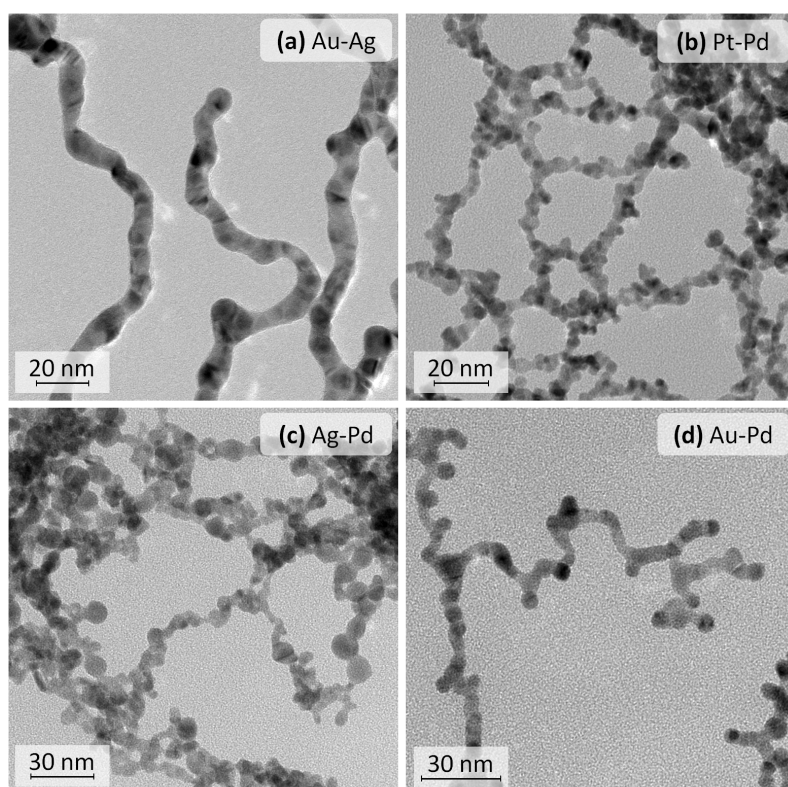
Figure 2.3.: *TEM images of several bimetallic aerogels. The coalescence of the initial NPs leads to the formation of nanochains which are assembled into the network structure.*
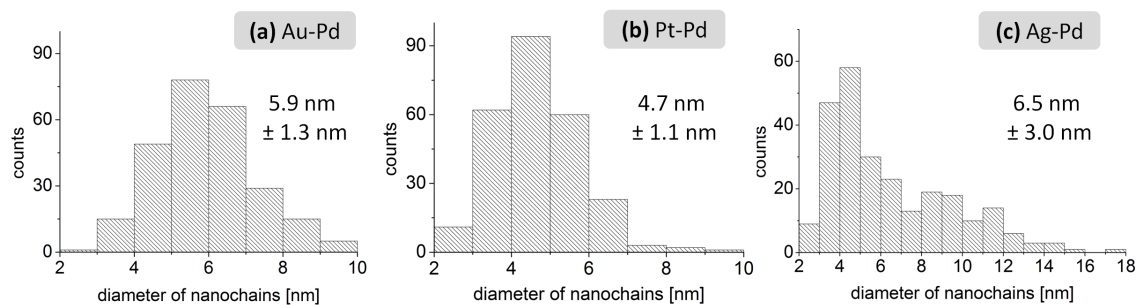
Figure 2.4.: *Distribution of the diameter of nanochains for several examples of bimetallic aerogels. Since the nanochains have a similar diameter like the initial NPs no agglomeration of formation of secondary particles before the gel formation is assumed.*

In the typical TEM overview images with lower magnification shown in Figure 2.5 the wide-spreading network formed by interconnection and interpenetration of nanochains is evidenced. Branching points with fission into 2 or 3 branches are frequently part of all structures observed. The electron diffraction patterns displayed in the insets of Figure 2.5 show diffraction rings instead of separated spots which prove the polycrystalline nature of the nanochain networks shown in the corresponding TEM images of Figure 2.5. The

distances of diffraction spots from the center of the circle or in this case the radii of the diffraction rings are related to the reciprocal values of the lattice plane distances.
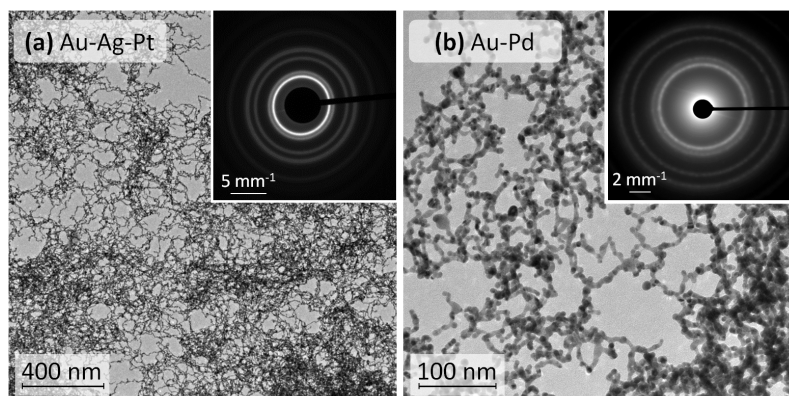
Figure 2.5.: *Overview TEM images reveal the wide-spreading network of the gel structure. Insets show electron diffraction patterns of the area displayed in the image, respectively. The polycrystallinity of the structure is evidenced by the appearance of rings instead of spots in the diffraction pattern. The image was adapted with permission from reference.[20] Copyright 2014 American Chemical Society.*
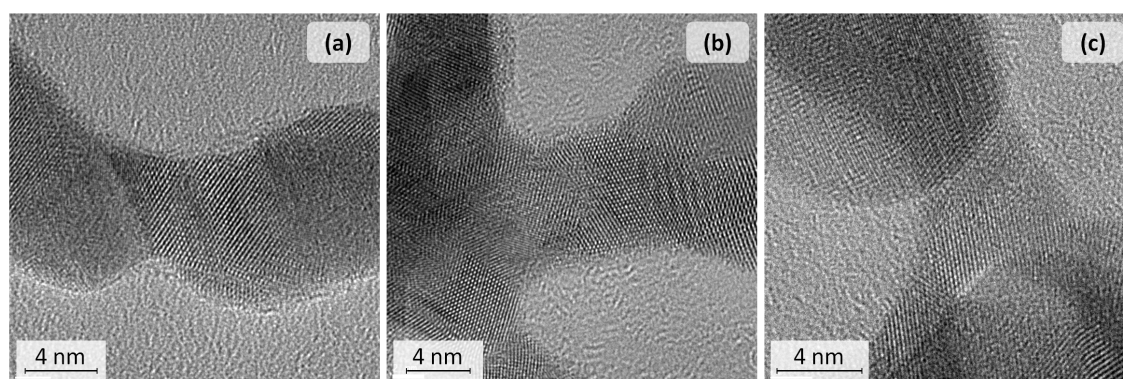
Figure 2.6.: *HRTEM images of an Au-Ag aerogel specimen prove the coalescence of particles without linkers or organic layers between the particles. Furthermore, the variety of grain boundaries which may act as catalytic reactive sites is obvious. Part (a) was adapted with permission from reference.[20] Copyright 2014 American Chemical Society.*

With high resolution TEM (HRTEM) shown in Figure 2.6 the coalescence of the particles within the nanochains without the help of linkers or other supporting materials of the Au-Ag system is confirmed since there is no spacing or organic layer between the aggregated particles. Furthermore, these investigations accentuate the variety of existing grain boundaries in a nanochain arrangement from Au and Ag NPs. Some of these are already formed during the NP synthesis as it is known for the reduction of metal salts

by NaBH$_4$.[103] Additional grain boundaries may occur during the fusion of NPs forming the chain where different crystal facets are interacting. These grain boundaries are of great interest for example with respect to the application in catalysis as the advantage in catalytic activity of nanochains with high density of grain boundaries compared to single nanocrystals with comparable diameter was already shown in the literature.[104] A reliable location of crystal planes for gold and silver is not possible due to overlapping of several crystal facets in the three-dimensional structure, possible torsions at the grain boundaries and the variety of crystal orientations.

The large-scale, three-dimensional and porous structures of the metallic aerogels are further investigated by means of SEM (Figure 2.7). For better comparison images of the same magnification of Au-Pd, Pt-Pd and Ag-Pd aerogels are shown in Figure 2.7 (b, c and d) and no significant morphological differences are observed. Independent from the individual material, a homogeneous, sponge-like network is formed within the whole macroscopic monolith which is also evidenced by the lower magnification image in Figure 2.7 (a).
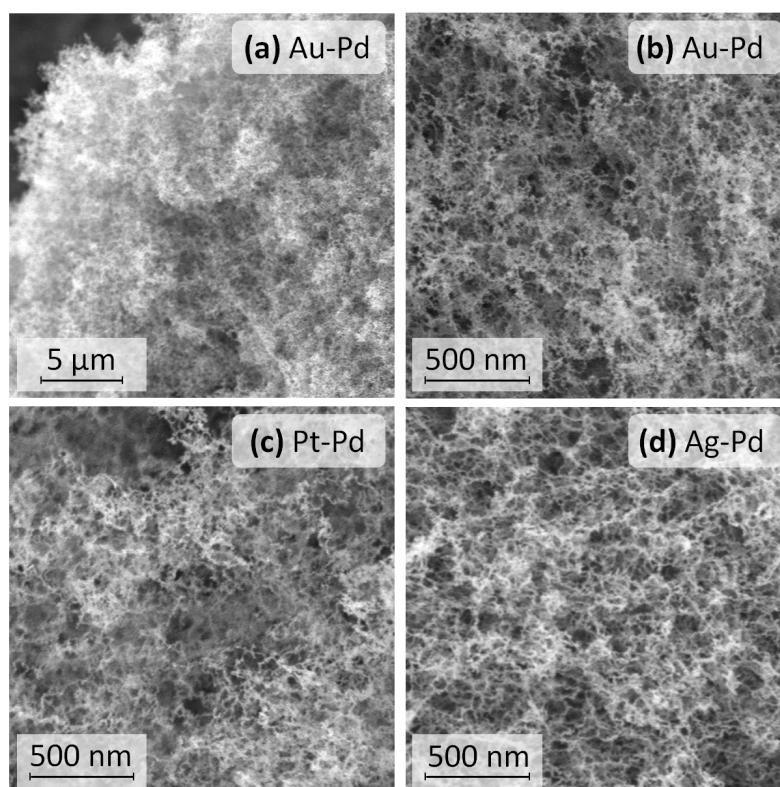
Figure 2.7.: *SEM images of several bimetallic aerogels display the three-dimensional, homogeneous and highly porous structure of the gel network. The image was reprinted with permission from reference.[20] Copyright 2014 American Chemical Society.*

2.1.4. The evolution of the network structure

The evolution of particle coalescence and the formation of nanowires and their intercon-
nected structure were studied by means of absorption spectroscopy and TEM. Concen-
trated, aqueous solutions of Au and Ag NPs were combined in order to reach a 1:1 atomic
ratio of both metals and the mixed solution was kept at 75 °C until complete hydrogel
formation was observed. In order to monitor the reaction samples were taken after each
15 minutes. The preparation of the TEM samples as well as the measurement of the ab-
sorption spectra was carried out directly after the sample-taking in order to avoid further
progress of the reaction. Nevertheless, when evaluating the results from TEM one should
take into account that the agglomeration and further coalescence of NPs and nanochains
may occur during the drying process of the sample on the hydrophilized carbon-coated
copper grid.
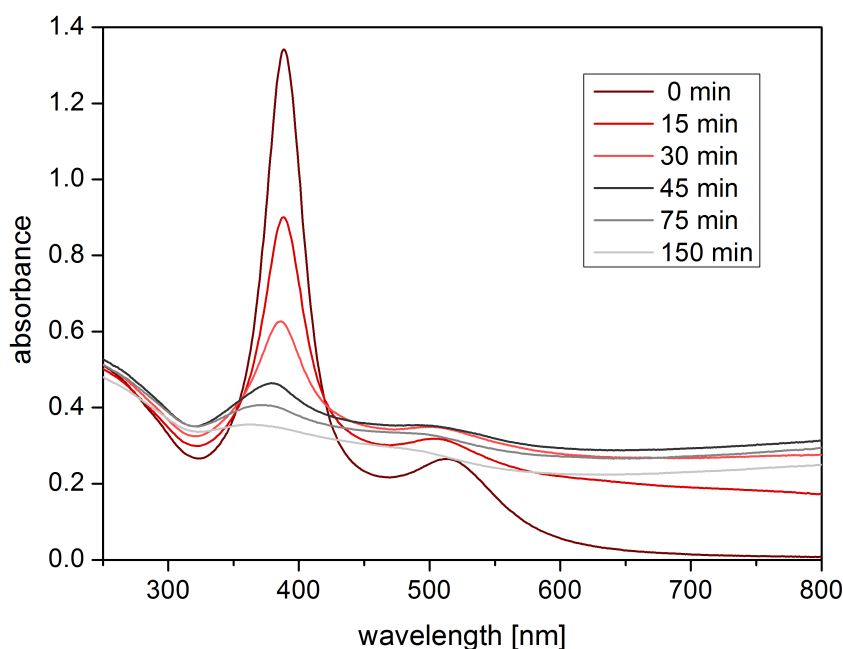
Figure 2.8.: *Evolution of the absorption spectrum of a highly concentrated solution containing
Au and Ag NPs kept at 75 °C. Two separated absorption maxima are observed in
the initial solution due to the SPR of spherical Ag and Au NPs. While the reaction
proceeds the formation of aggregates is indicated by the strong and broad absorption
at longer wavelengths.*

The absorption spectrum of the freshly mixed NP solution shows two separated max-
ima which correspond to the surface plasmon resonance (SPR) of Ag (389 nm) and Au
(513 nm) NPs (Figure 2.8). Even at this stage an agglomeration of particles is observed in
TEM as shown in Figure 2.9 (a). Both, single, individual particles and agglomerated ones
are observed, whereas the latter have probably been formed during the drying process
on the carbon film, since there are no indications for aggregation in the corresponding

absorption spectrum. It shall be noted that no elongated nanochain-like fragments are observed at this stage which underlines that nanowire formation did not start yet. Already after 15 minutes at 75 °C the color of the solution turned to black affirmed by a strong increase of absorption at longer wavelengths. This enhanced flat absorption may arise from the longitudinal mode of the SPR of nanowires with many different lengths and therefore gives a hint to the aggregation of particles into elongated structures. The broad size distribution of the nanowires is reflected in the broad absorbance band. Due to the SPR of the remaining single NPs and the transverse mode of the SPR of the nanowires the absorption maxima observed before are still present. Whereas the absorption maximum at the SPR of Ag NPs drops down, the absorbance at 515 nm where the SPR of the spherical Au NPs is located increases. This is probably caused by an overlapping with the broad and flat absorption at longer wavelengths. With increasing reaction time the described trend further proceeds until all NPs are implemented within the network structure. The broad absorption in the whole visible range which is generated in the reaction solution during the gel formation is also associated with the absorption behavior of the hydrogels and the solid aerogel monoliths since the gels obtained had no characteristic color, but instead were all black.

A similar appearance of the absorption spectrum and a grayish color of solution caused by welding and linear aggregation of spherical Au NPs into a network of nanochains was also shown and discussed in the literature.[40,105,106] Moreover, PONG et al. described an intermediate state of nanowires formed during the evolution of spherical Au NPs by reduction of metal salt with citrate which is characterized by a dark blue color and a flat absorption profile. Here, darkening of the solution was linked to an increase of the nanowire lengths and the formation of an extensive network.[107]

The results from TEM analysis confirm the assumption that the NPs first form some short chains. In Figure 2.9 (b) separated nanochains with length of about 50 nm as well as agglomerates of particles are observed. After 30 minutes (Figure 2.9 (c)) strong coalescence of the initial particles within the elongated fragments is obvious and the nanochains are already branched and partially interconnected. However, the nanowires exhibit a "knobbly" and pearl necklace-like morphology. After 60 minutes of reaction time the nanochains are smoothed and they exhibit a similar morphology compared to the final structure. Until the formation of hydrogel is completed a further interconnection and branching of nanochains is observed. In the final structure (Figure 2.9 (f)) no single particles or separated short chain segments are observed and the coalescence of NPs and smoothing of nanowire surfaces is even more pronounced.
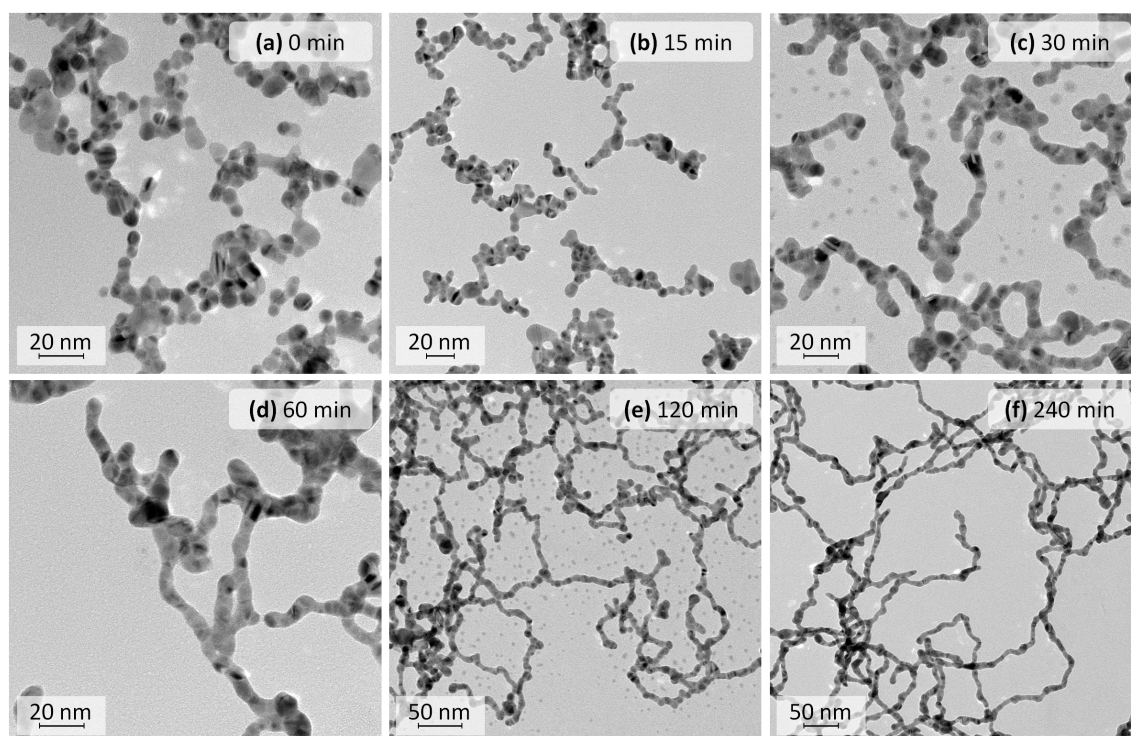
Figure 2.9.: *TEM images monitoring the structural changes during the formation of an Au-Ag hydrogel. Starting from spherical particles which tend to agglomerate on the carbon film short nanochains and finally a network structure is growing. The ongoing coalescence of NPs leads to a smoothing of the nanochain morphology.*

2.2. Ion-induced gel formation

2.2.1. Synthetic procedure, benefits and variety of materials

In order to face the different requirements regarding the properties of metallic aerogel materials and the synthesis conditions an extension of the portfolio of preparation pathways is desirable. The alternative synthetic procedure described in the following meets several requirements: It provides a fast gel formation process which can be realized within minutes or seconds instead of hours or days whereas no elevated temperature is needed. These are favorable conditions for scale up of the process. Furthermore, it is a universal approach which enables the preparation of monometallic as well as multimetallic structures from noble metal NPs.

The initial conditions are quite the same as described for the temperature-controlled gel formation (Chapter 2.1) which comprises that noble metal NPs are prepared in aqueous media and their concentration is increased by a stepwise removal of the solvent via filter centrifugation. It is expected that the merging of NPs during the gel formation is facilitated by a low concentration of stabilizing molecules on the particle surface leading to partially bare metal surface and lowering of electrostatic shielding and stabilization. In order to minimize the concentration of stabilizing agent molecules several washing steps

were applied to the highly concentrated NP solutions. The noble metal NPs used in the experiments are stabilized by citrate ions which are known to form stable complexes with many transition metal ions. Due to the chelate effect the stability constants of these complexes are pretty high and complex formation is favored.

It is believed that after the addition of small amounts of transition metals ions to the highly concentrated NP solution, citrate is acting as chelating agent and the concentration of free citrate ions in solution as well as on the NP surfaces is reduced. Hence, the decrease of stabilization might lead to coalescence of the NPs which initiates the formation of nanowires and a network structure. Even though the reaction mechanism is still under investigation as it will be discussed later, it was evidenced for many different examples that the addition of small amounts of transition metals ions like Ni^{2+}, Cu^{2+}, Fe^{3+} or Ag^+ to concentrated solutions of citrate-stabilized noble metal NPs lead to a spontaneous gel formation. For Au, Pt and Pd NP solutions as well as for their bimetallic mixtures (Au-Pt, Au-Pd, Pt-Pd) the gel formation was performed by the addition of the four different kinds of metal ions. In a typical experiment 0.01 M aqueous solution of a nitrate metal salt is added stepwise to the concentrated and washed NP solution until millimeter-sized precipitates dispersed in a colorless supernatant are observed. The final concentration of metal ions in the colloidal solution which is needed to induce the gel formation is below 1.5 mM. At the beginning of the gel formation small segments are dispersed in the solution but settle down rapidly forming a hydrogel sample which is less compact compared to hydrogels obtained by the temperature-controlled approach. Nevertheless, after supercritical drying solid aerogel monoliths are obtained.

Even though gel formation is performed successfully in all cases, the resulting network structures look quite different as revealed by the TEM images shown in Figure 2.10. For example, the nanoparticular building blocks of the Pd (Ni^{2+}) aerogel do not form elongated nanowires but agglomerated structures of irregular size. The structures of Pd (Cu^{2+}), Pt (Ag^+) and Pt-Pd (Ag^+) exhibit a mixture of elongated nanowires with diameters similar to the initial NPs but also thicker and aggregated segments. In the case of Au-Pt (Ni^{2+}) an even more irregular structure is obtained which contains large irregular shaped fragments decorated and mixed with small and agglomerated NPs. Since a quite similar behavior is also observed in Au-Pd (Ni^{2+}) aerogels, it is expected that Au is aggregating to form large and irregular shaped particles whereas Pt particles do not grow but perform irregular agglomeration. Nevertheless, it shall be noted that gel formation was performed successfully in the case of an Au-Pt structure which could not be realized by the temperature-controlled approach. Moreover, different elemental compositions of the nanostructures can be implemented by controlling the ratio of different monometallic NPs in the initial solutions. One example for bimetallic aerogels with different metal ratios is shown in Figure 2.11. Even though both TEM images (Figure 2.11 (a, b)) reveal a large amount of agglomerated particles the structure of Pt_{20}-Pd_{80} shows stronger coalescence of particles and more elongated structural elements compared to the Pt_{50}-Pd_{50} aerogel sample. It is obvious that the structure of the Au (Ag^+) aerogel (see Figure 2.10 (d))constitutes an exception since this material provides a network of continuous nanowires with diameters of about 5-8 nm. Also the hydrogels and aerogels of this material are characterized by their high stability and monolithic shape. It should be pointed out that this is an outstand-
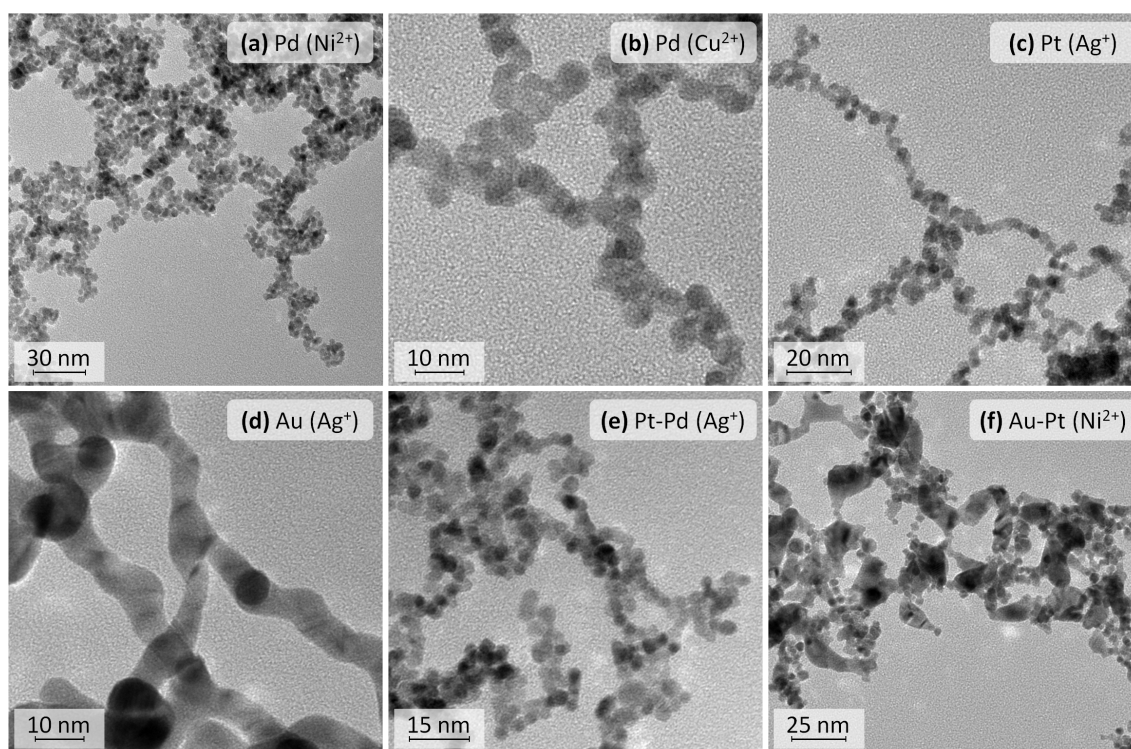
Figure 2.10.: *TEM images of different samples obtained by ion-induced gel formation reveal their different structural features.*

ing method for preparation of monometallic Au aerogels taking into account that other approaches e.g. the use of destabilization agents such as H_2O_2 or ethanol, suffer from pre-agglomeration of Au NPs leading to strikingly thicker nanowires ($> 100\,nm$) and less porous structures.[84] It is supposed that the acceleration of reaction and formation of nanochains by the ion-induced approach helps to prevent pre-agglomeration of NPs.

Although a structural variety was observed in TEM the corresponding SEM images of Au (Ag^+), Pd (Ni^{2+}) and Pt-Pd (Ni^{2+}) displayed in Figure 2.12 confirm the highly porous network structure of the obtained aerogels. Similar to the results from the temperature-controlled approach the nanochains are forming a self-supporting network and a system of open pores and tunnels is provided.

It was noticed that dispersing of e.g. Pt-Pd (Ni^{2+}) or Pt (Ni^{2+}) aerogels in water by ultra-sonification leads to decomposition of the nanowires into short chains or particle agglomerates which is signalized by a brownish color of the dispersion. No decomposition to the initial particle size is assumed because of the fast sedimentation of the resulting fragments. It is expected that this behavior originates from the less pronounced merging of nanocrystals in the network. To overcome this issue, material properties can be markedly improved by annealing the sample under mild conditions and thereby promote the welding and interconnection of the nanosized building blocks. For example the Pt_{50}-Pd_{50} (Ni^{2+}) aerogel shown in Figure 2.11 (a) was annealed at $150\,°C$ for $150\,minutes$ which leads to strong structural changes as presented in Figure 2.11 (c). An inert atmosphere was used
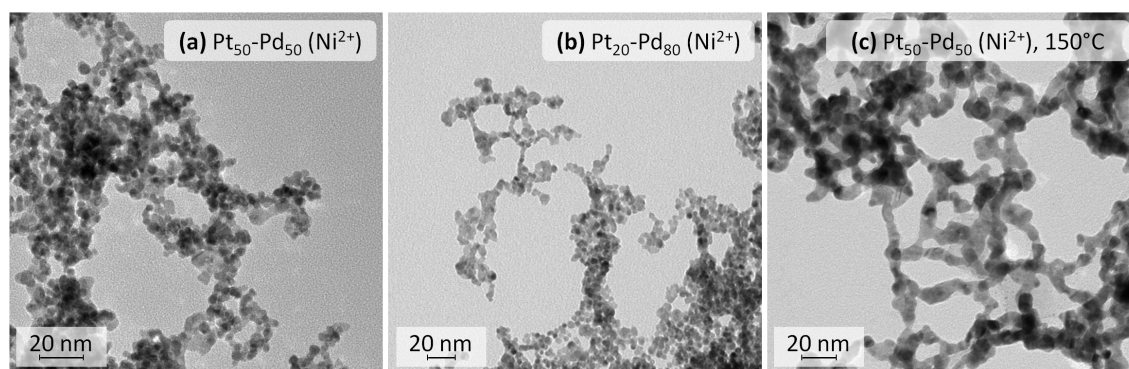
Figure 2.11.: *TEM images of Pt-Pd (Ni^{2+}) aerogel structures with different elemental composition (a,b). After annealing at 150 °C for 150 minutes under inert atmosphere elongated nanowires instead of irregular agglomerates are obtained (c). After the thermal treatment the stability of the aerogel is strongly improved and the material can be dispersed without decomposition.*
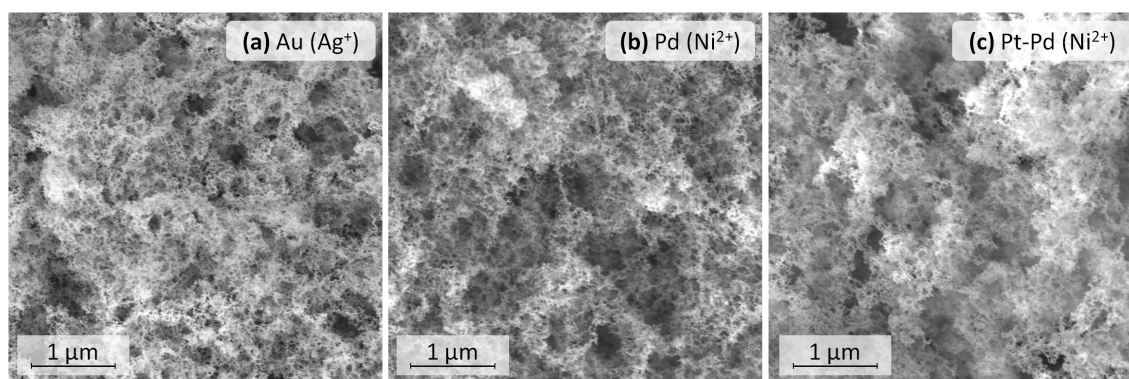
Figure 2.12.: *Corresponding SEM images for some of the samples investigated in TEM. They illustrate the high porosity and open pores formed by the fine network of nanochains within the gels.*

in order to prevent oxidation of the metal during the thermal treatment. After annealing of the aerogel a network of elongated nanowires is obtained which are not decomposed by ultrasonification and cause a grayish color of the corresponding aqueous dispersion.

In fact, the transition metal ion (Ag^+, Ni^{2+}, Cu^{2+}, Fe^{3+})-induced preparation of noble metal NP-based gels and aerogels was not presented before but a similar approach was used by WEN et al. who prepared Pd aerogels for application in bioelectrocatalysis by the addition of different amounts of Ca^{2+} ions to citrate-stabilized Pd NPs.[91] It was found that the amount of Ca^{2+} ions added to a Pd NP solution influence on the one hand the time scale of gel formation but on the other hand also determines the final porosity and structure of the gel which is formed. The higher the concentration of Ca^{2+} ions the faster the coalescence of particles and the gel formation occur. However, the structures of the resulting aerogels differ from those obtained by slow gel formation at low Ca^{2+} concentration. The latter are similar to the nanowire structures obtained by the temperature-induced gel

formation described in Chapter 2.1 On the other hand at higher Ca^{2+} concentration the materials exhibit higher densities and smaller pore sizes. Their structures show less elongated nanowires and the particles form a higher number of irregular agglomerates which corresponds e.g. to the results of Pd (Ni^{2+}) aerogels shown in Figure 12.10.

Nevertheless, one of the main goals of the synthetic approach presented here is the acceleration of the gel formation and therefore improving its availability and ease of use especially with respect to up-scaling and preparation of devices for application issues. Therefore the amount of ions was increased to a value where gel formation is realized within seconds or at maximum 1-2 minutes. Afterwards, only few minutes are needed in order to further settle down the porous structure of the hydrogel in the solution. Although less compact monoliths or smaller fragments might be formed by the approach, this may not be a great disadvantage for further use of the materials e.g. for preparation of coatings, inks, dispersions or powders.

Moreover, promising results concerning simplification and up-scaling of the preparation of NP-based aerogels are achieved by the ion-induced approach. Instead of filter centrifugation a rotary evaporator was used to remove the solvent from noble metal NP solution and thereby increase the particle concentration 10 times. As it was proven by the experimental results, this concentration factor was sufficient which signifies that no maximization of NP concentration is essential in this approach. Much larger volumes of NP solution can be treated in this way in short time which is associated with tremendous time saving. Nevertheless, washing the solution with pure water by help of centrifugation filters is still an essential working step. Afterwards gel formation is induced by a final Ni^{2+} concentration of 2 mM. Furthermore, the approach introduces the possibility to use NPs with a considerable larger diameter. It should be taken into account that for bigger particles sedimentation is a strong and conceivably dominant process interfering with the three-dimensional network formation. Owing to the fast and spontaneous initiation of the gel formation process and the lower NP concentration required, the ion-induced preparation pathway is highly suitable for large particles. First experiments with Pd nanocrystals with a diameter of ca. 10-20 nm were performed. The NPs were prepared by the seeded-growth method[†] and further concentrated and washed with the filter centrifugation technique. This preliminary experiment shows very promising results since gel formation was observed immediately after addition of Ni^{2+} ions.

2.2.2. Investigation of the gel formation process

The evaluation of the processes which take place in the reaction solution after the addition of the metal ions and finally lead to the gel formation remains a challenging task. It cannot be simply assumed that citrate is partially removed from the particle surface via the interaction with the metal ions leading to controlled destabilization of particles and formation of a network structure. Another mechanism could be that the metal ions act

---

[†]Pd NPs prepared by seeded-growth method were provided by M. Werheid (Physical Chemistry, TU Dresden).

as interparticle bridges which connect the neighboring NPs by interaction and complex formation with the citrate molecules on the particle surface. Indeed, a similar kind of bridging the NPs by complexation has already been used to form gels from several kind of nanocrystals. In this approach the ability of tetrazole derivatives to build strong complexing bridges with several metal ions was used for the interconnection of semiconductor but also metal NPs, leading to multibranched network structures.[77,78,81] In order to assess the interaction between metal ions, citrate molecules and noble metal NPs several investigations should be considered:

(1) Because of their high solubility in aqueous media nitrate salts of the different metals were used throughout all experiments. However, the addition of KNO_3 solution to the NP solutions did not lead to gel formation at all even if a notably higher final concentration of the salt was used. Hence, the alkaline metal ion K^+ is not suitable for destabilization of the nanocrystals and moreover, no influence of the nitrate used as a counter ion is concluded. This investigation clarifies also that the destabilization of particles and the gel formation are not only induced by the increase of the ionic strength of the solution.

(2) The concentration of citrate in the NP solution is a crucial factor for the concentration of metal ions needed to induce the gel formation. It was shown that addition of a defined amount of citrate molecules to the concentrated and washed NP solution before addition of metal ions leads to an increase of the amount of transition metal ions needed to initiate the gel formation by the very same molar value. For example 0.1 μmol of Ni^{2+} were required to start gel formation in 0.25 ml of a Pt NP solution. After addition of 1, 2 or 3 μmol of sodium citrate to 0.25 ml of the same initial Pt NP solution 1.1, 2.1 and 3.0 μmol of Ni^{2+} ions were needed to induce the gel formation, respectively. This correlation confirms the strong interaction of citrate molecules with the transition metal ions as well as the importance of washing the NP solutions with pure water in order to minimize the concentration of "free" citrate ions in solution.

(3) The concentration of metal ions needed for a spontaneous gel formation is not a fixed value. For different transition metal ions different amounts were needed to induce the gel formation in the same NP solution and the required concentration of ions follows the general trend $Ag^+ > Ni^{2+} > Cu^{2+} > Fe^{3+}$. To give an example a final concentration of 1.0 mM or 0.2 mM of Ni^{2+} or Fe^{3+} ions is needed to initiate the gel formation in concentrated and washed Pd NP solutions, respectively. Moreover, the concentration of noble metal NPs in solution determines the consumption of metal ions. It is reasonable that higher amounts of metal ions are needed to initiate the gelation in the case of Pd NP solutions since a higher amount of Pd precursor is utilized in the initial particle synthesis and hence a higher particle concentration is expected. Assuming no losses of material during the preparation pathway the noble metal concentration in the final solution is about 15 mM (Au, Pt) and 28 mM (Pd), respectively. Considering Pt NPs with a diameter of 5 nm as an example this would correspond to a final particle concentration of 3.2 μM. However, the determination of the final citrate concentration and in particular the number of citrate molecules per metal nanocrystal is quite challenging and no exact number can be

given here. Nevertheless, it is assumed that interaction between the particle stabilizing molecules and the transition metal ions takes place. In this context it seems reasonable that even a slight decrease of stabilizer concentration on the particle surface or a decrease of electrostatic repulsion may lead to coalescence of particles especially in aqueous solution with extremely high particle concentration and low amount of stabilizing agent.

Many conditions and parameters are crucial for the complex formation and the stability of the noble metal NPs. Among those are pH and ionic strength of the solution; stability constants, composition and charge of the formed complexes; formation of insoluble salts (e.g. AgCl); crystal structure of the particles and interaction of citrate molecules with the particle surface. Since many of these factors are either difficult to be determined in a multicomponent system or are strongly affecting each other, predictions for the required amount of transition metal ions not investigated yet are highly challenging. Nevertheless, the results obtained for gel formation using Ag^+, Ni^{2+}, Cu^{2+} and Fe^{3+} are highly reproducible with only slight deviations for different samples series probably resulting from small differences in concentration of particles or citrate ions arising due to the multistep procedure of particle synthesis, solvent removal and washing. For example loss of NPs by adsorption to the centrifugation filter membranes cannot be fully avoided or precisely controlled. Nevertheless, for the very same concentrated and washed NP solution the experiments and the results for the obtained structures are highly reproducible.

(4) For semiconductor nanocrystals bridged by tetrazol metal ion complexes the reversibility of the process was shown by the addition of the strong complexation agent ethylenediaminetetraacetic acid (EDTA) which forms stable complexes with the metal ions and leads to dissolving of the gel.[77] In order to compare with these results and investigate the influence of a strong, competitive complexation agent 0.1 M EDTA solution was added to the supernatant of a Pt (Ni^{2+}) hydrogel. After shaking, a brownish and clear solution was obtained that was stable over several minutes without formation of agglomerates visible to the naked eye. It shall be noted that a brownish and clear solution was also observed after shaking the sample before addition of EDTA, but complete reagglomeration of particles occurred within 2 minutes. TEM images of the EDTA treated hydrogel as well as of a corresponding pristine aerogel are shown in Figure 2.13. An aggregated and connected network structure similar to other Pt containing gels obtained by the ion-induced approach is observed for the Pt (Ni^{2+}) aerogel sample (Figure 2.13 (a)). In contrast to that a loose structure and a large number of unattached spherical particles as well as dimers and trimers are observed at same magnification of the EDTA treated hydrogel sample (Figure 2.13 (b)). This impression is confirmed by the high amount of loose, single particles and small agglomerates obvious in the low magnification image of Figure 2.13 (c). While comparing the results from aerogel and EDTA treated hydrogel one should take into account that supercritical drying itself may enhance the welding of NPs and the stability of the material which is reflected by the stronger coalescence of building blocks observed in TEM. Moreover, even the untreated hydrogel shows limited stability when dispersed in solution as described in the former section so the influence of EDTA on the structure decomposition due to dispersing is uncertain. In summary, no completely reversible dissolution of the gel network by addition of EDTA was observed. But still, EDTA seems to

enhance the degradation of the network structure and cause a partial dissolution of the gel.
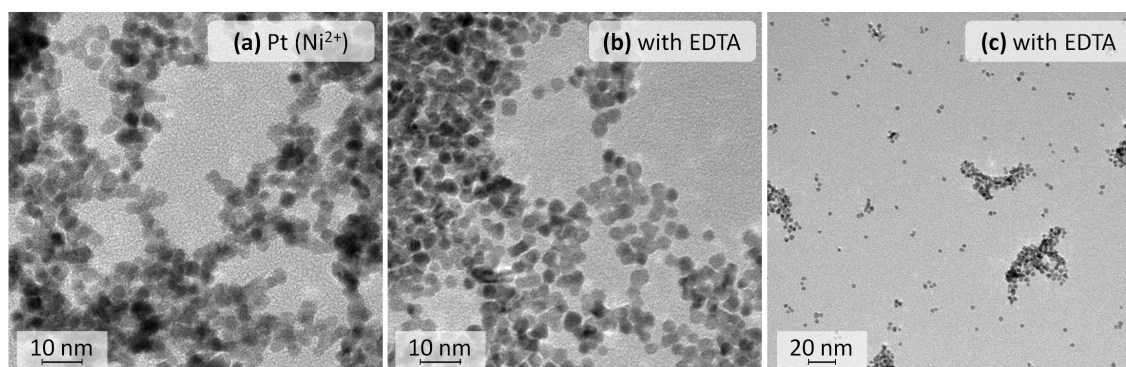
Figure 2.13.: *TEM images of Pt (Ni²⁺) aerogel (a) and a corresponding hydrogel after treatment with the strong complexation agent EDTA (b, c). A loose structure and a large number of unattached spherical particles as well as dimers and trimers are observed in the EDTA treated hydrogel sample. Still, no complete decomposition of the network structure is caused by the competitive complexation agent and the influence of EDTA on the stability of the network remains uncertain.*

(5) The optical properties of Au NPs were used to monitor the gel formation. Therefore, small amounts of AgNO₃ were added stepwise to an Au NP solution and the formation of the network structure was investigated by means absorption spectroscopy. The results are summarized in Figure 2.14. Changes of the optical properties especially the shift of the SPR may give some indication on the size and aggregation of the nanocrystals. The initial NP solution shows a single maximum at 515 nm corresponding to the SPR of the individual spherical Au NPs. Already after the first ion addition step the absorption of the solution at longer wavelengths (> 600 nm) increases markedly and the SPR maxima is slightly red-shifted. With higher ion concentration the intensity of the SPR peak at about 520 nm is further decreased which is accompanied by an increased absorption at longer wavelengths. The absorption peak at 520 nm corresponds to the SPR of single particles not agglomerated yet as well as to the transverse direction of plasmon resonance of the Au nanowires, while the enhanced flat absorption in the region above 600 nm may arise from the longitudinal mode of SPR of nanowires with many different lengths. With increasing ion concentration the formation of nanochains and coalescence of NPs further proceeds.Finally, agglomerates start to settle down in solution which leads to an overall drop of the absorbance as shown at an Ag⁺ concentration of 1.21 mM in Figure 2.14. As already discussed in Chapter 2.1.4 similar investigations concerning the change of absorption spectra due to coalescence of Au NPs into nanochains with various length and network structures are described in the literature.[40,105–107]

To sum up, the mechanism of NP destabilization and gel formation by the addition of transition metal ions was not completely clarified by the experiments. It is assumed that complex formation between citrate molecules and transition metal ions plays a major role
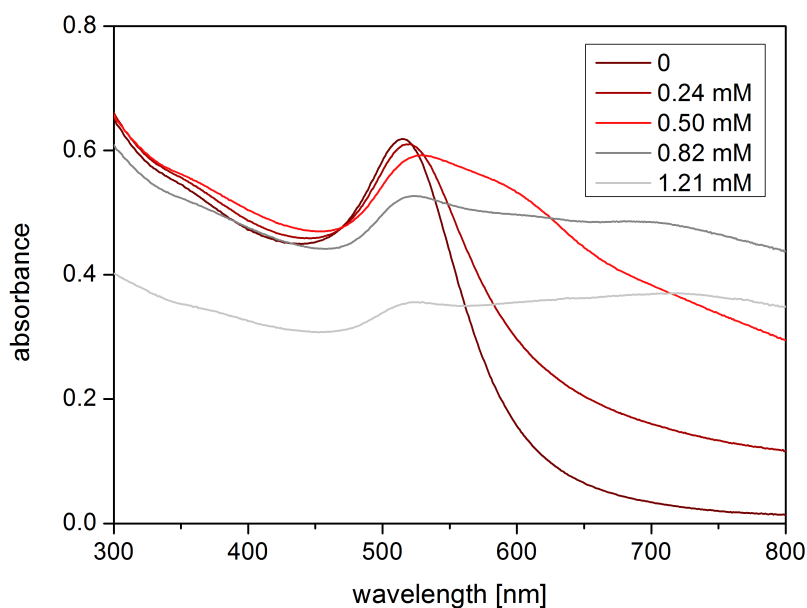
Figure 2.14.: *Evolution of the absorption spectra of Au NP solution after stepwise addition of AgNO$_3$. The final concentration of Ag$^+$ in solution is given in the key of the diagram. Whereas the absorption peak related to the SPR of the spherical NPs drops down, flat absorption at longer wavelengths is observed which is attributed to the formation of elongated nanochains with various lengths. At higher Ag$^+$ concentration the agglomerates settle down in solution which leads to an overall drop of absorption.*

in the process. But still it remains unclear whether these complexes are present in solution leading to coalescence and agglomeration of particles due to the low amount of stabilizing molecules or the particles are bridged by citrate metal complexes still bound to the metal surface. A quantitative proof of the transition metal ions within the hydrogel or aerogel structure is highly challenging due to their very low absolute amount and the possible interference with impurities. Moreover, a spatial localization of transition metals would be necessary in order to make sure that they are incorporated into the nanostructure instead of being adsorbed to the metal surface or being part of co-precipitated salts.

At least in the case of Au (Ag$^+$) gel structures a strong linear welding of the NPs is observed in TEM and confirmed by the evolution of the absorption spectra. It seems that welding of particles into elongated nanochains and agglomeration of particles forming loose connections is different for different structures and probably even not uniform within one sample. In addition, it has to be taken into account that the coalescence of NPs can proceed even further within the nanostructured network. So for example the particles may get into contact first by citrate-ion bridges or by agglomeration and later are welding to interconnected nanochain-like structures by atom diffusion processes. Regarding this point, it should also be underlined that thermal annealing of aerogels lead to strong coalescence of particles resulting in elongated nanochains which are comparable to materials obtained by the temperature-controlled approach described in Chapter 2.1.

2.3. Monometallic aerogels from glucose-stabilized nanoparticles

2.3.1. Metallic nanosponges from glucose-stabilized nanoparticles

For the preparation of metal NPs in aqueous media a wide range of organic molecules providing charge stabilization of the particles and preventing their agglomeration is available. At the same time, the long-term stability of particles strongly depends on the parameters and conditions used during the preparation and on the properties of the resulting colloidal solution. For example the variation of synthesis parameters may cause the formation of either stable, spherical NPs or their aggregation and cross-linking which lead to formation of nanowires and nanostructured networks as it was shown in the case of glucose stabilized metal nanoparticles by QIN et al.[40,104] They present a template-free approach for the preparation of mesoporous gold sponges by assembly and sequential linear welding of Au NPs.[40] In the synthesis described glucose acts as both, mild reducing agent and stabilizing molecule. Depending on the pH value of the solution either stable Au NPs or a three-dimensional, self-supporting and porous network is formed. The authors suggest that in alkaline glucose solution the particle surface seems to be partially unprotected and the particles undergo a welding process into nanowires and further cross-link to a three-dimensional network. The resulting nanosponges reveal an inner surface of 11.9 m^2/g and a large number of grain boundaries within the nanowires. In addition the change of microstructure and pore size after applying of different annealing conditions was studied by the authors.

Another approach was used by QIN et al. for the preparation of Pt nanowires and networks.[104] While glucose still acts as stabilizing agent, sodium borohydrid was used for the reduction of the metal salt. Herein, the molar ratio of metal salt and reduction agent plays the major role for the formation of either monodisperse spherical NPs or their self-organization into nanowires. In the case of a molar ratio [NaBH$_4$]/[Pt^{4+}] < 2 the Pt NPs that were formed in the beginning subsequently undergo a linear self-organization into stable particle-linked Pt nanowires and the color of solution turns from brown to gray in about 20 hours. In addition to the description and the analysis of the preparation pathway the authors also investigate the catalytic activity of NPs and nanowires prepared by their approach towards the reduction of nitrophenol and potassium ferricyanide. It shall be noted that in the absence of any stabilizing agent similar approaches for the preparation of porous metallic nanostructures by rapid reduction processes were described in the literature e.g. by KRISHNA et al.[41] and ZHU et al.[42] Furthermore, nanoporous gold sponges with similar morphology prepared without the use of stabilizer molecules exhibit promising activity in the SERS applications as described in the literature.[108] Moreover, the reduction of metal salt by glucose solution and pH dependent design of structure morphology was also assign to silver nanostructures which are applied for the preparation of SERS substrates.[109]

2.3.2. Adopting the approach for the preparation of monometallic aerogels

Both preparation pathways described above were adopted in order to prepare monometallic networks of nanowires and transfer them into solid aerogel monoliths by supercritical drying. Within the frame of experimental studies several preparation conditions were tested in order to optimize the synthetic procedure of hydrogel structures. The solvent exchange and drying procedure were performed according to approved methods. The results from SEM and TEM characterization of an Au aerogel are shown in Figure 2.15. The hydrogel was obtained by adding a defined amount of Au salt into an aqueous solution of glucose with an initial pH of 12.2. By this approach the hydrogel was formed immediately and settled down in solution after several minutes. The SEM images of the corresponding aerogel (Figure 2.15 (b, c)) show a homogeneous and porous network of nanowires. However, the diameter of segments is quite large. This is also confirmed by the TEM analysis as shown in Figure 2.15 (a). Here, the irregular shape of the nanowires and their diameters in the range of 8 to 25 nm become more obvious. Nevertheless, regarding their grain size these materials are still ahead compared to Au aerogels obtained by the controlled destabilization of citrate-stabilized Au NP by the addition of destabilization agents such as H_2O_2 as described by BIGALL et al.[84] In that work the diameter of the obtained nanowires was hundreds of nanometers and therefore much larger than the size of the initial NPs (3-6 nm). To conclude, the approach based on the pH dependent morphology control of glucose-stabilized Au nanostructures provides a template-free, facile and fast method for the preparation of monometallic Au aerogels with improved quality.
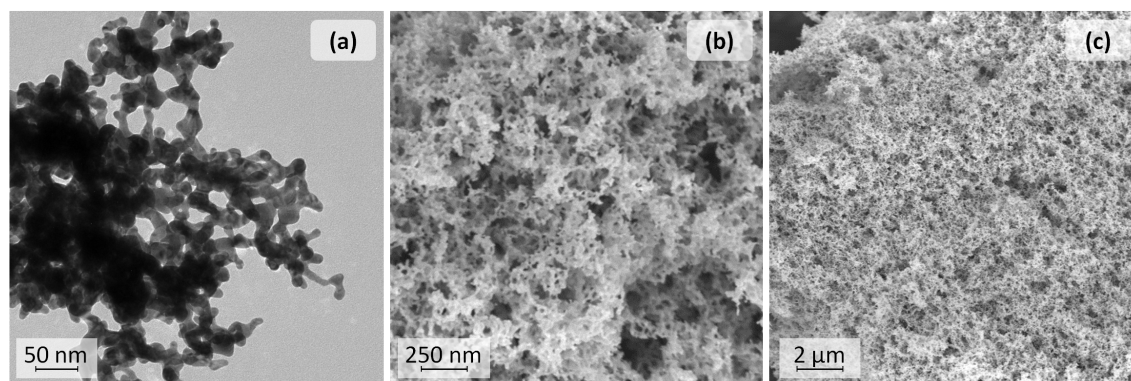
Figure 2.15.: *TEM (a) and SEM (b, c) images of Au monometallic aerogels obtained from glucose-stabilized NPs. A porous and homogeneous network structure was obtained even though the nanowires show a broad size distribution in the range of 8 to 25 nm.*

Likewise, the formation of Pt nanowires as described by QIN et al.[104] was successfully adopted for the preparation of monometallic aerogels. Optimal conditions were found to be realized by a $[NaBH^4]/[Pt^{5+}]$ ratio of 0.85 and hydrogel formation is observed within several hours. First a thin layer is formed on the bottom of the glass bottle which agglomerates to a compact monolith after gently shaking. The structure of the resulting aerogels is presented in Figure 2.16. As determined from TEM images elongated nanochains with

a diameter of about 6 nm are formed and a highly porous network of filigree nanowires is confirmed by SEM. In lower magnification images conspicuously coiled and stable layers of the porous network with a thickness of 10 μm and more are found in several areas of the sample. This property might be advantageous for the preparation of thin film coatings using this approach. To sum up, the synthesis protocol developed for monometallic Pt aerogels stands out due to a fast and facile preparation pathway which leads to a highly porous network of nanowires with thin diameter and strong coalescence of its building blocks.
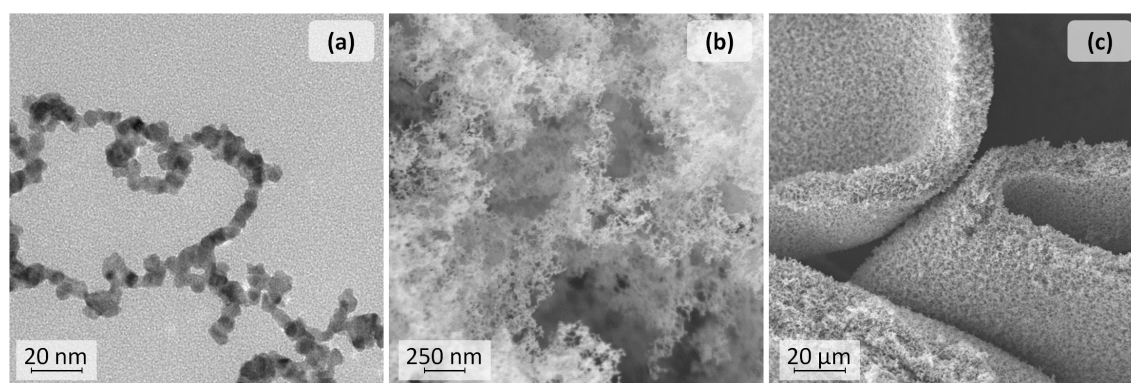
Figure 2.16.: *TEM (a) and SEM (b, c) images of a Pt aerogel structure prepared by addition of low amounts of reduction agent using glucose as stabilizing agent. Elongated nanowires with a diameter of about 6 nm and a porous and filigree network are obtained.*

2.4. Conclusion and perspective

The sol-gel approach opens up the possibility of a template-free synthesis of three-dimensional, porous, metallic superstructures by the self-assembly of noble metal NPs. The controlled destabilization and coalescence of the nanosized building blocks leads to the formation of a self-supporting network of interconnected, interwoven and branched nanochains which exhibits macroscopic dimensions but a structuring on the nanometer scale. In order to remove the solvent from the porous structure which is formed in solution the cold supercritical drying technique is used. Since the fine and fragile structure as well as the high porosity of the gels are retained during this process, the obtained solid materials are named aerogels. These are versatile materials with exceptional properties and a broad range of promising application fields. For many of these application purposes the control of properties, scale and quality of the materials are crucial requirements. In order to face these various demands several methods for the preparation of NP-based metallic aerogels were developed and the synthesis conditions were optimized, respectively. The structure morphologies of the gained materials were characterized by means of electron microscopy and the evolution of structure was additionally monitored via absorption spectroscopy. It should be emphasized that all methods described in the present work are characterized by the high yield of porous metals since the initial NPs are completely transferred from the

solution into the network structure.

Highly porous aerogels which stand out due to strong merging of NPs are prepared by a spontaneous gel formation process without the addition of any destabilization agent. Noble metal NPs are prepared in aqueous media, and subsequently a strong increase of particle concentration and several washing steps are realized by filter centrifugation of the colloidal solution. The created conditions lead to the controlled destabilization of NPs and their coalescence and merging into nanochains which have a similar diameter compared to the initial NPs and are forming a three-dimensional network. Regarding the optimization of synthesis conditions, temperature was found to be a powerful tool to reach a controllable acceleration of gel formation and thereby a strong improvement of reproducibility of the preparation pathway. In the case of the temperature-controlled approach the preparation of multimetallic materials is in focus of investigations since synergetic effects are expected by the interaction of several kinds of metals which may improve their performance in application. Multimetallic structures can be easily prepared by mixing the highly concentrated solutions of different preformed, monometallic NPs and performing a joint gel formation. The elemental ratio of the final gels is equal to the metal ratio of the initial NP solution mixture and hence, can be tuned reliably. For Au, Ag, Pt, and Pd all bimetallic (and even multimetallic) combinations can be realized (except the Au-Pt structure) by this approach. It shall be noted that TEM analysis points out the different morphologies of the nanochains obtained depending on the metals which are combined. The polycrystalline structure of the materials is proven by the formation of rings instead of separated spots in the electron diffraction patterns. This was further underlined by HRTEM which also shows variety of grain boundaries and the coalescence of the initial NPs within the nanochains without the help of linkers or other supporting materials. Furthermore, the large-scale, three-dimensional and highly porous structures of the metallic aerogels are investigated by means of SEM. Here, comparable and homogenous results are obtained for all bimetallic materials investigated. To gain insight into the mechanism of gel formation the evolution of the structure was monitored by absorption spectroscopy and TEM. Therefore, samples were taken repeatedly from a mixed solution of Au and Ag NPs kept at 75 °C. The initial solution shows two separated maxima which correspond to the SPR of spherical Au and Ag NPs, respectively. Already after the first minutes, short but elongated nanochains are formed which is confirmed by both TEM images and the raise of a broad and flat absorption at higher wavelengths. With increasing reaction time the fragments are interconnected to form a network and the surface of the formed nanochains is smoothed remarkably. To further shorten the reaction time and extend the scope of preparation an alternative synthetic procedure was evolved. It provides a fast gel formation process which can be realized within minutes or seconds instead of hours or days whereas no elevated temperature is needed.

The controlled destabilization of the citrate-stabilized NPs is achieved by the addition of small amounts of transition metal ions which are believed to interact with the stabilizing agent by complexation. For Au, Pt and Pd NP solutions as well as for their bimetallic mixtures the gel formation was performed by the addition of four different kinds of metal ions

(Ni^{2+}, Cu^{2+}, Fe^{3+}, Ag^+), respectively. The resulting network structures look quite different as revealed by TEM analysis. In many examples the nanoparticular building blocks do not only form elongated nanowires but also agglomerated structures of irregular size. Although structural variety was observed in TEM the corresponding SEM images illuminate the highly porous and homogeneous network of nanochains within the resulting aerogels. Moreover, it was shown for one example that the material properties can be markedly improved by annealing of the sample under mild conditions and thereby promote/forward the welding and interconnection of the nanosized building blocks. It should be emphasized that the structure of the Au (Ag^+) aerogel differs since it provides a network of continuous nanowires with diameters of about 5-8 nm without further treatments. Due to this, the ion-induced approach is up to now the most suitable method for the preparation of monometallic Au aerogels with respects to prevention of preagglomeration of particles and achievement of high porosity. Furthermore, the formation of an Au-Pt aerogel was accomplished by the addition of transition metal ions which was not realized in the temperature-controlled approach. Nevertheless, the corresponding structure shows agglomerated parts and synthesis conditions have to be further improved. The ion-induced gel formation is a universal approach which enables the preparation of monometallic as well as multimetallic structures whereas the elemental compositions of the nanostructures can be tuned by controlling the ratio of different monometallic NPs in the initial solutions. Moreover, promising results concerning simplification and up-scaling of the preparation of NP-based aerogels are achieved since even lower particle concentrations which can be reached by rotary evaporation of the solvent are suitable for gel formation by the ion-induced approach. Furthermore, the approach introduces the possibility to use NPs with a considerable larger diameter as building blocks for the gel network. The unraveling of the reaction mechanism which finally leads to gel formation remains a challenging task. It cannot be simply assumed that citrate is partially removed from the particle surface via the interaction with the metal ions. Another mechanism could be that the metal ions act as interparticle bridges which connect the neighboring NPs by interaction and complex formation with the citrate molecules on the particle surface. However, analysis of structural data could not provide conclusive results because it seems that welding of particles into elongated nanochains and agglomeration of particles forming loose connections is different for different structures and probably even not uniform within one sample. In addition, it has to be taken into account that the coalescence and merging of NPs can proceed even further within the nanostructured network. In order to assess the interaction between metal ions, citrate molecules and noble metal NPs several issues are discussed as for instance the influence of ionic strength and citrate concentration, the concentration of metal ions needed to induce the gel formation, the partial decomposition of the structure by EDTA, and the evolution of the absorption spectra of a Au NP solution after stepwise addition of Ag^+ ions. In summary, it has to be admitted that the mechanism of gel formation was not completely clarified by the experiments und is still under investigation.

Both the temperature-controlled and the ion-induced approach make use of stable colloidal solutions as an intermediate stage which provides flexibility and control of e.g. size and elemental ratio of the initial building blocks. Since NP synthesis and gel formation

are separated and constitute independent synthesis steps these methods are named as two-step approaches.

For the preparation of monometallic Au and Pt nanoporous metals from glucose-stabilized NPs several approaches were adopted from the literature.[40,104] These methods can be referred to as one-step approaches since the synthesis conditions of the colloidal solutions were tuned to reduce the stability of particles from the outset which results in formation of nanochains and porous networks without further treatments. The increase of the pH value is crucial for the spontaneous formation of Au networks whereas the ratio of metal salt and reducing agent is the key to control the resulting structure in the case of Pt. The SEM images of the Au aerogel show a homogeneous and porous network of nanowires although the diameters of the segments are quite large as revealed from TEM. With nanowire diameters in the range of 8 - 25 nm the structure provides thinner building blocks compared the network obtained from destabilization of citrate-stabilized Au NPs by the addition of destabilization agents such as H_2O_2. In summary, this technique provides a facile and fast method for the preparation of monometallic Au aerogels with improved quality. Moreover, the Pt aerogel prepared by addition of low amount of reduction agent using glucose as stabilizing agent shows elongated nanowires with a diameter of about 6 nm and a porous and filigree network. In addition stable layers of the porous network with a thickness of 10 μm and more are found in several areas of the sample which might be advantageous in the case of film preparation. To sum up, a fast and facile preparation pathway which leads to a highly porous network of nanowires with small diameter and strong coalescence of its building blocks was developed. Even though the versatility of the approach is limited up to now an extension seems suitable as for instance the formation of an Ag sponge by a similar method was already described in the literature.[109]

Even though a lot of work has already been done and synthesis methods described in the present work and in the literature are manifold there are still further tasks to be addressed concerning the preparation of metallic aerogels and the tuning of their properties. Synthesis conditions should be modified in order to gain control of the network morphology e.g. regarding porosity, pore size and density of branching points. The variation of the diameter of the initial particles over a broad range and the combination of particles with different sizes could be applied in order to tune the diameter and branching of nanochains. As discussed above first promising results for this attempt have been achieved by the ion-induced approach. Beyond tuning the size of the initial building blocks future preparation strategies may also address their shape and crystallinity. A strong effect on the morphology, surface, and optical properties depending on the shape of the initial building blocks has already been demonstrated in the case of CdSe nanocrystal-based aerogels.[110] Moreover, the use of monocrystalline NPs with desired sizes and facets and the control of their oriented assembly within the gel structure may results in enhanced catalytic activity and/or selectivity. Nevertheless, the evaluation of suitable conditions to perform controlled destabilization of capped NPs or to control the orientation of crystals during the agglomeration remains highly challenging issues.

Furthermore, the necessity of chloride-free preparation pathways for noble metal aerogels used in electrocatalysis is an important topic to be discussed since chloride impurities promote corrosion and degradation effects and block the noble metal surface which causes performance losses.[111,112] Moreover, the introduction of non-precious metals like Ni, Co, Cu and Fe into Pt or Pd NP-based aerogel structures is in focus of research since these materials are very promising candidates in electrocatalysis.[113,114] Using a one-step gel formation approach PdNi aerogels were obtained by the coreduction of both metal salts in the absence of any stabilizing agent.[93] Moreover, Pt_3Ni NPs were prepared in organic media according to the literature[115] and the initiation of gel formation by phase transfer into the aqueous phase was intended. This approach was adapted from the successful hydrogel formation from PbS and PbSe nanocrystals by phase transfer using 3-mercaptopropionic acid (MPA) as stabilizing agent in the aqueous phase.[116] Even though the phase transfer succeeded no controlled destabilization of particles and formation of a porous networks was achieved in the case of Pt_3Ni NPs, yet. Thus, further efforts for the preparation of mixed noble and non-precious metallic aerogels are required. Finally, it should be taken into account that the modification of structure can be also realized by post-synthetic treatments instead of changing of synthesis conditions. Suitable examples are thermal treatment under inert condition or in the presence of reactive gases as well as inclusion or linking of functional units by infiltration of the gel samples or by co-precipitation on suitable substrates.

Chapter 3.

Structural investigations and modifications

The unique properties of NP-based aerogels and the established variety of preparation pathways have already been outlined in the previous chapters. However, a detailed knowledge of the structural characteristics and peculiarities of the prepared nanostructured materials forms the basis for understanding of the resulting material properties as well as for gaining insight into the processes and interactions that occur during the formation of the three-dimensional network. Moreover, evaluation of these characteristics further allows for the assessment of promising application fields and for designing of suitable modifications and tuning procedures. It shall be noted that the structure of a material could be explored concerning different properties and scales. Within this chapter mainly the investigation of the porosity of the material, its crystallinity and the elemental distribution within the network structure will be addressed.

For the application of porous metals in catalysis or sensors technology a high inner surface area as well as the accessibility of the metallic surface for reactants or analytes needs to be ensured. For these reasons, the inner surface areas as well as the pore size distributions of metallic aerogels were studied by means of N_2 physisorption. Beyond that, the density and porosity of the materials were evaluated. Furthermore, the thermal stability of the aerogels and the feasibility of structural modification by specific heat treatment are part of the research. The modifications aim at the tuning of the nanochain diameters and the pore sizes whereas the thermal stability might be a crucial parameter in the case of gas phase reactions or activation processes. In conclusion, the inner surface area and porous structure of metallic aerogels are in the focus of the first part of the chapter. Furthermore, the second part deals with one of the basic and at the same time most striking questions which is about elemental distribution, interdiffusion and alloying of both noble metals in a bimetallic aerogel structure that has been prepared by the 2-step approach. In the beginning of the gel preparation pathway colloidal solutions of different monometallic NPs are mixed in a defined elemental or volume ratio. Depending on the interaction of these nanosized building blocks, different models for the resulting network structure can be supposed which are schematically represented in Figure 3.1.

During the preparation of hydrogels no hints for the formation of separated networks, e.g. by delayed gel formation of one of the components, was observed. Furthermore, the analysis of multimetallic aerogels by spatially resolved SEM EDX mapping reveals the homogeneous distribution of all metallic components in the structure.[20,84] Based on these results the formation of separated networks or monometallic domains in the size range of 100 nm can be excluded. Nevertheless, it is still an open question whether gel formation leads to directed or random assembly of NPs and whether the fusion of nanocrystals

is accompanied by the formation of an alloy. Inhomogeneities and intermediate stages e.g. partially alloyed segments as well as various structural peculiarities are feasible and should be part of the investigations. The spatial distribution of the metals within the nanochains may give important hints to the mechanism of gel formation. Furthermore, the alloying of metals or preservation of separated phases is a highly important parameter for many application fields e.g. the catalytic activity of the materials.
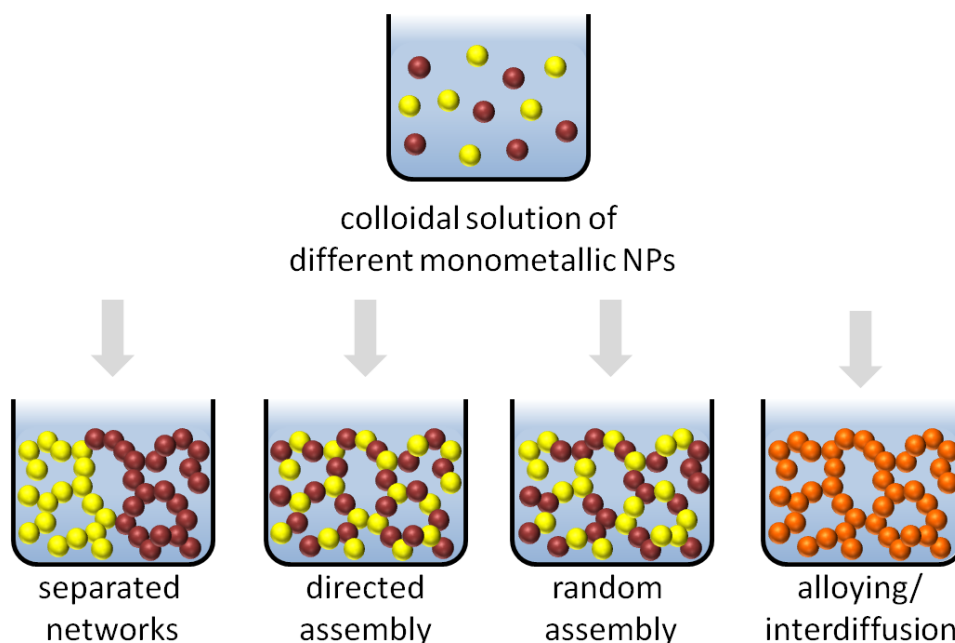
Figure 3.1.: *Schematic illustration of possible structures of the gel network. Whereas the formation of separated networks is excluded by former investigations, the determination of directed or random assembly of NPs and the formation of alloyed structures from the monometallic building blocks are still open questions to be answered by suitable characterization techniques.*

In general, bimetallic aerogels that were prepared by the temperature-controlled two-step approach are in the focus of the presented investigations. Details concerning the preparation pathway can be found in Chapter 2.1. The whole set of analytical methods used to examine the assembly and elemental distribution of the nanostructures is summarized in Table 3.1. These investigation methods are highly suitable for nanosized structures and metallic crystallites and can be classified by the kind of material property which is used to gain information about the structure, the contained elements and their distribution (see Table 3.1).

The analysis of lattice distances by high resolution TEM (HRTEM) has already been performed for an Ag-Pt aerogel sample as described by BIGALL et al.[84] In the investigated area separated Ag and Pt domains within the elongated nanochains were found

Table 3.1.: *Analytical methods applied for characterization of bimetallic aerogels. They are classified according to the material properties which are used in order to gain information about the structures and the elemental composition/distribution.*

Material property	Analytical methods
Array of atoms in a crystal lattice and parameters of this lattice	HRTEM, powder XRD
Inelastic interaction with radiation and element-specific characteristic energy levels of bond electrons	SEM EDX, EXAFS, Analytical TEM: STEM EDX, (EELS/EFTEM)
Difference of the atomic weight (Z-contrast)	HAADF STEM

and the structure was suggested to be formed without further alloying of metal components. In the above-mentioned publication also Au-Ag aerogel nanochains are analyzed by HRTEM but it had to be stated that the crystallographic parameters of the face centered cubic (fcc) crystal structures of Au and Ag are very similar which makes them crystallographically nearly non-distinguishable.[84] In the following subchapters, background information and measurement results concerning powder X-ray diffraction (XRD), extended X-ray absorption fine structure (EXAFS) analysis, analytical TEM and high angle annular dark field (HAADF) scanning transmission electron microscopy (STEM) are presented and discussed in detail. In the conclusion of the chapter the correlation of results gained by different characterization techniques is highlighted.

3.1. N_2 physisorption and density evaluation

3.1.1. Background

Adsorption processes can be classified into physisorption and chemisorption depending on the kind of physical and chemical interactions between the solid phase named as adsorbent and the gas phase in the adsorbed state named as adsorptive.[117] In physisorption processes the components are interacting via weak and non-specific van-der Waals forces. The adsorption enthalpy is typically below 40 kJ/mol and multilayer adsorption occurs. In contrast, specific interactions and covalent bonding are involved in chemisorption processes and therefore only a monolayer of adsorbed molecules is formed. Due to this, physisorption measurements with gases like N_2 or Ar are used to characterize the internal surface area, pore volume and pore size of materials whereas chemisorption with e.g. CO or H_2 can be applied to determine the number and structure of reactive centers on the surface of a material.
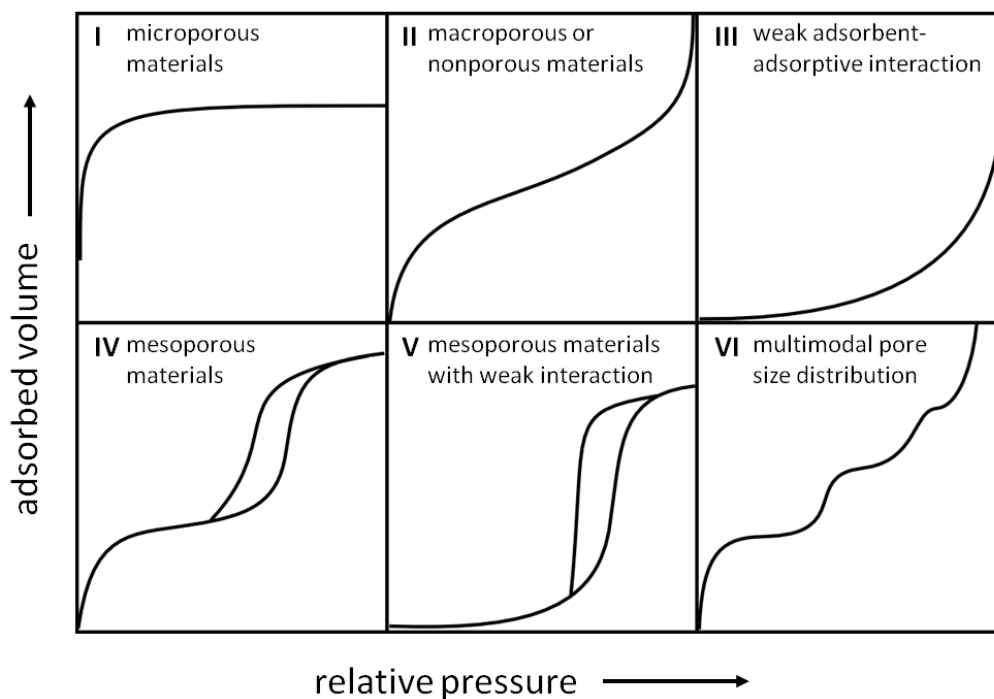
Figure 3.2.: *Types of adsorption isotherms according to IUPAC convention.*[118] *The shape of isotherms depends on the pore size of the adsorbent and the adsorbent-adsorptive interactions.*

In a typical N_2 physisorption experiment the activated sample is cooled down to the boiling point of N_2 (77 K) and small amounts of N_2 are dosed stepwise to the sample. After reaching the equilibrium state at each step the resulting pressure and the adsorbed volume are measured. In order to investigate the desorption process the sample is also degassed afterwards. The plot of the adsorbed volume versus the obtained pressure measured at a constant temperature results in the adsorption isotherm. A relative pressure given by the ratio of the obtained pressure to the saturated vapor pressure of the adsorptive at the given temperature is commonly used to ensure comparability. According to the guidelines published by the IUPAC in 1985 there are 6 different types of adsorption isotherms which are displayed in Figure 3.2.[118] The shape of isotherms strongly depends on the structure and the pore size of the adsorbent and the adsorbent-adsorptive interactions. Furthermore, pore sizes were classified into micro- ($< 2\,$nm), meso- (2-$50\,$nm), and macropores ($> 50\,$nm) by the IUPAC convention.[118] The shape of type II isotherms result for macroporous or nonporous materials with high external surfaces e.g. nanoscaled materials, such as inorganic nanoparticles. In these systems multilayer adsorption is observed and interparticular capillar condensation occurs at a high relative pressure.

In mesoporous systems pore condensation takes place at low relative pressure and determines the shape of the adsorption isotherms. At a certain pressure the multilayer film on the pore walls cannot be stabilized any longer and pore condensation occurs. By the formation of a concave meniscus the vapor pressure of the liquid is decreased and the condensation of the adsorptive leads to complete filling of the pores. Due to the higher den-

sity of the liquid the adsorbed volume is increased at constant pressure. For mesosporous materials a hysteresis loop between adsorption and desorption branch is observed. The adsorption branch is delayed and therefore shifted to higher relative pressures due to the metastability of the adsorbed film. Hence, the desorption branch is commonly used for evaluation since it represents the equilibrium state of transition. The Kelvin equation expresses the relation between the relative pressure and the radius of the meniscus r_m

$$ln\frac{p}{p_0} = \frac{-2\gamma V_M}{r_m RT} cos\varphi \tag{3.1}$$

γ = surface tension, φ = wetting angle, V_M = molar volume of the adsorbate

Meanwhile, the pore radius is given as the sum of the meniscus radius rm and the thickness of the pre-adsorbed multilayer t:

$$r_{pore} = r_m + t \tag{3.2}$$

The multilayer thickness of the adsorbate on a flat surface in dependence of the relative pressure is given by the empirical determined Wheeler equation:

$$t = 4.3 \left(\frac{5}{ln\frac{p}{p_0}}\right)^{\frac{1}{3}} \tag{3.3}$$

Based on this knowledge the Barett-Joyner-Halenda (BJH) approach can be used to determine the pore size distribution of mesoporous materials.[119]
Nevertheless, the BJH method suffers from several restrictions since it does not take into account the difference of the thermophysical properties of the adsorbed fluid and the bulk liquid as well as the deviation of the multilayer thickness for small pores. To overcome these problems microscopic methods based on the density functional theory (DFT) have been developed[120] as for example the quenched solid DFT (QSDFT) approach.[121] Nevertheless, the sets of theoretical local isotherms (kernels) needed for QSDFT calculations are only available for some particular material classes and defined pore geometries. In addition, the approach is mainly developed for micropores and small mesopores and its applicability is therefore limited.

The specific surface area of mesoporous materials is commonly determined by the Brunauer-Emmett-Teller (BET) equation[122] given below:

$$\frac{p}{(p_0 - p)\,V_{ads}} = \frac{1}{C \cdot V_{mono}} + \frac{C-1}{C \cdot V_{mono}}\frac{p}{p_0} \tag{3.4}$$

V_{ads} = amount of adsorbed N_2, C = adsorption constant, V_{mono} = volume of a monolayer

The BET theory assumes that an infinite number of layers is formed and that the adsorption energy of the first layer is different from the adsorption energy of the following ones. By plotting $\frac{p}{(p_0-p)V_{ads}}$ versus $\frac{p}{p_0}$ the volume of a monolayer is assessed from the intersection with the y-axis and the slope of the linear function. The linearity of the plot

is limited to $p/p_0 < 0.25$ because adsorbat-adsorbat interactions are not considered by the BET theory. Based on V_{mono} the specific surface area is calculated by:

$$S_g = \frac{N_A \cdot V_{mono} \cdot \sigma_{N_2}}{V_{mol} \cdot m_{sample}} \qquad (3.5)$$

S_g = specific surface area, N_A = Avogadro constant, V_{mol} = ideal gas volume, σ_{N_2} = surface required for a single N_2 molecule, m_{sample} = mass of the sample

3.1.2. Results and discussion[*][†]

As it was revealed by SEM images the nanochains of the gel network offer a system of open pores and tunnels. Inner surface area and pore size distribution were evaluated by N_2-physisorption. The isotherms for N_2 adsorption and desorption for two examples of metallic aerogels are depicted in Figure 3.3. They mainly show a type II behavior with an additional slight accordance to type IV isotherms. The isotherms display a multilayer adsorption behavior, and no plateau is formed for high values of relative pressure which prove the presence of large mesopores and macropores inside the material. The insets of Figure 3.3 show the corresponding cumulative pore volumes calculated from the desorption branch of isotherms applying the BJH theory. In the evaluated range no prevalent pore size is observed, and the distribution is broad and does not reach a plateau. Furthermore, no sharp step corresponding to a specific pore size can be observed. This is in good accordance with the results from SEM characterization which also show the broad pore size distribution and the system of open pores and tunnels. It shall be noted that due to the strong increase of adsorbed volume and the resulting restricted resolution of measurement at high relative pressure the larger macropores of the material cannot be evaluated reliably.

The surface area of the aerogels was determined by a multi-point BET approach. The values for several aerogels prepared by the temperature controlled approach as well as for a Pd aerogels prepared by ion-induced gel formation are summarized in Table 3.2. The specific surface area is given as a mass referred number but also converted into molar values which allow better comparability with the values of other porous metals and aerogel materials. In the case of bimetallic aerogels a weighted molar mass is calculated based on the elemental ratio of metals determined by EDX analysis. Since the content of organic compounds is quite low as revealed by TGA, they are neglected for the calculation of the average molar mass. It shall be noted that surface areas of NP-based metallic aerogels presented here reach values of up to $11 \cdot 10^3$ m³/mol which is quite amazing taking into account a typical surface area for silica aerogels of $36 \cdot 10^3$ m³/mol.[44] As it has already been underlined in Table 1.1, the NP-based gel approach provides exceptional materials which surface areas hardly reached by other preparation pathways for porous noble metals.

---

[*]Parts of this section have already been published.[20]

[†]Physisorption measurements and calculations of pore size distribution and surface area were performed by M. Rose, L. Borchardt and M. Oschatz (Inorganic Chemistry, TU Dresden)
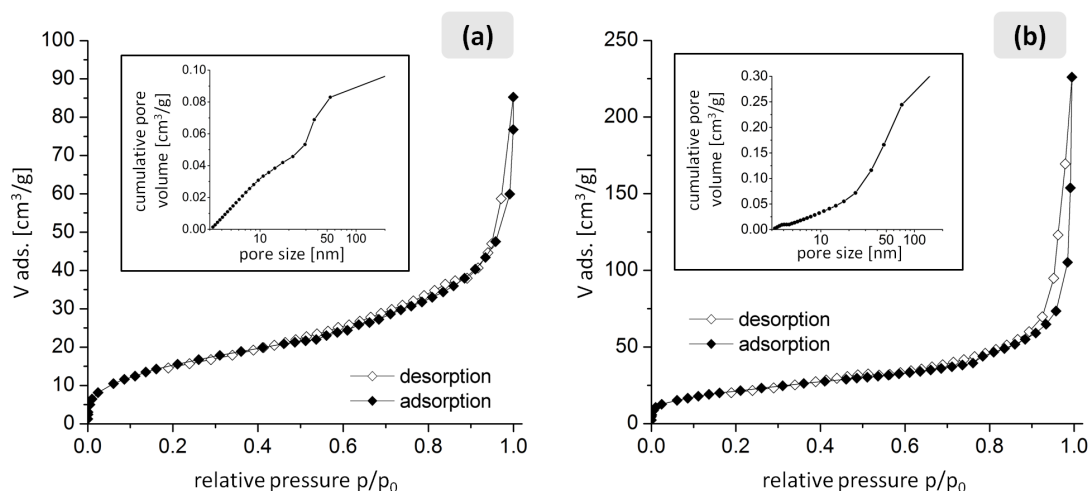
Figure 3.3.: *Nitrogen physisorption isotherms for an Au-Pd aerogel (a) and a Pt-Pd aerogel (b). The presence of large mesopores and macropores can be concluded from the shape of the isotherms. The insets show the corresponding cumulative pore volumes determined by BJH theory. The image was reprinted with permission from reference.[20] Copyright 2014 American Chemical Society.*

Furthermore, the monolith densities of the aerogels are estimated by weighting several monoliths and assessing their spatial dimensions. By this approach the monolith density of the Au-Pd aerogel is estimated to be as low as $0.0238\,\text{g/cm}^3$ which refers to a relative density (monolith density of aerogel/skeletal density) of only $0.16\,\%$. Accordingly, the prepared aerogel is almost 650 times lighter than the corresponding bulk metal. The skeletal density is calculated by taking into account the atomic ratio of metals determined by EDX analysis and the bulk densities of Au ($19.3\,\text{g/cm}^3$) and Pd ($11.99\,\text{g/cm}^3$), respectively. The relative density is closely connected to the porosity ϕ which is as high as $99.84\,\%$ for the evaluated Au-Pd sample.

$$\phi = 1 - \frac{\rho_{monolith}}{\rho_{skeletal}} \tag{3.6}$$

Since the physisorption isotherms of the investigated aerogels show no plateau at high relative pressures, the total pore volumes cannot be calculated from the physisorption data. Hence, the specific total pore volume given here is estimated by calculating the difference of the reciprocal monolith density and the reciprocal skeletal density. Applying this approach a value of $42\,\text{cm}^3/\text{g}$ was obtained for the Au-Pd aerogel. The density and total pore volume of other samples summarized in Table 3.2 are calculated in an analog way, respectively. The pore volume for pores smaller than a certain diameter is determined from the desorption branch of isotherms at a corresponding relative pressure. The volume of mesopores smaller than ~40 nm and even of pores smaller than ~200 nm is obviously below the estimated total pore volume which underlines the conclusion that the porosity of the material is mainly based on huge mesopores and on macropores. The hierarchical pore system might be of great advantage for the transport of analytes or reactants since

Table 3.2.: *Summary of inner surface areas, pore volumes and density values for several kinds of metallic aerogels. [*] density values are determined by averaging over more than 5 samples*

aerogel sample	surface area [m²/g]	surface area [m²/mol]	pore volume for pores smaller than ~40 nm [cm³/g] (pore diam.)	pore volume for pores smaller than ~200 nm [cm³/g] (pore diam.)	monolith density [g/cm³]	relative density	porosity	total pore volume [cm³/g]
Au-Pd	57	8380	0.073 (39 nm)	0.093 (217 nm)	0.024[*]	0.16%	99.84%	42
Pt-Pd	79	10900	0.147 (42 nm)	0.238 (222 nm)	0.033[*]	0.20%	99.80%	30
Au-Ag	48	7020	0.101 (38 nm)	0.333 (189 nm)	0.016	0.11%	99.89%	62
Ag-Pt	46	6970	0.140 (40 nm)	0.199 (213 nm)	0.041	0.26%	99.74%	24
Pd	88	9400	0.466 (43 nm)	1.175 (191 nm)	0.025	0.21%	99.79%	40
Pd (Ni^{2+})	52	5535	0.105 (42 nm)	0.231 (199 nm)	0.044	0.36%	99.64%	23

the diffusion rate through pores with diameter of 10-50 nm approach those of molecules in air.[15] Furthermore, taking into account the high surface area, the extremely low density as well as the prevention of pore blocking by the network of open and interconnected pores and tunnels metallic aerogels are promising candidates for catalysis and sensor applications.

3.2. Thermal stability and structure modification

The investigation of thermal stability of metallic aerogels is of great importance since they might be exposed to elevated temperature in gas phase reactions or activation protocols which are aiming for the removal of moisture or organic residuals in order to clean the metallic surface. In these processes sintering effects and loss of inner surface area need to be avoided. Furthermore, annealing of aerogel solids might be also a tool of post-preparative treatment in order to control the density, ligament diameter and pore size of the materials. The influence of thermal treatment on the network structure and the diameter of nanochains was studied for several bimetallic aerogels and pronounced differences depending on the components, applied temperature and duration of treatment were observed. High thermal stability was verified for Au-Pd and Pt-Pd aerogel specimens which still provide an ultrafine, highly porous network after heat treatment at 300 °C for 30 minutes under argon atmosphere as depicted by the corresponding SEM images (Figure 3.4 (b, d)). Evaluation of TEM (Figure 3.4 (a, c)) indicates a slight increase of diameter of nanochains to 7.0±1.8 nm for Pt-Pd and 6.7±1.6 nm for Au-Pd.
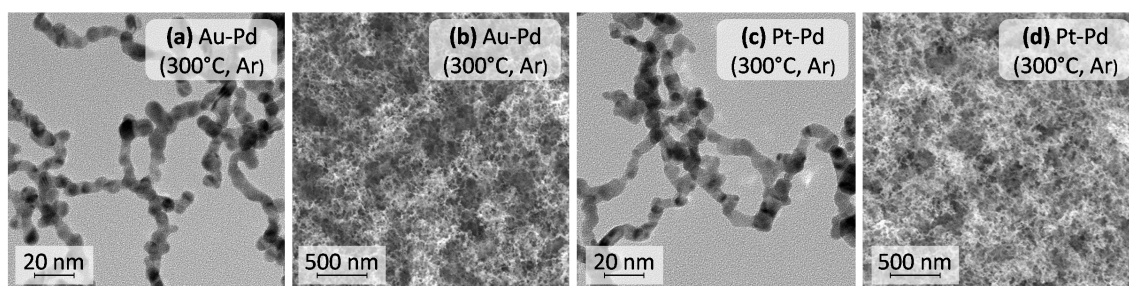
Figure 3.4.: *TEM and SEM images of Au-Pd (a, b) and Pt-Pd (c, d) aerogels after thermal treatment (300 °C, 30 min, Ar atmosphere). The highly porous structure of the material is preserved whereas the diameter of the nanowires only slightly increased compared to the initial nanostructure of the aerogels.*

In contrast, the structure of Au-Ag aerogels is very sensitive to thermal treatment and the appearance of the network can be tuned by this approach. Some examples for the structural changes caused by annealing at 150 °C or 400 °C are displayed in Figure 3.5 (b, c). After 2 hours at 150 °C in argon atmosphere the diameter of nanochains in the Au-Ag aerogel increased to approximately 20 nm and reach maximum values of 40 nm in some segments. It needs to be emphasized that still a network of nanochains is observed and no degradation to a compact or nonporous structure occurred due to sintering and reorganization of the structure. After continuous heating (heating rate 5 K/min) and retaining the sample at 400 °C for 5 minutes in air atmosphere the sintering of nanowires is even more pronounced and a compact, less porous architecture is developed.

It shall be noted that heat treatment at 400 °C for 12 hours also leads to a partial increase of diameter of nanochains and the formation of inhomogeneities within the nanostructure of Au-Pd aerogels. Whereas the fine network structure is retained in some areas of the sample, also strong growth of ligament size occurred in others as revealed by SEM (Figure 3.5 (a)). Both types of structure are distributed irregularly within the network and it seems reasonable that outer parts of monoliths and fragments are affected stronger by the heat treatment.

Structure modifications of nanoporous metals or NP-based aerogels were also described in the literature. For instance, changes of the surface area, crystallinity, and crystal structure as well as an increase of crystallite size after annealing of CdS nanocrystal-based aerogels were performed by MOHANAN et al.[59,123] In addition, to name only one example from the field of nanoporous noble metals, the change of ligament diameter and pore size control by thermal treatment of gold nanosponges are discussed by QIN et al.[40]
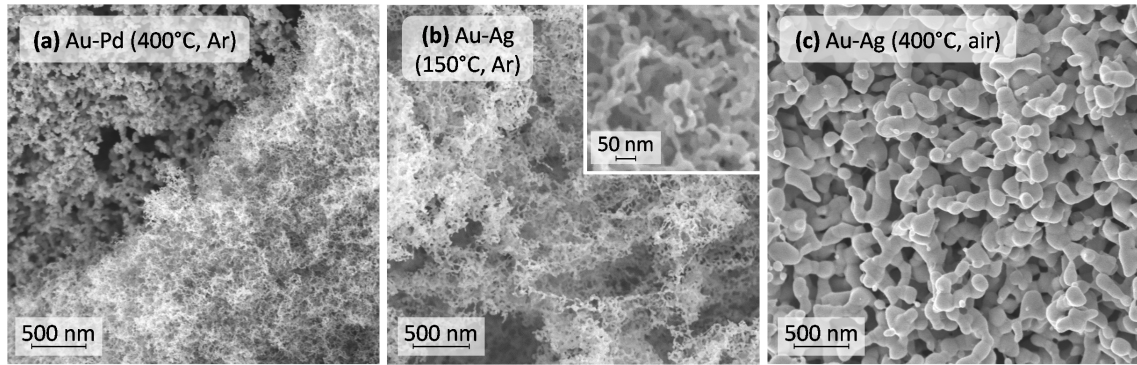
Figure 3.5.: *SEM images of bimetallic aerogels after thermal treatment at different conditions. Sintering of an Au-Pd aerogel at 400 °C for 12 hours under Ar atmosphere leads to a partial increase of the diameter of the nanochains and the formation of inhomogeneities within the resulting nanostructure (a). Thermal treatment of Au-Ag aerogels at 150 °C for 120 minutes causes an increase of the nanochain diameter to ca. 20 nm but even though reorganization occurs still a porous network of nanochains is observed (b). After 5 minutes at 400 °C in air atmosphere the sintering of the nanowires in an Au-Ag aerogel is even more pronounced which leads to a loss of porosity (c).*

3.3. Powder X-ray diffraction

3.3.1. Background

The diffraction of X-rays by crystal lattices was proposed by MAX VON LAUE in 1912 when he recognized that the wavelength of X-rays has the same order of magnitude like the distances of atoms in a crystal and his theory was confirmed by the work of Walter Friedrich and Paul Knipping only some years later.[124] In present-day research X-ray diffraction (XRD) is known to be a powerful and widespread technique for structure determination. Likewise, XRD is commonly used to investigate the solid structure of NPs and nanomaterials.

Due to interaction with the crystal the incident beam is diffracted in a characteristic way, called diffraction pattern. Constructive interference occurs when Bragg conditions are fulfilled:

$$n\lambda = 2\,d\,sin\Theta \tag{3.7}$$

n = order of reflection, λ = wavelength of radiation, d = interplanar spacing, Θ = diffraction angle

Hence, interplanar distances can be calculated by measuring the glancing angles. Different crystal planes result in a set of d values which can be used to determine the space group and the lattice parameters of the crystal. In powder XRD techniques many crystallites with random orientation are investigated in parallel and it is commonly used to identify a phase by comparison of the diffraction pattern with materials listed in appropriate databases. Moreover, the presence of an alloyed structure as opposed to a mixture

of several monometallic phases can be demonstrated by XRD since the diffraction pattern of the physical mixture consist of individual reflections of the two individual monometallic phases and is different from that of a lattice formed by alloying of both metals. The lattice parameter of a solid solution of two phases with similar structures in its ideal form is a linear function of the composition in the range of the lattice parameters of the two constituent phases as described by Vegard's law[125,126]

$$a_{AB} = a_A (1 - x_B) + a_B x_B \qquad (3.8)$$

a_{AB} = lattice parameter of the alloy, a_A and a_B = lattice parameters of the constituent elements, x_B = mol fraction of component B

Since this equation is based on the idea that the cell parameters are a direct consequence of the sizes of the component atoms and it does not take into account the interaction of atoms the ideal behavior is almost never observed.[127]

If the size of crystallites of a powder XRD sample is sufficiently small this will lead to a broadening of the maxima of the diffraction pattern. The relation between crystallite size and reflection broadening is given by the Scherrer equation[128,129]

$$L = \frac{K\lambda}{b \cos\Theta} \qquad (3.9)$$

L = crystallite size, K = Scherrer constant (dimensionless number of the order to unity), λ = wavelength of radiation, b = additional broadening (in radians), Θ = Bragg angle

This correlation is also used to determine the crystallite size of nanomaterials. It should the noted that this value cannot be equated to the particle diameter of multicrystalline NPs or nanocrystals containing several phases and it is not inevitably equal to values determined by other methods e.g. dynamic light scattering (DLS) which evaluates the hydrodynamic radius. The Rietveld refinement is a well established tool for the evaluation of powder XRD measurements.[130,131] This method refines the structural (and instrumental) parameters for each involved phase, based on a given starting model of an assumed structure which is supposed to be close to the actual configuration of atoms in the measured sample, by minimizing the differences between the calculated structure model and the measured diffraction pattern. Crystallite sizes, lattice parameters and a quantitative phase analysis are provided by the output of the refinement.

3.3.2. Results and discussion[‡§]

As it is stated in the beginning of the chapter the phase analysis of multimetallic aerogels is needed to understand the gel formation process as well as the inner structure of the materials and to predict and influence their functionality. Aerogels are multicrystalline

---

[‡]Parts of this section have already been published.[20]

[§]XRD measurements and structure modeling by the Rietveld method were performed by M. Klose and L. Giebeler (Institute for Complex Materials, IFW Dresden)

materials as it was confirmed by electron diffraction and HRTEM and their compressed solid monoliths are suitable samples for powder XRD. Several bimetallic aerogels have been investigated and the Au-Pd system was chosen for further examination of the influence of thermal treatment on the diffusion of the different metals and on the crystallite size by means of XRD. For evaluation of the XRD data the Rietveld method was used with individual structure models for each involved phase.

The analysis of the XRD results is challenging since all metals investigated exhibit a face-centered cubic (fcc) crystal structure and their lattice parameters are quite similar. Furthermore, the small size of crystallites leads to a considerable broadening of the reflections as described by Scherrer equation. In addition, the variety of grain boundaries inside the chain-like structure leads to additional stress and strain inside the crystallites which may result in further reflection broadening. For an Au-Pd aerogel and its thermal modifications as well as for an Ag-Pd and a Pt-Pd sample the observed data, the calculated structure model, and the respective difference plot are summarized in the diagrams of Figure 3.6. In addition, the Bragg positions for each involved phase are shown as small ticks. Moreover, the results of the calculated structure model including phase fractions, lattice parameters, and crystallite sizes are summarized in Table 3.3.

Table 3.3.: *Results of the calculated structure models gained from Rietveld refinement of the XRD pattern of several bimetallic aerogels.*

sample	phase	space group	lattice constant [Å]		Phase fraction [wt%]	crystallite size [nm]
			a	c		
Ag-Pd aerogel (as synthesized)	Ag	F*m*-3*m*	4.0727		67	4
	Pd	F*m*-3*m*	3.9232		32	2
	Ag$_2$O	P*n*-3*m*	4.7961		1	16
Au-Pd aerogel (as synthesized)	Au	F*m*-3*m*	4.0673		68	3
	Pd	F*m*-3*m*	3.8975		32	3
Au-Pd aerogel (300 °C, Ar)	Au	F*m*-3*m*	4.0467		52	5
	Pd	F*m*-3*m*	3.9892		48	5
Au-Pd aerogel (400 °C, Ar)	AuPd	F*m*-3*m*	3.9549		100	15
Au-Pd aerogel (400 °C, air)	Au	F*m*-3*m*	4.0540		48	9
	PdO	P4$_2$/*mmc*	3.0422	5.3370	52	8
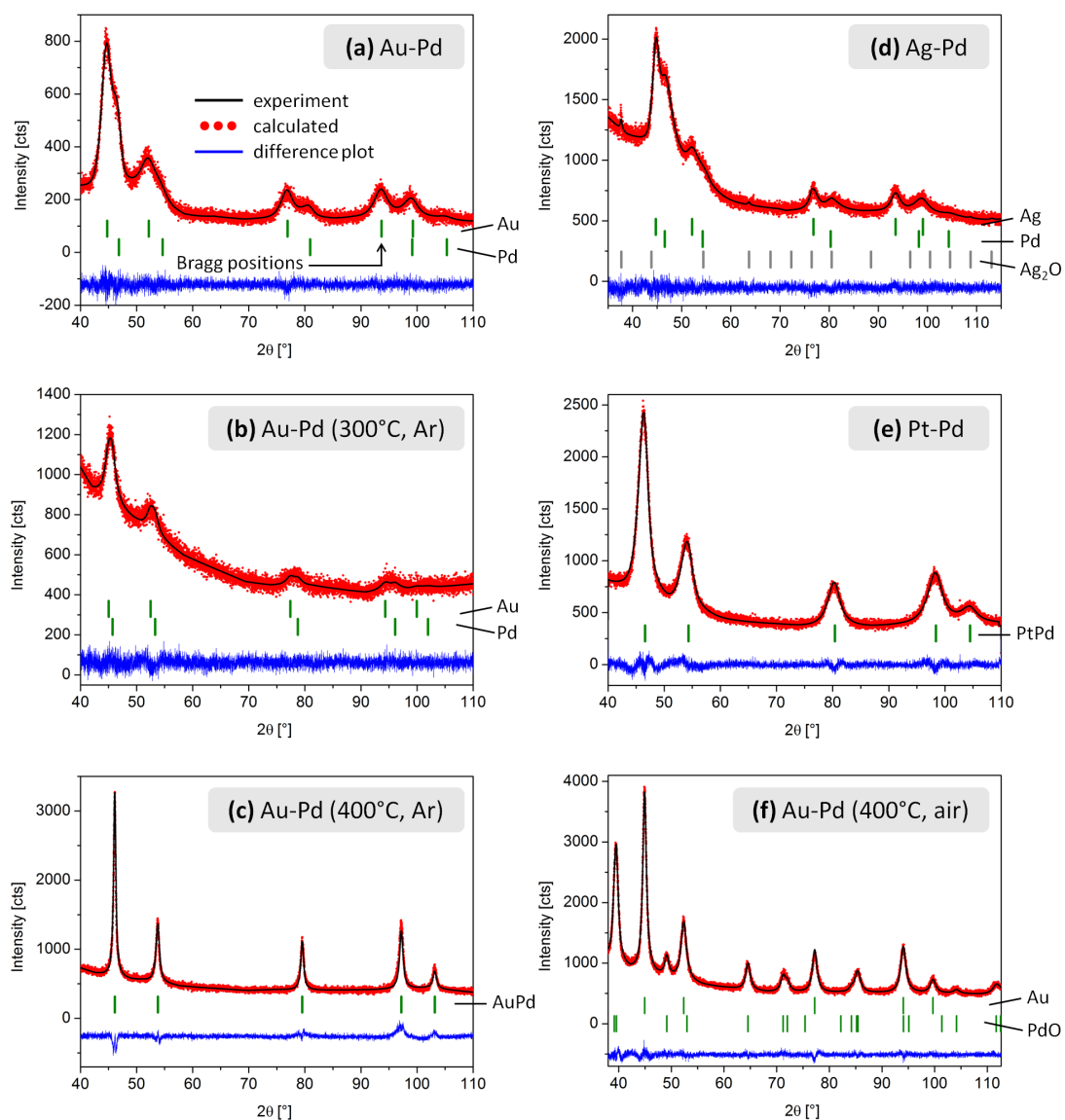
Figure 3.6.: *XRD pattern, calculated pattern from Rietveld refinement, difference plot and Bragg positions for the involved phases for several bimetallic aerogel samples, respectively. Two separated phases in accordance to the contained metals are verified for the as prepared Au-Pd (a) and Ag-Pd (d) aerogels. For Pt-Pd (e) no distinction between an alloyed phase and separated metal phases is feasible based on the XRD pattern. The influence of thermal treatment is studied for several Au-Pd aerogel specimens. After 30 min at 300 °C under argon atmosphere a partial intermixing of phases occurs and the assumption of an Au rich and a Pd rich phase gives best results for fitting the data (b). Moreover, complete alloying of both metals is observed after heat treatment at 400 °C for several hours (c). Reflections become much sharper since the crystallite site increases. After annealing at 400 °C under air atmosphere complete oxidation of Pd and the formation of a PdO phase is clearly visible from the corresponding reflections whereas the reflections for Pd phase disappeared (f). Part of the image were adopted with permission from reference.[20] Copyright 2014 American Chemical Society.*

Based on the XRD pattern of the Pt-Pd aerogel (Figure 3.6 (e)) no reliable phase analysis can be performed. Due to the reflex broadening and the small difference of the lattice parameters of Pt and Pd a clear distinction between separated metal phases and an alloyed phase is not possible. For the same reasons also the XRD pattern of an Au-Ag aerogel does not give a reliable indication about phase composition of the material. In contrast to that, the XRD pattern of an Ag-Pd aerogel (Figure 3.6 (d)) clearly shows separated Ag and Pd phases indicated by reflections at Bragg positions for Ag and Pd, respectively. This is especially evidenced by the well separated reflections at higher diffraction angles ($> 70°$). The average sizes of crystallites are 4 nm for the Ag phase and 2 nm for the Pd phase, respectively. Likewise, also the noble metals in the as prepared Au-Pd aerogel show two separated phases displayed by reflections at the Bragg positions for Au but also for Pd (Figure 3.6 (a)). Crystallite sizes evaluated from Rietveld refinement are 3 nm for both the Au and the Pd phase.

In order to gain interdiffusion of the metals and thereby control the progress of alloying a thermal treatment of the solid samples is applied. Heating the Au-Pd aerogel to 300 °C over a period of 30 minutes leads to obvious changes of the XRD pattern (Figure 3.6 (b)). For this pattern the best fit is obtained by assuming two partially mixed phases, a gold-rich and a palladium-rich one. The lattice parameters of the Au phase is shifted to 4.0467 Å compared to the corresponding value of 4.0783 Å for the pure bulk metal which gives hint to the inclusion of Pd atoms into the Au lattice. At the same time the lattice parameter of the Pd phase shifted to 3.9892 Å compared to 3.8908 Å in bulk Pd which suggest the integration of Au atoms into the Pd crystal structure. The crystallite sizes of both phases only slightly increased to 5 nm and the highly porous structure is retained during the treatment as it is shown in the SEM image in Figure 3.4 (b). Moreover, even a complete alloying of both metals can be reached by annealing at 400 °C for 12 hours under argon atmosphere as it is revealed by the corresponding XRD pattern (Figure 3.6 (c)). Here, only one single AuPd alloyed phase is observed. In addition, the reflections become sharper as a result of crystal growth to a value of 15 nm. A similar low temperature metal interdiffusion and corresponding change of XRD pattern were described by SCHAAK et al. for an Au-Pd nanocomposite after heating to 300 °C. [132] It should be noted that heat treatment of the Au-Pd aerogel at 400 °C for several hours also leads to a partial increase of diameter of nanochains and the formation of inhomogeneities within the resulting structure as described in the previous subchapter. Furthermore, it was proven that annealing of Au-Pd aerogel at 400 °C under air atmosphere caused entire oxidation of palladium. The corresponding XRD pattern in Figure 3.6 (f) shows maxima at Bragg positions corresponding to PdO whereas the reflections for Pd completely disappeared. Meanwhile, the calculated size of crystallites increases to 9 nm (Au phase) and 8 nm (PdO phase), respectively.

The calculated crystallite sizes of the as prepared aerogels are smaller than the size of the initial NPs which correspond to the structural features and variety of grain boundaries within the nanowires observed in TEM. In addition, the fraction of each involved phase is calculated from the structure model (Table 3.3). It shall be noted, that these values cannot be easily compared to the mass fractions of the pure metals determined by EDX analysis

of the corresponding aerogels. For instance EDX analysis states a composition of 44 wt% Au and 56 wt% Pd for the Au-Pd aerogel analyzed by XRD in the as synthesized state and after heating to 400 °C under argon as well as 66 wt% Au and 34 wt% Pd for the sample heated to 300 °C. For the pristine Au-Pd aerogels the phase fractions calculated from XRD pattern strongly differs from the EDX results. One reason might be that interdiffusion of metals already occurred to a certain extend and therefore no values of pure monometallic phases are calculated. This kind of interdiffusion is supposed due to the slight changes of the lattice parameter. Compared to the bulk metals the lattice constant is decreasing in the case of the Au phase and increase for the Pd one. Moreover, the complexity and versatility of the internal structure and phase composition of bimetallic aerogels cannot be considered entirely by the fitting which is based on a simplified model of the structure. Furthermore, the analysis of the measurement patterns suffers from broad reflections, similarity of lattice parameters and huge background and hence, the precision of the fitting is limited. However, XRD offers a reasonable approach in order to evaluate differences in phase composition of the nanostructures as well as the effects of thermal treatment on the alloying of metals. In summary it can be stated that separated metal phases are observed in the initial Au-Pd and Ag-Pd aerogels which are suitable samples for phase analysis by XRD. After applying different thermal conditions to several Au-Pd aerogel samples a stepwise change of diffraction pattern is observed which reveal the gradual alloying of Au and Pd. These are very promising results which express the realization of controlled temperature-induced phase transitions in the structure of multimetallic NP-based aerogels.

3.4. Extended X-ray absorption fine structure analysis

3.4.1. Background

When an X-ray beam passes through a material, its intensity is attenuated by various interaction processes. The absorption is given by the Lambert-Beer equation:

$$\mu \cdot t = log \frac{I_0}{I} \tag{3.10}$$

μ = linear absorption coefficient, t = material thickness traversed, I_0 = intensity of the incident beam, I = transmitted intensity

In the case of hard X-rays (> 1000 eV) the interaction with matter is dominated by the photo-electric effect in which a core-level electron is promoted out of the atom by X-ray photon absorption.[133] The X-ray absorption fine structure (XAFS) displays the modulation of the X-ray absorption probability of the absorbing atom due to its physical and chemical state. Therefore, the intensity of μ is measured as a function of photon energy, near and above the binding energy of a known core-level of a specific atomic species. The X-ray absorption spectrum (XAS) is commonly divided into two regimes. The region closest to the absorption edge has a structure that is sensitive to the local symmetry, coordination chemistry and formal oxidation state of the absorbing atom. This region

is named X-ray absorption near-edge structure (XANES) and extends to approximately 50 eV above the absorption edge. For evaluation of these data multiple scattering events have to be taken into account. On the other hand, the extended X-ray absorption fine structure (EXAFS) refers to the oscillations of the absorption up to 1000 keV above the absorption edge. Due to the higher energy of the ejected photo-electrons single scattering events dominate. Valuable information about the atomic distances, coordination number, and identity of the atoms neighboring the absorbing atom can be yielded from the evaluation of the EXAFS spectra.[133]

The acquisition of XAFS spectra requires an intense and energy-tunable X-ray source, which usually implies the use of synchrotron radiation. With the development and increasing accessibility of high-performance X-ray sources, the investigation of XAFS has become a versatile approach for a wide range of scientific fields, including biology, catalysts research, as well as environmental and material science. It should be underlined that XAFS places only a few constrains on the nature of specimen since it does not require long-range order or crystallinity within the sample and therefore is also applicable to disordered or finite systems and even solutions. It probes the local environment of the absorbing atom and exhibits excellent spatial resolution but at the same time provides ensemble-averaged information. For these reasons XAFS analysis is also highly suitable for characterization of nanostructured systems.[134] Even if measurement conditions and data evaluation are similar to bulk materials, effects of the nanoscaling on the structural parameters (coordination number, inter-atomic distances, and degree of disorder) are to be expected. In addition, indirect information on the material properties (e.g. particle diameter, structural defects) can be derived from the results of fit analysis. Since the sample is characterized as a whole, this method displays a complement to other high–resolution techniques which provide rather detailed information on a very limited number of particles. On the other hand, it should be admitted that an ensemble-averaged method offers only limited information in the case of a non-uniform sample structure or composition. XAFS measurements are element specific and can be performed even at low concentration. Thus, it can be used to investigate the element of minority in a mixed system and to gain information about the local environment of different elemental species within one sample. Various experimental techniques and sample conditions are applicable to XAFS measurements. In particular, it provides the ability to conduct the measurements in situ which means for example at defined pressure or temperature. The measurement can be even performed while (electro-) chemical reactions takes place which offers a powerful tool to directly monitor structural changes of reactants or (electro-) catalytic active materials.

For an isolated atom the absorption coefficient $\mu(E)$ is described by a sharp step at the binding energy of the core-level electron and a smooth function above this edge (see Figure 25). However, in condensed matter the ejected photo-electron interacts with atoms in the direct neighborhood of the absorbing atom. The photo-electron is backscattered from neighboring atoms and interferes with itself. Hence, the constructive and destructive interferences of the outgoing and scattered waves of photo-electrons which depend on the

exact position of neighboring atoms affect the probability of exciting a core electron and by this cause a modulation of the absorption coefficient as a function of photo-electron energy. These modulations which are also displayed in Figure 25 can be isolated by the EXAFS fine-structure function $\chi(E)$.

$$\chi(E) = \frac{\mu(E) - \mu_0(E)}{\Delta\mu_0(E)} \tag{3.11}$$

$\mu(E)$ = measured absorption coefficient, $\mu_0(E)$ = smooth background function representing the absorption of an isolated atom, $\Delta\mu_0(E)$ = change in the atomic absorption at the threshold energy
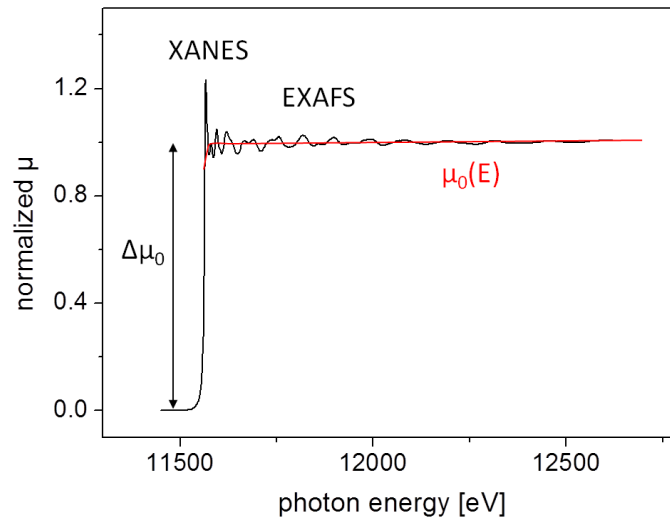
Figure 3.7.: *Normalized XAFS spectra of a Pt foil measured in the energy range of the Pt L_3 absorption edge at the SuperXAS Beamline, SLS. The measured spectra (black), the edge-step $\Delta\mu_0$ and the smooth background function μ_0 (red) which represents the absorption of an isolated atom are displayed. Moreover, the XANES and EXAFS regions of the spectra are denoted.*

Since the wave-behavior of the photo-electron is most important for the evaluation of the EXAFS spectra, the X-ray energy is converted to the wave number of the photo-electron k.

$$k = \sqrt{\frac{2m(E - E_0)}{\hbar^2}} \tag{3.12}$$

m = mass of the electron, E = photon energy, E_0 = threshold energy of the absorption edge, $\hbar$ = reduced Planck constant

The total EXAFS signal is composed from superposition of individual pair-wise contributions from all neighboring atoms. Atoms which are found in similar distances to the

absorbing center can be grouped into a coordination shells. Thus, the different frequencies apparent in the oscillation of the fine-structure correspond to different coordination shells and can be described and modeled by the EXAFS equation:[133,135]

$$\chi(k) = \sum_{j=1}^{shells} A_j(k)\,sin\delta_j(k) \tag{3.13}$$

with the amplitude function

$$A_j(k) = \frac{N_j}{kR_j^2}\,S_0^2\,F_j(k)\,e^{-2k^2\sigma_j^2}\,e^{-2R_j/\lambda(k)} \tag{3.14}$$

and the phase function

$$sin\delta_j(k) = sin\left(2kR_j + \varphi_j(k)\right) \tag{3.15}$$

j = coordination shell index
R = distance between absorbing atom and neighboring atom

N = number of identical atoms in the same coordination shell

σ_j^2 = *relative mean-square disorder of neighbor distance*

$F_j(k)$ = *backscattering amplitude*

$S_0^2(k)$ = *amplitude reduction factor due to many-body effects*

$\varphi_j(k)$ = *total phase shift*

$\lambda(k)$ = *mean free path of the photo-electron*

This expression includes atomic parameters such as $\lambda(k)$, $\varphi(k)$, $S_0^2(k)$ and $F_j(k)$. Moreover, the term $exp(-2R/\lambda(k))$ accounts for the finite lifetime of the excited state. The required set of atomic parameters can be obtained either from theoretical calculations or from experimental determinations by using standard reference compounds. By analyzing the EXAFS signal this equation allows the determination of the structural parameters of the absorbing atoms such as nearest coordination number (N), atomic distance (R) and degree of disorder σ^2. Furthermore, also the atomic species of the neighboring atoms can be identified since the scattering factors depend on the atomic number Z.

The EXAFS contributions from individual coordination shells can be separated by Fourier Transformation (FT) of $\chi(k)$ into the R-space. The FT corresponds to pseudo-radial functions where peak positions are related to inter-atomic distances and the area under the curve can be associated with the number and type of backscatterers.[133] The signal is often weighted with a power of k in order to emphasize the contribution of neighboring atoms with low Z (k-weighting) or high Z (k^3-weighting). The commonly used k^2 weighting of the FT constitutes a compromise between both regimes.[135]

In heterogeneous systems the particle ensemble averaging of the EXAFS results can lead to difficulties in interpretation of the final structure and elemental distribution (e.g. alloying and surface segregation effects, formation of core-shell structures). Here, the Cowley short range order parameter α can be used to describe the homogeneity or heterogeneity of crystalline solids.[136–138] Furthermore, this approach has already been used to investigate the degree of alloying or clustering within bimetallic nanostructures.[139] The short range order parameter α for a bimetallic system is expressed by the following equation whereas the included coordination numbers can be assigned e.g. by evaluation of EXAFS data.

Different situations of homogeneous and heterogeneous packaging of two types of atoms within a 2-dimensional NP are outlined in Figure 3.8. In all cases the lattice provides a 1:1 ratio of both elements. Homogeneous systems where all atoms have similar local environment within each NP are shown in Figure 3.8 (a) and (b). The range of homogeneous configurations is correlated with negative values of α. Moreover, in the case of homogeneous systems one can further distinguish between perfectly ordered (Figure 3.8 (a)) and random configurations (Figure 3.8 (b)). On the other hand, heterogeneous configurations are characterized by positive values of α (see Figure 3.8 (c) and (d)). One example of this configuration where atoms of each type are entirely segregated within different NPs is shown in Figure 3.8 (d).

(a) $\alpha_{AB} = -1$ **(b) $\alpha_{AB} = 0$**   **(c) $\alpha_{AB} > 0$**   **(d) $\alpha_{AB} = 1$**
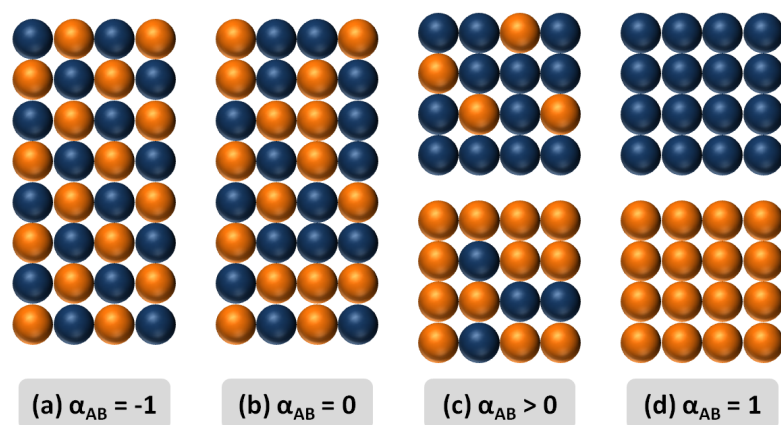
Figure 3.8.: *The Cowley short range parameter α can be used to describes the homogeneity or heterogeneity of crystalline solids. Negative values of α are associated with homogeneous configurations with either ordered (a) or random distribution (b). In contrast, heterogeneous configurations like (c) and (d) are described by positive values of α. They are characterized by the segregation of different kinds of atoms. Graphic was adapted from reference.[139]*

3.4.2. Results and discussion[¶]

Bimetallic NP-based Pt-Pd aerogels are highly promising materials for application in catalysis and their outstanding performance and durability regarding several (bio-) electrocatalytic reactions have already been demonstrated.[90–92,94,95] Moreover, a close relationship between the exceptional structural features of the materials and their electrocatalytic activity is beyond question. As described above, EXAFS probes the atomic environment of a selected element and thereby provides structural and chemical information like homogeneity and spatial distribution of various metal atoms inside the aerogel. Hence, the examination of the structural properties of bimetallic aerogels prepared from monometallic Pt and Pd NPs is in focus of the presented EXAFS investigations. Moreover, influences of a mild thermal treatment on the structure parameters and the alloying behavior of both metals were studied in this work.

Multi-edge EXAFS fits that take into account both the Pt L_3-edge as well as the Pd K-edge, were performed for the Pt_{50}-Pd_{50} aerogel in the pristine state and after a thermal treatment as well as for a Pt_{20}-Pd_{80} specimen. To improve the quality of the fit by reducing the number of independent parameters, a multi-edge fit analysis for the Pt and Pd EXAFS spectra was applied. Moreover, the Pt_{80}-Pd_{20} aerogel was characterized based on the EXAFS data resulting from the energy range of the Pt L_3-edge.
As a representative example, the k^2-weighted Fourier transformed EXAFS data for the Pt L_3-edge and the Pd K-edge of a pristine Pt_{50}-Pd_{50} aerogel sample and the corresponding best fits are displayed in Figure 3.9 (data in black line and fit in red line). The EXAFS spectra and corresponding fits of other samples mentioned in this chapter as well as details on the measurement conditions and data processing can be found in the Experimental Section. The quality of the corresponding fit is demonstrated in both spectra and can be further proven by the R-factor which is as low as 0.013. It is noted, that the R-factor is established by the difference between the real spectra and the resulting fit and should be in the range below 0.020. More details are given in the Experimental Section.
Several intense peaks in the range of 2.0 to 3.0 Å can be observed in both Fourier transformed spectra (Figure 3.9 (a) and (b)). The peaks are related to single scattering events by interaction with the nearest neighboring atoms. Based on the EXAFS equation the fit analyses provide structure parameters of the materials such as partial and total coordination numbers, atomic distances, and disorder parameters. The sets of structure parameters for the first nearest coordination shell of different Pt-Pd aerogel samples obtained for the best fits are summarized in Table 3.4. Even though the elemental composition of the samples was varied over a broad range, the obtained spectra show quite similar behavior and the conclusions based on the EXAFS refinement remain unchanged.
Different kinds of neighboring atoms can be separately quantified by EXAFS analysis. Here, it should be underlined that no reasonable fits for the measured data can be ob-

---

[¶]XAFS measurements were performed in cooperation with C. Laugier Bonnaud (Engineering School Phelma Grenoble INP) and M. Werheid (Physical Chemistry, TU Dresden) under the supervision of M. Özaslan (Electrochemistry Laboratory, headed by T.-J. Schmidt, Paul Scherrer Institut Villigen) and M. Nachtegaal (in situ X-ray Absorption Spectroscopy, Paul-Scherrer Institut). Data evaluation of the EXAFS results was performed by M. Özaslan.
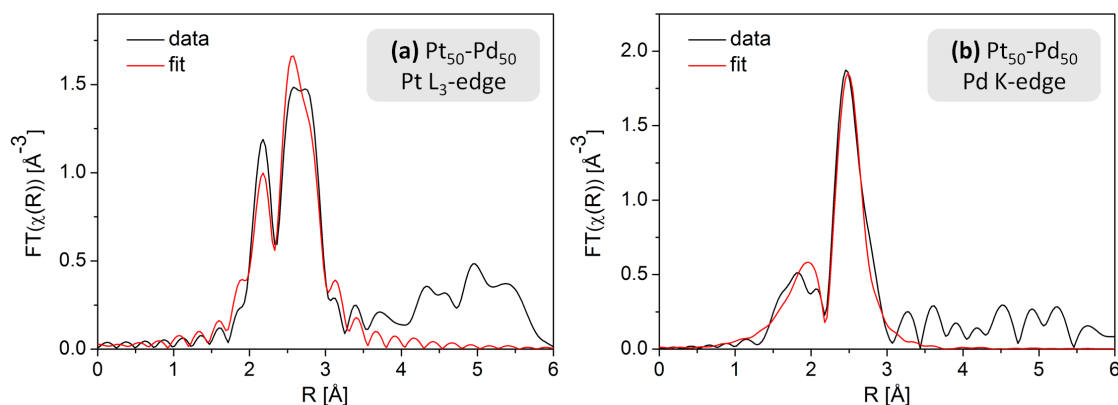
Figure 3.9.: *k^2-weighted Fourier transformed EXAFS spectra of a Pt_{50}-Pd_{50} aerogel sample. Both, the Pt L_3-edge and the Pd K-edge based XAS spectra were concurrently evaluated by using a multi-edge fit analysis. The quality of the fit (red line) is demonstrated in both spectra (black line). The resulting R-factor was as low as 0.013.*

tained when taking into account a Pt-Pd or Pd-Pt coordination. Hence, the partial coordination numbers Pt-Pt and Pd-Pd are equated with the total coordination number of Pt and Pd. Thus, the EXAFS analyses reveal that (almost) no alloy behavior between Pt and Pd within the network structure of the gel was detected. The complete separation of both metal phases can be further expressed by a value of +1 for the short range order parameter α that underlines also the heterogeneity of the structure and of the atomic distribution of both metals. However, the Pd-Pd and Pt-Pt coordination numbers differ strongly from those of the corresponding bulk metals (typically 12 for an fcc crystal lattice) which indicate that the aerogel materials still provide nanoparticular behavior despite the formation of a large-scale and interconnected network. In addition, the total coordination numbers of both metals are quite similar to each other which indicate similar particle sizes. This conclusion is in general accordance with the assumption of separated monometallic domains.

Similar values of the disorder parameter σ^2 of the Pt-Pt bond can be found in all presented samples. The values in the range of about $55 \cdot 10^{-4}$ Å^2 are quite low and therefore signify an ordered structure in the Pt lattice. In contrast to that, the Pd-Pd coordination shows a noticeable higher value of σ^2 and a relatively strong disordering is concluded. This might be related to a disturbed crystal structure due to small crystallite sizes, stress and strain within the crystal lattice or accumulation of stacking faults and grain boundaries.

The atomic distances in the fcc lattices of the corresponding bulk metals Pt and Pd are in the range of 2.774 Å and 2.751 Å, respectively.[140] An decrease of the Pt-Pt atomic distances that might be related to compressive lattice strains caused by a large surface tension, has been described in the literature for nanometer sized Pt aggregates and clusters.[141] However, for particles in the size range above 4 nm, almost bulk-like behavior regarding the Pt-Pt atomic distances is expected. Also in the case of the evaluated Pt-Pd aerogels the Pt-Pt atomic distance is almost equal compared to the bulk metal. On the

Table 3.4.: *Summary of the structure parameters from several Pt-Pd aerogels as determined by EXAFS refinement. The first nearest neighbor coordination numbers N, the first nearest atomic distances R and the first nearest disorder parameter σ^2 are given for different Pt-Pd aerogel samples, respectively. No Pt-Pd or Pd-Pt coordination was revealed by the results of the fit analysis and therefore separated Pt and Pd domains within the nanostructured materials are assumed.*

aerogel	N Pt-Pt	N Pd-Pd	R [Å] Pt-Pt	R [Å] Pd-Pd	σ^2 [10^{-4} Å^2] Pt-Pt	σ^2 [10^{-4} Å^2] Pd-Pd
Pt$_{50}$-Pd$_{50}$	10.5 ± 1.9	10.1 ± 1.2	2.76 ± 0.05	2.76 ± 0.01	57 ± 7	97 ± 8
Pt$_{50}$-Pd$_{50}$ 150 °C, 30 min	9.0 ± 0.8	8.5 ± 0.9	2.76 ± 0.05	2.77 ± 0.01	55 ± 4	83 ± 8
Pt$_{20}$-Pd$_{80}$	9.4 ± 1.2	9.2 ± 0.8	2.76 ± 0.05	2.79 ± 0.03	53 ± 6	89 ± 7
Pt$_{80}$-Pd$_{20}$	9.2 ± 0.6	—	2.76 ± 0.05	—	55 ± 3	—

other hand, a contrary lattice expansion is observed in the case of the Pd-Pd bond. Even though this phenomenon has been described in the literature for several times the reason is still unrevealed. Possible explanations include structural changes, pseudo-morphism, incorporation of impurities, as well as enhanced surface disorder.[142] However, this effect is discussed controversially in the literature and in the case of Pt-Pd aerogels no reliable explanation can be given on the basis of the available data.

Furthermore, structural changes due to thermal treatment could be monitored by means of EXAFS analysis. Therefore, a mild thermal treatment of the Pt$_{50}$-Pd$_{50}$ aerogel sample was performed for 30 minutes at 150 °C under inert atmosphere. This annealing step aimed to the enhancement of atom diffusion and might promote the fusion of both metals in particular at the interparticle interfaces. However, the corresponding fit analysis reveals that the thermally treated aerogel structure still exhibits separated domains of Pd and Pt since no Pt-Pd coordination was observed in the EXAFS spectra. Moreover, also the structural parameters remain quite unchanged compared to the corresponding pristine sample.

In conclusion, the EXAFS analysis gives valuable information on the number and kind of atoms neighboring the absorbing atom, but also on the atomic distances and the degree of disordering within the nearest coordination shell. Based on the EXAFS analysis it has to be stated, that almost no alloy formation or mixing of Pt and Pd atoms occurred during the formation of the gel network. This might imply the preservation of the initial monometallic building blocks within the nanowires. Even a mild thermal treatment did

not sufficiently promote the formation of an alloyed Pt-Pd structure. Nevertheless, it should be taken into account that EXAFS is an averaging method which might not display partially alloyed domains at the interparticle interfaces of the NPs which are attached to each other during the gel formation. Therefore the findings from EXAFS analysis need to be complemented by the results gained from other characterization methods.

3.5. Analytical and scanning transmission electron microscopy

3.5.1. Background

Although enlightening results were gained from phase analysis and investigation of local atomic environment by means of powder XRD and EXAFS, one has to admit that these techniques suffer from a lack of spatial information and the ensemble-averaging of results over the whole investigated specimen. Complex, heterogeneous structures which provide a combination of different structural regimes and contain minority phases with low proportion are not sufficiently characterized by these approaches. Since the investigated bimetallic aerogels are formed by attachment and possible fusion and merging of separated monometallic spherical building blocks also quite heterogeneous structures could be expected. For example, even in the case of separated phases of both metals in a bimetallic aerogel, atom diffusion and alloy formation might be observed at the boundaries and contact points of the fused initial NPs. In addition, up to now only little or indirect information was gained regarding the clustering and random or ordered assembly of the initial metallic building blocks along the nanochains. In order to throw some light on these open issues several bimetallic aerogel structures were investigated by analytical TEM which provides chemical analysis with high lateral resolution. Thereby, even a quantitative mapping of the elemental distribution can be achieved.

Analytical TEM is a term which describes the collection of spectroscopic data in TEM by following the inelastic interaction of the incident electron beam with the specimen. By this approach the quantification of the concentration of elements in a certain area, the mapping of their distribution with high spatial resolution, and even the determination of their chemical state can be performed.[143] Electrons are a kind of ionizing radiation and a great variety of secondary signals arise from the specimen due to interaction with electrons. The signals which are generated when a high-energy beam of electrons interacts with a thin sample are summarized in Figure 3.10. The most common techniques in analytical TEM are energy-dispersive X ray spectroscopy (EDX) and electron energy-loss spectroscopy (EELS) and the corresponding signals are highlighted in the scheme.

To determine the content of a particular element in the investigated sample the characteristic quantized energy levels and the associated electronic states of the atoms can be used. Under the impact of an incident electron, the tightly bound, inner-shell electrons of the atom may be excited either to a free electron state or to an unoccupied energy level with higher energy. The excited system will subsequently decay with the core hole being refilled and this will release energy in the form of an X-ray photon or an electron.[133] The energy of the X-rays, typically in the range of few hundred eV to 20-40 keV, depends on
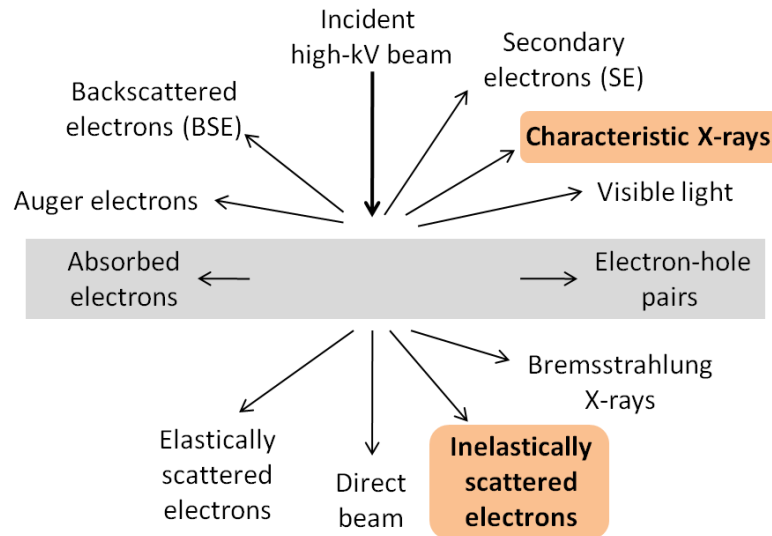
Figure 3.10.: *Signals generated when a high-energy beam of electrons interacts with a thin sample. Those signals which are commonly used in analytical TEM are highlighted. Characteristic X-rays emitted from the sample are detected in EDX techniques whereas inelastically scattered electrons are evaluated by EELS and used for image formation in the EFTEM approach. Graphic adapted from reference.[144]*

the characteristic energy levels of the bound electrons which makes it possible to identify the atomic number of the elements that have been involved in the excitation process.[143] Due to this, the chemical composition can be analyzed from EDX results by investigating the energy-distribution of the emitted characteristic X-rays photons.

Contrary to EFTEM, the EDX approach requires the localization of the exciting electron beam to not only gain a quantitative elemental analysis but rather complement these data with spatial resolution. In order to achieve a nanoscaled excitation area a very small electron beam, termed probe, is applied which has a typical diameter of less than 0.1 nm and can be scanned over the sample in a raster pattern.[145] This combination of TEM and SEM technology creates a scanning transmission electron microscope (STEM) which provides both the basic of analytical TEM and a unique scanning-imaging tool.[144] Setups which exclusively or primarily operate in the STEM mode are named as dedicated STEM and besides the detectors for chemical analysis they are typically equipped with a set of different imaging detectors. Due to the geometry of these detectors the transmitted electrons are classified by their scattering angle as it is depicted in Figure 3.11.

Contrast in TEM images arise due to the scattering of the incident beam by the specimen. In this process, the electron wave can change both its amplitude and its phase which leads to the fundamental distinction between amplitude and phase contrast. In the case of amplitude contrast there are two types, namely, mass-thickness contrast and diffraction contrast.[144] Mass-thickness contrast arise from incoherent elastic scattering of electrons (Rutherford scattering). In crystalline materials also a coherent scattering may occur in
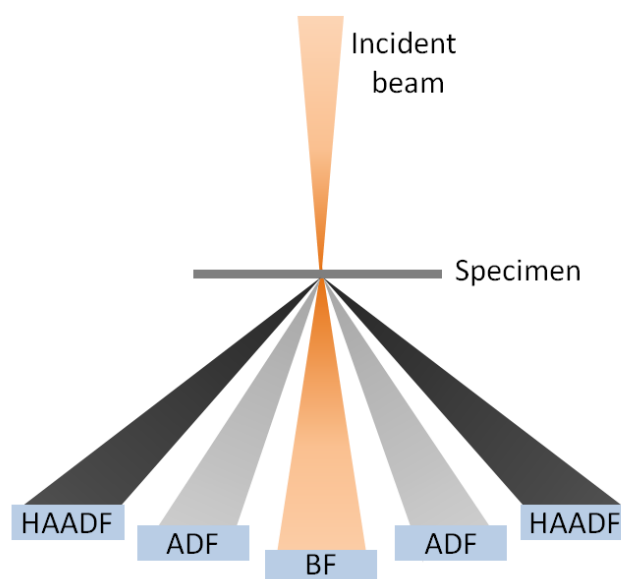
Figure 3.11.: *Configuration of detectors commonly used in STEM. Different ranges of electron scattering angles are gathered by the detectors, respectively. Off axis angles are: BF < 10 mrads, ADF 10-50 mrads, HAADF > 50 mrads. Graphic adapted from reference.*[144]

case of Bragg conditions are fulfilled which leads to diffraction contrast. Since the diffraction depends on orientation of the sample the diffraction contrast changes when the sample is tilted. In STEM a detector which collects over a disc of scattering angles centered on the optical axis of the microscope is used to perform bright-field (BF) images, whereas the annular dark field (ADF) detector collects over an annulus at higher angle where only scattered electrons are detected.[143] Electrons scattered out to even higher angles forming a so-called high angle annular dark field (HAADF) image in which Rutherford-scattering effects are maximized and diffraction contrast effects are smoothed out. Bragg effects are avoided if the HAADF detector only gathers electrons scattered through an angle of > 50 mrads.[144] As the scattering angle increases, the scattered intensity from an atom approaches the Z^2 dependence (Z= atomic number) that would be expected for Rutherford scattering from an unscreened Coulomb potential. Due to the screening effect of the atom core electrons this limit is not reached in practice, and the Z exponent falls to values typically around 1.7.[143] Therefore the contrast in HAADF images shows a strong sensitivity to the atomic number which allows heavy elements to show up brighter in the image. Nevertheless, the contrast in HAADF images still depends linearly on the sample thickness.

EDX and EELS can be used in parallel with ADF and HAADF to gain information about the chemical composition of the sample simultaneously with the structural and morphological information. Nevertheless, it should be noted, that EDX is most suitable for quantification of heavy elements like the noble metals investigated in the present nanostructures. For that reason, the results presented here are limited to STEM EDX technique for

the analysis of the elemental distribution of multimetallic aerogels. The main advantage of EDX analysis in STEM compared to SEM is the improvement of spatial resolution. Due to the increasing accelerating voltage and the thinner sample the interaction volume strongly decreases but still beam broadening effects are significant for EDX in STEM.[143] The EDX spectra gained by scanning the sample are transformed into quantitative maps of elemental distribution. Due to the high lateral resolution and the reliable determination between the different noble metals on the basis of their characteristic X-ray photon energies the STEM EDX technique is highly suitable for the investigation of the elemental distribution within the nanochains of bimetallic aerogels.

HAADF imaging and STEM EDX are widely used for the characterization of metal NPs and nanostructures as described in the literature. The techniques were applied for detection of heavy element NPs in environmental samples,[146] analysis of AuPd nanostructures and correlation between the Au:Pd ratio on the particle surface and synergistic effects for catalytic activity,[147] and characterization of noble metal alloyed nanostructures and tailoring of elemental composition in order to tune their catalytic activity[148] to name only some examples. For the characterization of semiconductor NP-based aerogels by HAADF imaging and STEM EDX so far only one example has been described by KO- RALA and coworkers.[72] Furthermore, first results regarding HAADF STEM and STEM EDX analysis of an Au-Ag NP-based aerogel structure were presented in a former work of the author[20] but extended calculations, optimization of measurement conditions and investigation of further elemental combinations are necessary to gain reliable and comprehensive conclusions on the respective elemental distribution.

3.5.2. Results from STEM and STEM EDX[‖]

In order to perform STEM imaging and elemental mapping by STEM EDX analysis a Titan^3 G2 60-300 microscope equipped with a ChemiSTEM EDX system based on a 4 windowless silicon drift detector was used, which provides enhanced acquisition efficiency and speed. Therefore, it offers measurements at low dose, high spatial resolution and fast chemical mapping. In addition, the acceleration voltage of the field emission gun can be tuned from 60 to 300 keV. Three different bimetallic aerogel structures (Au-Ag, Au-Pd and Pt-Pd) were chosen for evaluation and besides chemical analysis by STEM EDX also STEM imaging was performed. STEM images of an Au-Ag aerogel specimen that were acquired in parallel by the use of the BF, ADF, and HAADF detector are shown in Figure 3.12, respectively. The comparison of these images underlines the different material properties that are highlighted with the different detector configurations.

In the BF image (Figure 3.12 (a)) both the mass-thickness contrast and the diffraction contrast are contributing and the typical nanochain morphology of the Au-Ag gel structures prepared by the temperature-controlled two-step approach is obvious. The initial NPs are strongly merged and formed a network of nanochains with varying diameter. The polycrystalline nature of the nanostructure is clearly exhibited in the ADF image (Figure 3.12 (b)). The scattering of electrons to the angles gathered by this detector is mainly caused by diffraction effects. Therefore, the diffraction contrast between crystallites with various orientations and the variety of grain boundaries within the material are obvious in the ADF image. Moreover, contrast may arise from crystal defects as for example local lattice torsions, stacking faults, or twinning effects. It is apparent, that the HAADF image (Figure 3.12 (c)) strongly differs from the ADF image since the diffraction contrast is smoothed out and instead the Z-contrast becomes dominant. Bright domains that are much smaller than the initial NPs are distributed irregularly along the nanochains. Although the heavier element Au should appear brighter in the HAADF image, the contrast also depends on the sample thickness and therefore is influenced by the three-dimensional structure of the aerogel network, the varying diameter of nanochains and the possible overlaying of several nanowire fragments. One example of the latter can be clearly seen in the bright part located in the top left corner of the image. Hence, based on the contrast in the HAADF image it is not possible to clearly distinguish between the variation of the sample thickness and the distribution of lighter and heavier elements. Nevertheless, the HAADF STEM images exclude the connection of the initial noble metal NPs via organic linker molecules. Instead, continuous nanochains are formed by the strong coalescence of the spherical building blocks.
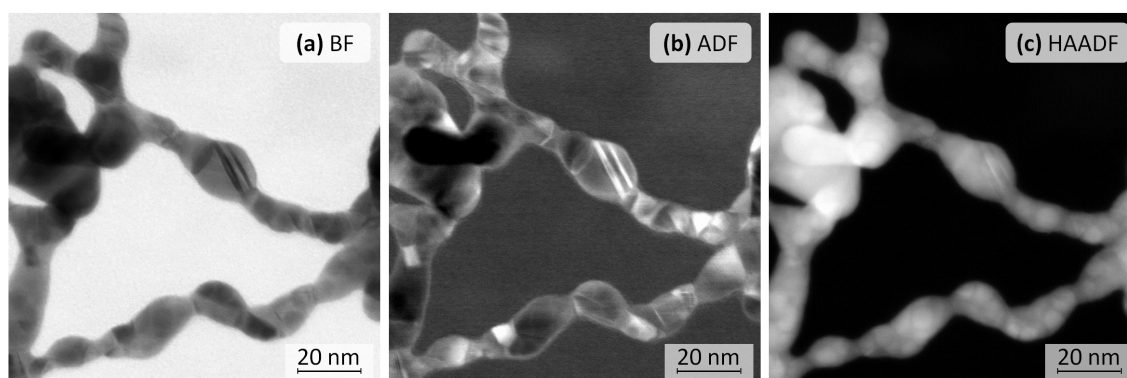
Figure 3.12.: *STEM images of the same area of an Au-Ag aerogel specimen that were acquired by the use of the BF, ADF and HAADF detector, respectively. The polycrystalline nature of the nanostructure is obvious from the ADF image whereas in the HAADF image it is not possible to clearly distinguish between contrast arising from sample thickness and such being attributed to the distribution of lighter and heavier elements.*

It shall be underlined that the enhanced acquisition efficiency and speed of the EDX detector system is highly suitable to ensure a low dose for the sample. This is crucial in order to minimize or even prevent damages of the structure morphology or changes of

the elemental distribution within the sample during the acquisition of EDX spectra and the mapping process. These changes might be caused by enhanced alloy formation or stimulation of segregation effects due to the interaction with the electron beam. Therefore, the measurement conditions had to be optimized and the acceleration voltage of the field emission gun was lowered to 60 kV. This approach ensures the decrease of the radiation dose even at higher currents that are required for the acquisition of EDX spectra with evaluable count rates at a reasonable time scale. At the same time a decrease of the acceleration voltage is accompanied with a broadening of the probe diameter. It has to be admitted that an increase of the probe diameter on the one hand decreases the resolution of the measurement but on the other hand further contributes to reduce the local stress for the affected specimen caused by the electron beam.

Considerable changes of the nanowire morphology and the elemental distribution due to the interaction with the electron beam were observed in the case of an Au-Ag aerogel sample. The alteration of the specimen is obvious by comparison of the HAADF images right before and after the STEM EDX elemental mapping which are shown in Figure 3.13 (a) and (b). Though the nanochains remain intact in general, their morphology drastically changed since additional blurred domains are formed at the outside of the nanowires. In the overlay of the HAADF image with the elemental maps of Au and Ag (Figure 3.13 (c)) it becomes obvious that these blurred domains are composed from Ag atoms which give rise to the conclusion that Ag segregation to the outer shell of the nanochains is induced by the interaction with the accelerated electrons of the probe. In order to avoid this kind of sample damage the beam current was significantly reduced during the further investigations.
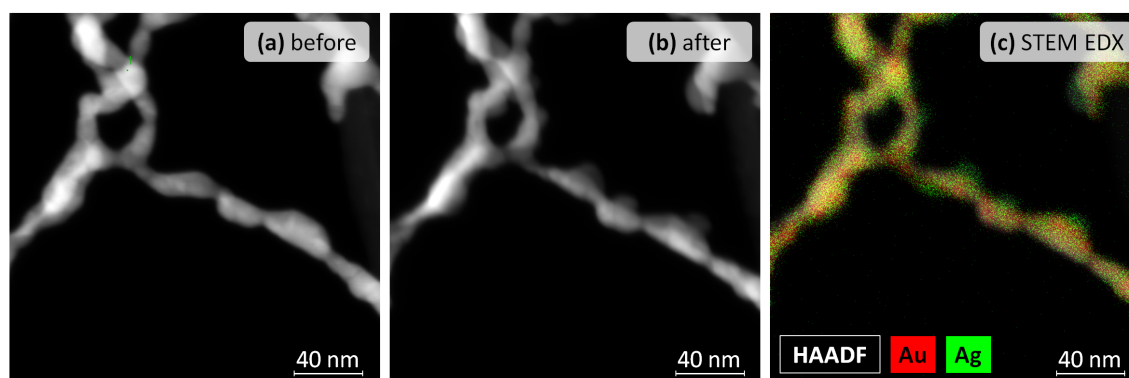
Figure 3.13.: *Comparison of the HAADF images of the same sample area before (a) and after (b) STEM EDX mapping reveals obvious changes. The blurred areas formed are attributed to segregation of Ag as concluded from the elemental mapping (c). Hence, the applied measurement conditions lead to considerable changes of the sample structure. Therefore, further measurements were performed with lower beam current in order to avoid damage of the sample.*

Valuable information can be obtained from the localized chemical nanoanalysis offered by high resolution STEM EDX elemental mapping. Several bimetallic aerogel structures were investigated and compared. The overall atomic ratio of the combined metals was ad-

justed to 50:50 as evidenced by SEM EDX analysis which averages the elemental composition over a sample area of several micrometers. For illustration of the bimetallic nanostructures a STEM image of a representative specimen section is combined with single element mappings and an overlay of the elemental distributions, respectively. Moreover, the quantitative elemental composition of several selected small areas that are marked in the overlay image are summarized in the corresponding tables.

	Au (at%)	Ag (at%)
1	37.2	62.8
2	43.8	56.2
3	43.5	56.5
4	16.5	83.5
5	55.7	42.9
6	18.7	81.3
7	39.1	60.9
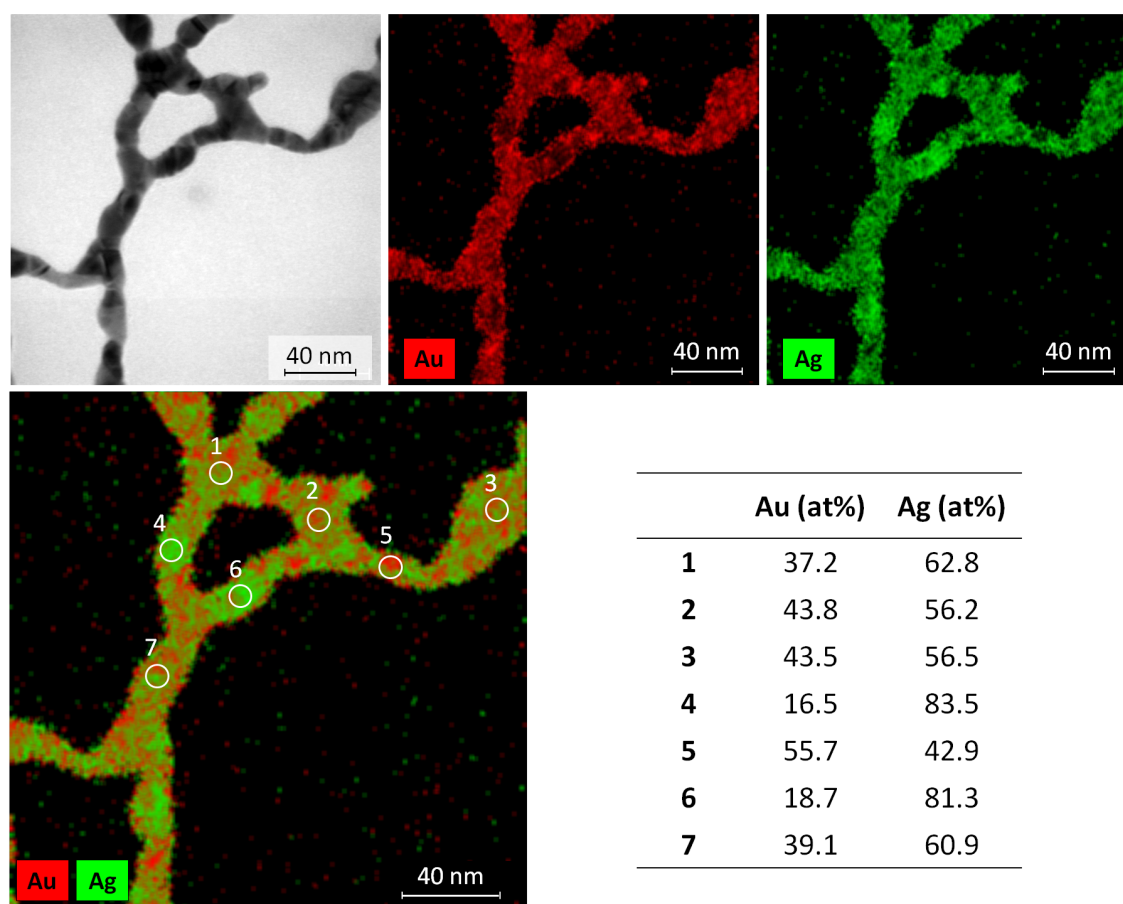
Figure 3.14.: *BF image, Au map, Ag map and Au-Ag overlaid map as resulting from the STEM EDX analysis of an Au-Ag aerogel sample. The elemental compositions of several selected areas (d ≈ 9 nm) marked in the combined mapping are summarized in the corresponding table. Even though monometallic building blocks were used to grow the nanochains an almost completely alloyed Au and Ag nanostructure is found in the final aerogel. However, the elemental distribution is not completely homogenous and some Au-rich and Ag-rich areas were observed.*

The elemental mappings of an Au-Ag aerogel specimen that are shown in Figure 3.14 reveal an almost complete alloy formation of both noble metals within the nanochains. However, the elemental distribution is not entirely homogeneous and some Au-rich and Ag-rich areas can be observed in the map. For instance an elevated silver content in the marked areas 4 and 6 is proven by the quantitative compositions given in the table. Nevertheless, both metals were detected along the complete nanochains and there are several

examples of analyzed areas where the elemental ratio of close to 50:50 that character-izes the entire material is observed on the nanometer scale (see e.g. points 2, 3 and 5). Keeping in mind the starting point of separated monometallic NPs, these results signify a strong atom interdiffusion and alloying process of Au and Ag. It shall be underlined that no monometallic domains in the size of the initial NPs were preserved during the gel formation.

	Au (at%)	Pd (at%)
1	2.9	94.5
2	88.6	11.3
3	62.4	35.2
4	76.1	21.9
5	1.4	97.8
6	67.5	30.3
7	70.2	27.7
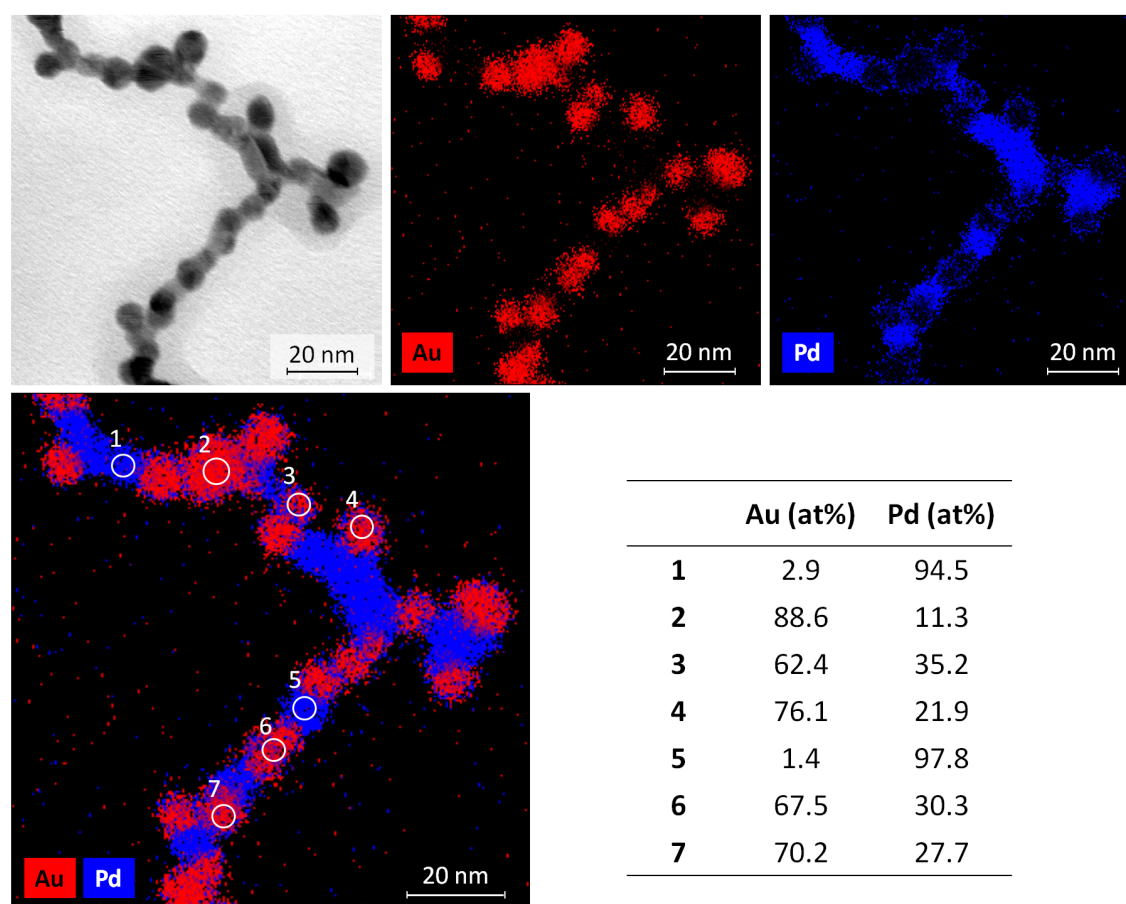
Figure 3.15.: *Results of the STEM EDX analysis of an Au-Pd aerogel. STEM BF image, single element mappings of the related metals, and an Au-Pd overlaid elemental distribution mapping are provided. In addition, the elemental compositions of selected areas (d ≈ 4.5 nm) are summarized in the table. The structure is characterized by separated domains in the size range of the initial NPs. Pd seems to be the more mobile species since it is found everywhere along the nanowires. Nevertheless, based on these data no clear distinction between the interdiffusion of Pd atoms into the Au lattice and the formation of a core-shell configuration along the nanowires can be established.*

A significantly different structure is identified in the case of an Au-Pd aerogel specimen as it is obvious from the corresponding elemental mappings displayed in Figure 3.15. Here, separated areas in the size range of the initial NPs which contain mainly one of the metals seem to be preserved within the nanochains even after fusion of the particles

and formation of the network structure. The distribution of Pd is especially remarkable since it is not only located in Pd clusters but also seems to enclose the Au domains with a thin Pd layer. Whereas almost pure Pd clusters are observed (see e.g. point 1 and 5), the gold-rich areas (e.g. point 2 and 4) still contain a certain amount of Pd which supports the assumption of a higher mobility of Pd atoms within the nanostructure. Moreover, several areas which are composed of both kinds of metals are evidenced by the STEM EDX measurements. However, when evaluating these results one should take into account that the penetration depth of the electron beam is larger than the diameter of the nanochains. Hence, in the case of sample areas where both metals were detected no clear distinction between a core-shell configuration and an alloyed structure formed by interdiffusion of the Pd atoms into the Au lattice can be made from these results.

	Pt (at%)	Pd (at%)
1	0.5	98.3
2	10.5	86.9
3	59.2	39.6
4	26.8	72.0
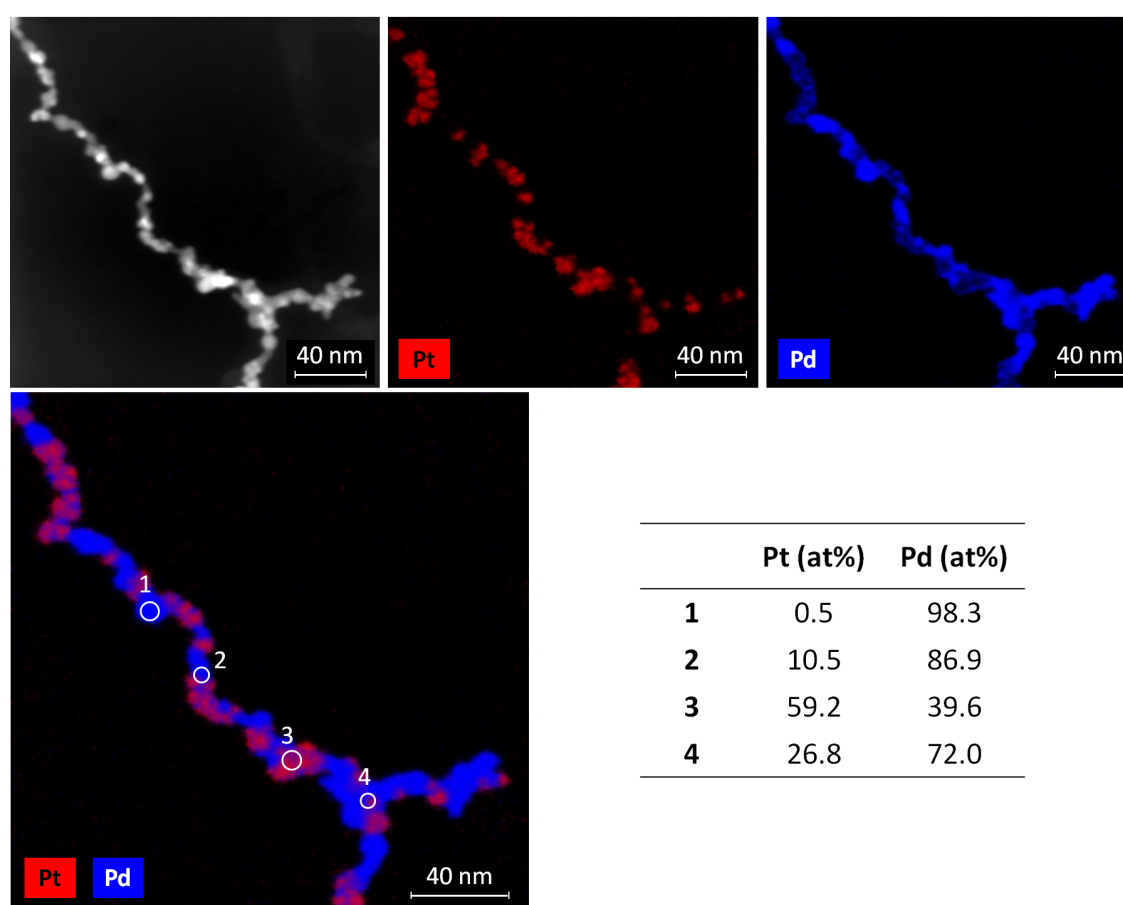
Figure 3.16.: *HAADF image and STEM EDX elemental mappings for the characterization of a Pt-Pd aerogel structure. The quantitative elemental compositions of the numbered areas (d ≈ 6 nm / 7.5 nm) are displayed in the table. While Pd is distributed over the whole nanochains and even pure Pd domains were detected, Pt is only found in separated domains. However, the question of interdiffusion and alloy formation in the areas where both metals were detected cannot be finally answered by these investigations.*

As a third example, the elemental distribution of a Pt-Pd sample was investigated. The results of the STEM EDX analysis and the related HAADF image that are displayed in Figure 3.16 reveal the special properties of the obtained structure. On the one hand Pd is detected in all areas along the investigated nanostructure and it is forming continuous nanochains which seem to provide the backbone of the network. Pure Pd domains were detected as for example shown in point 1. Thus, no complete alloying and interdiffusion of both metals occurred during the joint gel formation. On the other hand separated clusters of Pt are incorporated within the network. Even though in some of the investigated spots both metals were detected (e.g. point 3 and 4) it is not clear whether interdiffusion and alloying of the metals occurred in these areas or whether for example Pt particles are attached to the surface of a Pd wire without intermixing of both metals. It is even possible that Pd forms a shell structure that encloses the Pt domains similar to the structure observed in the Au-Pd sample. This question cannot be finally clarified since also in this case the penetration depth of the electron beam is larger than the diameter of nanochains. Moreover, it shall be noted that the contrast of the related HAADF image is not suitable for estimation of the elemental distribution since the Z-contrast of the image is additionally influenced by the variation of the nanochain diameter. The sample thickness is increase in several areas of the structure where the initial NPs seem to be aggregated and these domains appear brighter in the HAADF image. Thus, the bright areas do not necessarily correlate to the distribution of the heavier element Pt as it is proven by EDX analysis for example in point 1.

In summary, strong differences regarding the alloying behavior and spatial elemental distribution within the gel networks were observed for different combinations of noble metal NPs. Whereas Au and Ag tend to form a completely alloyed structure, Au and Pd are distributed in separated areas in size of the initial NPs while Pd is forming a shell structure that encircles the Au domains. Moreover, in the case of Pd-Pt aerogels a continuous network of Pd nanochains is formed while separated domains of Pt are observed. Nevertheless, further investigations are needed to describe the structure in more detail and compare the resulting structures of different preparation methods. Moreover, the influence of thermal treatments or reactive gases on the metal distribution within the nanochains might be monitored by this approach. Further, the metal distribution in the nanostructures observed at the early stages of the gel formation could be investigated in order to monitor the diffusion process of metal atoms and the merging of particles e.g. in the Au-Ag system.

3.6. Conclusion and Discussion

In order to gain a detailed knowledge of the structural properties and features of bimetallic aerogel structures a manifold set of characterization techniques was utilized. Thereby, the characteristics of the materials were investigated with regard to various issues. NP-based aerogels provide unique properties since they represent macroscopic materials with structuring on the nanometer scale. Therefore, on the one hand the properties of the overall assembly need to be determined. In particular, the inner surface area, the pore size

distribution and the porosity of the three-dimensional network structure are in focus of the investigations. For the investigated metallic aerogels inner surface areas in the range of 45 - 90 m^2/g were quantified by BET analysis of the N_2-physisorption experiments. It shall be underlined that these are notably high values hardly reach by other techniques that are established for preparation of porous noble metals. The adsorption isotherms provide mainly type II behavior and no prevalent pore size was observed. Furthermore, the dominance of large mesopores and macropores within the material was concluded from the shape of the adsorption isotherms, as well as from the total pore volume that was calculated based on the monolith density. The exceptional properties of metallic aerogels that arise from the self-supporting three-dimensional network of nanochains are also expressed by the relative densities in the range of 0.1 to 0.4 % and the corresponding porosities of 99.9 to 99.6 %. Due to their extremely low density, high inner surface area and the accessibility and interconnection of pores in the size range of meso- and macropores, metallic aerogel are highly promising materials for their use in catalysis or sensor technology. Moreover, a high porosity, a broad pore size distribution and a network of open pores and tunnels were also observed in the SEM analysis of metallic aerogels which is in good accordance to the quantitative results of the physisorption experiments.

Specific thermal treatment was applied to investigate both the thermal stability of the materials and the possibility to tune the ligament diameters and pore sizes of the network. Several bimetallic aerogel samples were annealed under various conditions in the temperature range of 150 to 400 °C. Thereby, Au-Pd and Pt-Pd samples were characterized by a high thermal stability even at 300 °C under inert atmosphere. As evidenced from SEM and TEM images the highly porous structure of the materials is preserved whereas the diameter of nanochains only slightly increased. However, after annealing of the Au-Pd aerogel sample for 12 hours at 400 °C an inhomogeneous structure with partially increased diameter of ligaments was observed. In contrast, the nanochain diameter of Au-Ag aerogels can be tuned easily by thermal treatment. It shall be underlined that even though the material is much more sensitive to elevated temperatures and the diameter of nanowires increased, still a network of nanowires was preserved and no degradation to a compact and nonporous structure occurred.

Besides the investigation and modification of the assembly properties on the other hand versatile characterization techniques were applied that aim to the enlightenment of the elemental distribution, phase composition and local atomic structure within the nanochains that form the gel network. Within the scope of this chapter powder XRD and corresponding structure modeling, EXAFS analysis, HAADF STEM and STEM EDX high resolution elemental mapping were discussed in more detail. In addition, the evaluation of lattice parameters by HRTEM and imaging of the elemental distribution via SEM EDX have already been shown in our former publications.[20,84] These different approaches provide complementary data and findings which result in a coherent overall picture. It shall be highlighted that the conclusions gained by the different characterization techniques are consistent and by no means contradictory to each other.

Phase analysis of the bimetallic nanostructures is challenging due to the isotypy and the similar lattice parameters of the investigated noble metals. Moreover, the measurements suffer from reflection broadening that is caused by the small crystallite size and possible lattice strains within the multicrystalline nanowires. For these reasons no distinction between monometallic and alloyed phases was realized by this approach in the case of Pt-Pd and Au-Ag aerogel samples. In contrast, separated phases for each involved metal were verified from the XRD pattern of an Ag-Pd and an Au-Pd aerogel specimen, respectively. The latter was chosen for further investigating the enhancement of the interdiffusion and alloying process by thermal treatment of the material. Indeed, thermal-induced phase modifications were realized by this approach and the gradual alloying is determined by the stepwise change of the diffraction pattern. After annealing at 300 °C for 30 minutes two partially mixed phases – a Au-rich and a Pd-rich one – were assumed from the results of the structure model calculations since the lattice parameter of Au increased due to incorporation of Pd atoms into the Au lattice and vice versa in the case of Pd. After annealing of the solid aerogel for 12 hours at 400 °C even a complete alloy formation of Au and Pd was observed as established by a single mixed phase in the XRD pattern. At the same time the crystallite sizes increased from 3 nm in the pristine sample to 5 nm after short annealing at 300 °C and further to 15 nm after entire alloy formation at 400 °C. Furthermore, the results of the annealed Au-Pd samples are in accordance with the observation from SEM and TEM regarding structural changes under same conditions as discussed above. It seems reasonable that the atom diffusion which enables alloy formation is also accompanied by reorganization of structure and by increase of crystallite sizes and nanochain diameters.

In addition to the diffraction measurements that could not provide significant information on the phase composition of Pt-Pd aerogels, alternative characterization techniques were used. For example EXAFS analyses were performed in order to investigate the homogeneity, coordination numbers, and atomic environments within the Pt-Pd nanostructures. The results of the EXAFS multi-edge fit analyses suggest that Pt is not coordinated by Pd atoms and vice versa. Therefore, separated domains of Pt and Pd within the structure are concluded. The value +1 of the short range order parameter α further expresses the heterogeneity of the structure. However, the total coordination numbers of Pt and Pd atoms are much smaller than in the corresponding bulk metals which indicate the preservation of the nanoparticular behavior even after formation of an interconnected network. Moreover, the quite similar coordination numbers of both metals also indicate similar particle sizes. It shall be noted, that the degree of disorder is remarkably higher in the case of the Pd-Pd bond as compared to the Pt-Pt environment which gives a hint on a disturbed Pd crystal lattice caused by small crystallite sizes, grain boundaries or stacking faults. Similar results of the EXAFS analysis were gained for different samples even though a broad elemental composition range was covered. In this respect again, the influence of thermal treatment on the elemental distribution and interdiffusion of metals was part of the investigations. After a mild thermal annealing at 150 °C for 30 minutes still no mixed Pt-Pd coordination numbers could be derived from the fit analysis. However, also in this case the results regarding the absence of an interdiffusion processes due to the thermal

treatment are in correlation with the observations of SEM and TEM which give no hint on distinct changes of the structure morphology under the given conditions.

In order to provide a counterpart to the ensemble-averaged results of XRD and EXAFS analyses STEM EDX high resolution elemental mapping was performed. This kind of analytical TEM approach provides chemical analysis with high lateral resolution and is highly applicable for the quantitative analysis of the distribution of the different metals within the nanochains of the gel network. Several bimetallic aerogels were investigated and strong differences regarding the interdiffusion and mixing of the initial monometallic building blocks were observed. However, the high penetration depth of the electron beam complicated the interpretation of the data. Hence, for evaluation of the structure, the results of STEM EDX need to be complemented and combined with the findings from XRD and EXAFS analyses. The elemental mapping of an Au-Pd sample displays separated areas of both metals in the size range of the initial NPs. Thereby, a particular distribution of Pd was observed since it is not only located in monometallic Pd clusters but also seems to enclose the Au domains with a thin Pd shell. No alloy formation of both metals is assumed, taking into account the results of the corresponding XRD refinement which show separated phases of Au and Pd. In the STEM EDX analysis of the Pt-Pd aerogel Pt is found in separated domains and agglomerates, whereas Pd provides continuous nanochains. This is in good accordance to the results from EXAFS analysis that reveal heterogeneity of the structure and absence of Pt-Pd or Pd-Pt coordination. Moreover, the higher mobility of the Pd within the structure may correspond to the higher degree of disorder evaluated from the EXAFS fit analysis. In contrast, the low degree of disorder in the Pt-Pt bond may give a hint on the retaining of the initial NP building blocks as well as on a low tendency of atom diffusion in the case of Pt. Hence, also for the Pt-Pd aerogel structure the findings from EXAFS analyses and the results of STEM EDX elemental mapping confirm and complement each other.

From the elemental mapping it becomes obvious that the Au-Ag system represents a special case since an almost complete interdiffusion and alloy formation of both metals within the pristine Au-Ag aerogel structure is suggested due to the STEM EDX results. Au and Ag are fully mixable in the solid bulk phase at all relative concentrations of the two species and homogeneous AuAg alloys are stated to be more stable than either pure Au or Ag thermodynamically.[149,150] The interdiffusion process is strongly enhanced due to the very similar lattice parameters, atomic radii and electronegativities of both metals. In general, the diffusion of metals in nanosized systems is strongly accelerated compared to the bulk materials and can be even stronger promoted due to grain boundaries and lattice defects. It shall be stated that the spontaneous alloying of Au-Ag nanostructures has already been described in the literature.[151,152] Moreover, the lower melting points of Au and Ag accompanied by a strong atom diffusion probability may also explain the sensitivity to thermal treatment and the tunability of the nanochain diameters in the case of Au-Ag aerogels.

Furthermore, STEM imaging with various detectors that gather different scattering angles of the transmitted electrons was performed. Thereby, the variety of grain boundaries along the nanochains was confirmed by ADF STEM images whereas the strong variation

of the sample thickness prevents reliable conclusions concerning the elemental distribution from the Z-contrast of the HAADF STEM images.

Finally, it should be noted that these results are also in correlation with the impressions gained from TEM images of bimetallic aerogels described in Chapter 2.1. The high mobility and diffusion rate of atoms which is needed to facilitate the formation of an alloy in the Au-Ag system also favors the strong welding of NPs and the smoothing of the surface of the nanochains. In contrast lower diffusion rates in the Au-Pd nanostructures are accompanied by "knobbly" nanochain surfaces since smoothing is hindered or at least decelerated. Moreover, the irregular shape of nanochains observed in Pt-Pd aerogels may also be attributed to the clustering of Pt fragments.

The results presented in this chapter display a useful overview on suitable characterization techniques and provide detailed insights into the structural properties of NP-based (multi-) metallic aerogels. However, further investigation that might be supported by theoretical calculations are needed to complete the characterization of the structures and to understand the fusion and merging of monometallic NPs that takes place during the gel formation in more detail.

Chapter 4.

Processability and thermoelectric properties of metallic aerogels

NP-based aerogels are macroscopic materials with structuring on the nanometer scale which carry exceptional properties. At the same time various preparation pathways and modifications leading to a broad range of NP-based aerogel compositions have been established. For these reasons the related list of promising application fields is remarkably wide-ranging: heterogeneous catalysis and (bio-) electrocatalysis, LEDs, photodetectors, energy-harvesting systems, (optical) sensors, SERS substrates, broad-band optical limiters, color conversion layers, gas storage, thermoelectric materials and transparent conductive substrates.[83]

The successful application of gels and aerogels depends strongly on the challenging issues of handling and technological integration into device architectures. Therefore, the work presented here aimed to improve the processability of metallic gels by grafting them to several kinds of substrates as well as producing hybrid materials with polymers. The porous structure of gels is infiltrated with polymers in order to gain mechanical strength, chemical stability and shape-forming ability. Several kinds of coatings including transparent, thin films and conductive xerogel films have been developed making use of various preparation techniques. In addition, aerogel dispersions named inks were applied for surface modification of glassy carbon electrodes which enable electrochemical investigations, e.g. application in electrocatalysis.

It was stated in a recent publication[153] that the integration of nanomaterials into electrical devices for energy applications is complicated as it is predicated on conductive particle interfaces. Long-chain organics at the particle surface prevent facile electron transport. One of the approaches to overcome this problem is the sol-gel particle assembly which provides ligand removal coupled to direct inter-particle bonding.[153] Gel networks solely made from metal NPs especially those which show a strong coalescence and merging of the initial building blocks meet the requirements for electrical conductive materials with structuring on the nanoscale. For that reason, the evaluation of charge transport phenomena and physical properties is addressed in the following chapter as the electrical resistances and Seebeck coefficients of xerogel films and aerogel monoliths are measured. Moreover, based on these results the applicability and required modifications of NP-based aerogels for their use as thermoelectric materials are discussed.

4.1. Hybrid materials*

An important approach allowing better handling of the originally fine and fragile NP-based aerogels is their hybridization with organic polymers. Cross-linking with polymers has previously been applied to improve the mechanical properties of SiO_2 aerogels.[50,51,154] In the case of colloidal NP-based aerogels, mechanical improvement may be even more important, taking into account the delicate nature of the interparticle connections and network. The infiltration with polymers leads to a mechanically stable hybrid material since the pores of the aerogel are completely filled with polymer. Cutting, shaping, slicing and a subsequent partial or complete removal of the polymer e.g. by plasma treatment or suitable solvents to gain the required geometries of aerogels is conceivable.

For the preparation of such a gel-polymer hybrid material the pores are infiltrated with a monomer solution and the polymerization is subsequently induced directly inside the network structure provided by the gel. Several kinds of monomers were tested, e.g. ethyl cyanoacrylate which undergoes an anionic polymerization immediately after contact to air humidity. A piece of Au-Ag-Pt aerogel was soaked with this monomer solution and cured for several hours. The resulting material was examined with SEM after focused ion beam (FIB) preparation of a cross section which is shown in Figure 4.1 (a).† Prior to FIB cut a platinum layer was sputtered on top of the piece of hybrid material to protect the specimen surface from damage during the preparation. The homogeneous appeal of the hybrid structure reveals that the network within the aerogel is retained during the infiltration process and the pores are completely filled with the polymer. The network structure of the aerogel still percolates the polymer matrix, which is an important issue with regard to energy and charge transport in the hybrid material. It shall be noted that the infiltration with a polymer solution and a subsequent curing has not been realized yet for semiconductor NP-based aerogels since this method leads to a deformation of the porous structure. This underlines the mechanical strength of the multimetallic aerogels. However, due to the high viscosity of the polymer solution this approach is limited to the infiltration of small pieces of the aerogel (smaller than ca. $20\,\text{mm}^3$).

An alternative preparation procedure is used in the case of poly(methyl methacrylate). Here, the initial solvent of the hydrogel is first replaced with acetone and further substituted by the organic monomer methyl methacrylate (MMA) (see Figure 4.1 (b)). Radical polymerization is induced by addition of azobisisobutyronitrile (AIBN). After a curing time of several hours a solid piece of hybrid material is obtained and no damage of the monolithic shape is observed as revealed by Figure 4.1 (c). It has to be noted, that this approach is general and seems to be applicable to many polymer materials with various functionalities. However, limitations may occur within the choice of suitable solvents for the monomers which also fulfill the criterion to be mixable with the gel media and in the strong shrinkage of some polymers during the polymerization process which may lead to collapse of the pores within the gel network.

---

*Parts of this section have already been published.[20]

†The FIB cut preparation of the cross section and the SEM investigation of the sample were performed by P. Formanek (IPF Dresden)
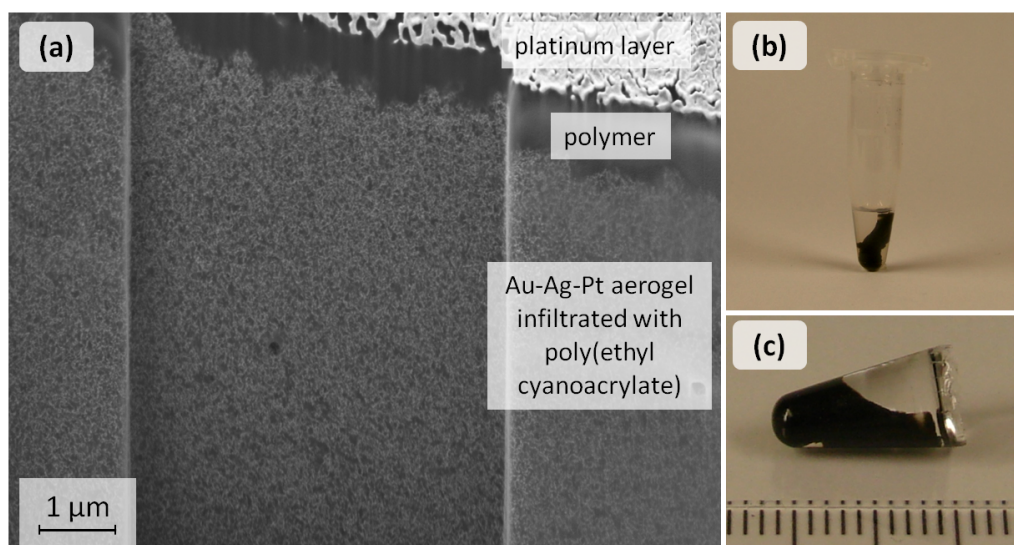
Figure 4.1.: *(a) Cross section of an Au-Ag-Pt aerogel infiltrated with poly(ethyl cyanoacrylate). The network structure of the aerogel is retained during the process while the pores are completely filled with polymer. The platinum layer was sputtered on top of the sample before the FIB cut to protect the specimen surface from damage by ion beam. (b) Au-Ag gel structure infiltrated with a monomer solution containing methyl methacrylate. (c) Solid piece of hybrid material obtained after radical polymerization of sample (b). No damage of the monolitic shape is observed. Part (a) was adapted with permission from reference.[20] Copyright 2014 American Chemical Society.*

4.2. Coatings[‡]

The successful application of gels and aerogels is very much dependent on efficient addressing (e.g. electric contacting, coupling to waveguides and electrode surfaces, etc.) and on their manipulation (e.g. insertion into and removal out of reaction mixtures as in the case of catalysis and hybridizing with other functional layers and structures). One of the important steps to face these requirements and promote the processability of aerogels is the fabrication of coatings on various substrates. Indeed, conductive patterned substrates will enable contact and various kinds of electric-transport measurements, transparent substrates might be required for coupling with optical systems, and conductive, inert supports are optimal for electrochemical investigations. Aerogels fixed on surfaces are easy to handle as heterogeneous catalysts, and they may be combined with microfluidic reactors as catalytic or sensory units. Moreover, thin-films from metallic networks may find applications as transparent conductive coatings. Not without reason, the importance of the fabrication of thin-film aerogels was mentioned by BROCK et al. already in their early work.[60]

Recent publications deal with the formation of sol-gel films from semiconductor NPs.[70,72] On the one hand xerogel films are prepared by ambient drying of wet gel films on im-

---

[‡]Parts of this section have already been published.[20]

mersed glass substrates.[70] Micron thickness films with high transparency and lumines-cence and a surprisingly high conductivity of 10^{-3} S/cm are prepared by this technique. On the other hand gelation strategies were applied to preformed spin-coated NP films.[72] This approach leads to sol-gel films with improved charge transport properties as shown by enhancement of the electrochemical photocurrent under white light illumination.

In the present work several techniques and substrates were evaluated for the preparation of coatings and films from metallic aerogels. Transparent thin films as well as xerogel films with thickness of few micrometers were developed. The later are suitable samples for determination of the resistivity of metallic gel networks. Furthermore, the structure of aerogel samples after re-dispersion and their use in surface modification of glassy carbon electrodes was studied.

4.2.1. Transparent thin-film coatings

Transparent conductive oxides like indium tin oxide (ITO) are commonly used for fabrica-tion of transparent electrodes which are implemented in a huge variety of optoelectronic devices and displays. Deposited as a thin film they provide a low resistance but at the same time high optical transparency. Nevertheless, these materials suffer from high costs and a lack of flexibility of the thin-film layers which prevents their applicability in fab-rication of flexible electrodes. For that reasons potential alternatives for the fabrication of transparent electrodes are widely discussed in the literature.[155] For example carbon nanotubes,[156,157] graphenes,[158] thin metal films,[159] conductive polymers,[160,161] net-works of Ag,[162,163] Cu[164,165] or noble metal nanowires[166] and even combinations of these materials[167] have been proposed for the replacement of ITO. It shall be noted that the widely studied Ag nanowire networks suffer from oxidation, corrosion and stability issues especially under harsh conditions. These problems could be overcome and life time of devices might be increased by the use of nanostructures from noble metals such as Au or Pt.[166]

As discussed in the beginning of the chapter it is expected that the particle coalescence and merging within the interconnected networks of metallic gels should facilitate the electron transport along the nanochains and avoid junction resistance. Hence, metallic NP-based gels are promising candidates for fabrication of conductive coatings. At the same time a high transparency has to be ensured. Thus, the fabrication process aims to the creation of a thin but percolated network of nanowires deposited on a suitable support material. Glass substrates are used as a basic support material throughout experiments presented in this section. In order to enhance interactions and thereby enable homogeneous deposition of the metallic nanochains the glass surface needs to be modified. Attractive forces between the silica surface and the metal nanostructures can be based on either electrostatic interac-tion or on interaction with functional groups such as thiols and amines. Several methods for surface modification of the substrates as well as for preparation of the nanochain net-

works were examined and the most promising results are presented in the following.

In the first example the glass surface is covered with thiol groups by esterification with MPA und subsequently decorated with Au NPs by immersing the substrate into an aqueous colloidal solution for several hours. After removal from the colloidal solution, the excess Au NPs were washed off carefully. The obtained Au NP-decorated substrate was finally placed vertically in the reaction solution which contained a high concentration of Au and Ag NPs. Afterwards the gel formation was performed at 75 °C according to the temperature-controlled approach described in Chapter 2.1. After entire Au-Ag hydrogel formation the substrate is finally removed from the solution and dried carefully under ambient conditions. The Au NPs which were first bounded to the substrate during the surface modification process are intended to act as seeds for the formation of nanochains and network clusters directly on the surface of the glass substrate during the gel formation. SEM images of the coating which is eventually obtained by this multistep procedure are shown in Figure 4.2. In lower magnification (Figure 4.2 (a)) the inhomogeneous distribution of the metallic nanostructure on the surface is obvious. Whereas a closed network is displayed in the upper part of the image some areas are even not covered with nanochains at all. Figure 4.2 (b) shows a magnification of the lower part of Figure 4.2 (a). Although small clusters of the metallic compounds are grafted on the surface they are separated from each other which prevent electrical contact. However, higher magnification reveals that these clusters are composed of gel-like networks of thin nanowires which are bonded to the surface (Figure 4.2 (c)). Moreover, several single metal NPs are observed which indicates a successful premodification of the glass surface. To sum up, even though nanowires bound to the surface, no homogeneous and percolated network was obtained by this approach. Consequently it seems not surprising that this substrate exhibits no measurable electrical conductivity.

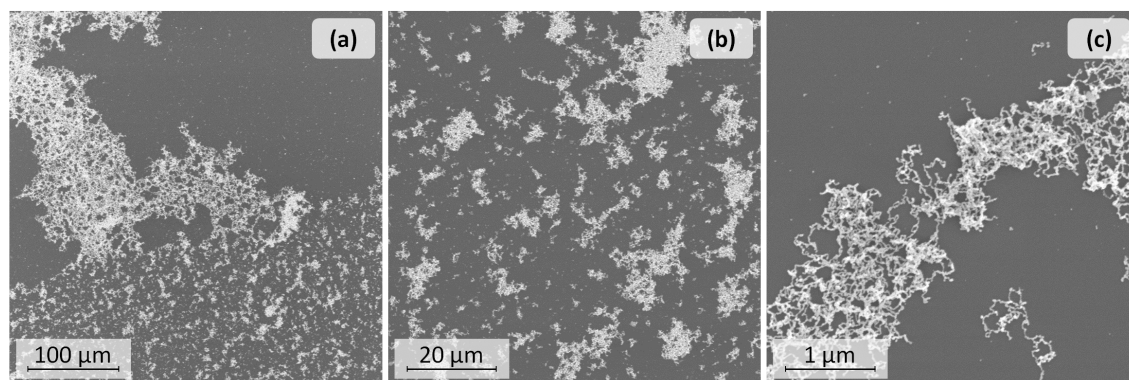**Figure 4.2.:** *SEM images of an Au-NP decorated glass surface coated with Au-Ag nanochains. The premodified glass substrate was immersed in the NP solution during the hydrogel formation. The distribution of the metallic network is inhomogeneous (a). Separated clusters have been formed on the surface (b) but in higher magnification the grafting of single NPs and nanochains as well as a partial network formation are revealed (c).*

In a second approach the glass substrates were first modified with the polyelectrolyte polydiallyldimethylammonium chloride (PDDA) to gain improvement of their attractive properties toward metallic nanochains and gel fragments by enhancement of electrostatic interactions. The Au nanochains used for preparation of the coating were synthesized according to a method described by PEI et al.[106] Here, the reduction of metal salt occurs in the presence of a limited amount of citrate which leads to the formation of interconnected nanowires instead of spherical NPs. The applicability of this approach for the formation of gels and aerogels has already been shown.[97] However, under suitable conditions the Au nanochains and small gel fragments are stable in dispersion for several days and can be applied for covering of the PDDA modified glass surface. A transparent and homogeneous coating is depicted by the inset of Figure 4.3 (a) and a homogeneous coating with thin nanowires is also revealed by the corresponding SEM image. Besides, this approach shows potential for controlling the thickness and particle density by variation of the immersion time. Nevertheless, it is assumed that still no percolated network of nanochains was formed since the final substrate did not offer any measurable conductivity.
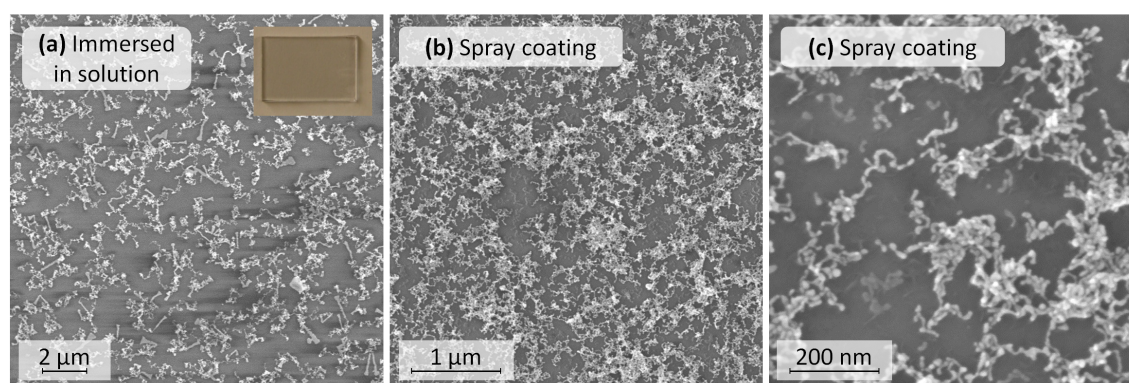
Figure 4.3.: *(a) SEM image of a PDDA modified glass surface coated with Au nanostructures by immersing the substrate into the preformed nanochain dispersion. Even though the nanochains were homogeneously distributed on the surface no percolated and conductive network was obtained. The transparent and uniformly grayish-colored substrate is shown in the inset. (b, c) SEM images of a coating obtained by a spray-assisted layer-by-layer deposition. PDDA and Au nanochains (prepared by the ion-induced approach) were deposited alternately on the glass surface. The composite film provides a transmittance of 80 % and a sheet resistance of 30 kΩ. Part (a) was adapted with permission from reference.[83] Copyright 2012 American Chemical Society.*

So far only a single deposition step was applied in order to cover the surface of the substrate. In contrast, the coating depicted in Figure 4.3 (b, c) was obtained by a layer-by-layer deposition.§ Therefore a homemade spray-deposition set-up was applied.[169] PDDA solution and an aqueous dispersion of Au nanochains were alternately deposited

---

§Preparation of substrates by spray-assisted layer-by-layer deposition and characterization of the sample were performed by P. Mundra (Physical Chemistry, TU Dresden).[168]

Table 4.1.: *Summary of different techniques, metallic nanomaterials and surface modifications applied for the preparation of transparent thin-film coatings on glass substrates.*

SEM image	Modification of glass substrate	Preparation of metallic nanochains and networks	Deposition technique and conditions
Figure 4.2	esterification with MPA and decoration with Au NPs	Au-Ag hydrogel formation by the temperature-controlled approach	substrate immersed in solution during the hydrogel formation
Figure 4.3 (a)	PDDA	Au nanochains prepared with low amount of citrate according to PEI et al.[106]	substrate immersed in the preformed dispersion of nanochains
Figure 4.3 (b,c)	PDDA	Au (Ag$^+$) nanochains prepared by the ion-induced approach	spray-assisted layer-by-layer deposition

on the surface. Due to the large dimensions and limited diffusion of the nanochains and gel fragments compared to single particles, the deposition time had to be extended and adjusted. The Au nanochains are prepared according to the ion-induced approach described in Chapter 2.2. Only a limited amount of Ag$^+$ ions was added to the Au NP solution to induce the formation of nanowires and network fragments but to prevent the formation of a compact hydrogel. As revealed by SEM (Figure 4.3 (b)) a homogeneous composite film with a quite dense network of metallic compounds was obtained by this approach. In higher magnification (Figure 4.3 (c)) separated nanochains as well as agglomerated and overlapping clusters are observed. Agglomeration of nanostructures may occur during the drying process on the surface of the substrate but also by interconnection of nanochains in the initial dispersion. In the SEM image also nanochains with a much lower contrast are depicted which are assumed to be deposited in a prior layer of the composite film. The obtained substrate shows a grayish color and a transmittance of 80 % was measured. Moreover, a sheet resistance of 30 kΩ was determined. Hence, the prepared coating do not offer the minimum industry requirements of transmittance > 90 % and sheet resistance ≤ 100 Ω.[166] Since a percolated network of nanochains was revealed by the SEM images it is assumed that conductivity is limited by the insolating polymer layers of PDDA. They prevent network formation and electrical contact between nanochains deposited in different layers. In order to improve conductivity throughout the multilayers a thermal annealing under mild conditions or removal of the polymer by plasma treatment are suggested.[168]

The various surface modifications, metallic nanostructures and deposition techniques investigated for the preparation of transparent thin-films are summarizes in Table 4.1. Al-

though no preparation of a satisfying transparent conductive coating was achieved yet, the presented results constitute promising starting points for further improvements. Indeed, grafting of nanochains on the modified glass surface was achieved for all methods and moreover the PDDA pretreated substrates stand out due to the homogeneous coatings that were obtained. Furthermore, it was shown that dispersions of Au nanochains prepared by the ion-induced approach are suitable inks for application in a spray-deposition setup. It is indicated by the results that the use of preformed and stable dispersions of nanochains should be favored compared to a simultaneous performance of gel formation and substrate coating. This provides more control and flexibility of the process parameters. The layer thickness may be tuned by variation of the immersion time and by application of multilayer deposition. The later seems the most promising approach to fabricate percolated networks and achieve reasonable conductivity of transparent films. However, as discussed above the insulating effect of the polymer matrix needs to be overcome by interconnection between the metallic compounds of different deposition layers. In the case of thermal annealing steps of the film also the thermal stability of the nanostructures as described in Chapter 3.2 should be taken into account.

Additionally, plasmonic metal nanostructures are known to cause an enhancement of the local electrical field which can be used to strongly improve the sensitivity of Raman spectroscopy.[109,170,171] For that reason some preliminary investigations concerning the SERS activity of the prepared thin-film coatings were performed.[¶] The probe molecule rhodamine 6G was detected even in the lowest applied concentration of 10^{-8} M when dropped on a substrate modified with Au nanochains. The specimen was prepared similar to the one shown in Figure 4.3 (a) but (3-aminopropyl)trimethoxysilane (APTMS) instead of PDDA was used to modify the glass surface. Detailed investigations are needed to verify the performance of metallic gels regarding the preparation of SERS substrates and further experiments are pending.

4.2.2. Xerogel films and electrical conductivity

The techniques presented in the previous section aim on the preparation of transparent and thin-film coatings. Alternatively, metallic xerogel films of several micrometer thickness can be deposited on glass substrates. The fabrication of these coatings displays another example of the successful processing of metallic gels with potential use for example in the fields of catalysis and sensors applications. Moreover, due to their defined macroscopic geometry these are suitable samples for determination of the resistivity of metallic gel networks.

The preparation of xerogel films follows a simple approach and no modification of the surface of the glass substrates is required. In an earlier experiment a glass substrate was vertically immersed directly into a hydrogel solution, and the deposition of the film was

---

[¶]SERS measurements were performed by S. Klosz (Physical Chemistry, TU Dresden) under the supervision of C. Ziegler (Physical Chemistry, TU Dresden).

performed by slow evaporation of the aqueous phase. Since no supercritical drying is applied the resulting metallic network is named xerogel. A black and non-transparent coating of the whole surface was obtained (see inset of Figure 4.4 (c)). A layer thickness of about 2 μm is determined by profilometer measurements and the resulting structure is characterized by SEM (Figure 4.4 (c)). Even after non-critical drying the structure shows high porosity and a network of interconnected and interwoven nanochains.

In a next step the preparation pathway was optimized in order to gain more control on the film thickness and homogeneity. At the same time the film preparation process was accelerated considerably. This was realized by first exchanging the aqueous phase in the pores of the hydrogel against acetone. This process is well known from the preparation steps prior to supercritical drying. In order to destroy the compact structure of the monolith the gel was first dispersed in solution by a short sonication step. Finally a glass substrate was horizontally immersed in the gel dispersion. The coating of the substrate was obtained by evaporation of the solvent at room temperature while shaking and even moving of the sample needs to be avoided. The process is fastened due to the highly volatile solvent and a quite homogeneous deposition is ensured by the horizontally immersed substrate.

This technique was applied to Au-Pd and Pt-Pd samples and suitable xerogel coatings with film thicknesses of 1.2 μm and 2.3 μm as estimated from profilometer measurements were obtained, respectively. High porosity and an open pore system are revealed by the SEM cross section profiles of similar specimens (Figure 4.4 (a, b)). The scratches were prepared artificially after deposition of the film in order to allow cross section imaging and determination of film thickness. It should be emphasized that even after dispersing the gel in solution by sonication and rearrangement of the network during the film formation no collapse of the porous network or agglomeration of nanowires were observed. However, ambient drying of the network is assumed to result in certain losses of porosity and pore volume. It should be admitted that full control of the thickness and porosity of the films demanded by each specific application needs more research. Moreover, critical point drying of wet gels and preparation of aerogel coatings may be necessary for fabrication of catalyst substrates with very large surface areas. Even though the set-up of the critical point dryer was adjusted and first attempts were executed, a non-destructive supercritical drying of a thin gel coating was not performed successfully yet and further efforts are required. Nevertheless, for many application fields drying under ambient conditions may already be sufficient since the porosity of the network, the accessibility of the pores and the metallic surface as well as the structure of nanochains is strongly preserved during the ambient drying of film of micrometer thickness. In addition this observation underlines the high mechanical stability of the porous systems formed by interconnection and merging of the metallic building blocks. Since no modification or functionalization of the glass surface was required it is assumed that the film formation and adhesion to the surface are simply based on the sedimentation of the gel and the evaporation of the solvent. Hence, the approach is supposed to be adaptive to various kinds of substrates with different surface chemistry.
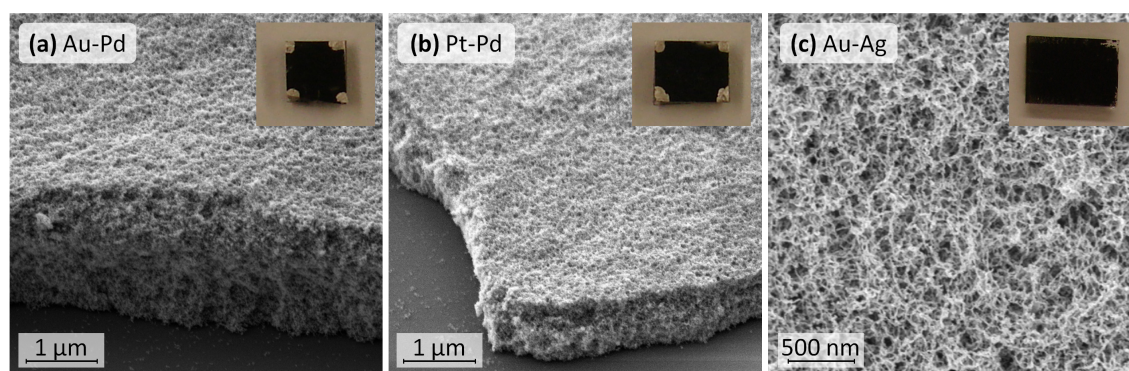
Figure 4.4.: *SEM images of bimetallic xerogel films on glass substrates. The porous network of nanochains is retained during the ambient drying of the micrometer thick films. Insets show photographs of the corresponding samples which provide sizes of 0.5 cm × 0.5 cm (or 0.7 cm in the case of (c)). A black, non-transparent and homogeneous coating is obtained by the approach (insets). Contacts at the edges of the substrates (inset (a) and (b)) are made from silver paint and are applied to ensure stable electrical contact during various characterization procedures. Part (a)and (b) were adapted with permission from reference.[20] Copyright 2014 American Chemical Society. Part (c) was adapted with permission from reference.[83] Copyright 2012 American Chemical Society*

The electrical conductivity is a crucial property of materials aiming for applications in thermoelectric devices or electrocatalysis. Due to this, the resistances of metallic gels need to be characterized. Thereby, the investigation of films instead of irregular shaped monoliths is advantageous. Taking into account the defined geometry and the known film thickness also a specific resistance can be calculated which enables comparison of the values among each other and to the values of other materials e.g. the bulk metals. The corresponding data are summarized in Table 4.2.

In a first approach the sheet resistance of an Au-Ag xerogel film was measured via a four point setup to be as low as $2\,\Omega$ which corresponds to a specific resistance $3.6\,\Omega\cdot\text{mm}^2/\text{m}$.[97]

Table 4.2.: *Summary of the results from the resistivity measurements of bimetallic xerogel films.*

sample	sheet resistance [Ω]	film thickness [μ]	specific resistance [$\Omega\cdot\text{mm}^2/\text{m}$]
Au-Pd xerogel film on glass	1.8	~1.2	2.2
Pt-Pd xerogel film on glass	2.4	~2.3	5.5
Au-Ag xerogel film on glass	1.8	~2.0	3.6

However, it shall be noted that the application of a four point setup for characterization of samples with less defined geometry is challenging. The measurement technique of the specific resistance can be markedly improved by applying the van der Pauw setup.[172,173] It is designed to measure the electrical sheet resistance of homogeneous, thin but irregular shaped films. In the case of the van der Pauw setup four contact points are positioned at the periphery of the film. Two of them are used to apply a current whereas the others are utilized to measure a voltage. After circular permutation the layer resistance can be calculated. The applied home-built van der Pauw setup and details concerning the calculation of the sheet resistance and the specific resistance are presented in the Experimental Section.

Taking into account the layer resistance and the film thickness of the samples a specific resistances of about $2\,\Omega\cdot mm^2/m$ and $5\,\Omega\cdot mm^2/m$ were obtained for Au-Pd and Pt-Pd xerogel-films on glass substrates, respectively. These values are only 2 orders of magnitude higher than those for the corresponding bulk metals which underline the high electrical conductivity of the multimetallic nanostructures obtained by this approach. A slightly higher value for Pt-Pd materials is not surprising since Pt and Pd as a bulk material show a five times higher specific resistance compared to Au.

The electrical conductivity of a material is determined by the charge carrier density and mobility whereas the mobility is mainly limited due to scattering effects. The mean free path of electrons in a bulk metal at room temperature is known to be typically around several hundred Ångström.[174] Hence, structures which provide dimensions in the order of the mean free path or even below are supposed to show a strong decrease in the electrical conductivity. Elastic electron-scattering processes are strongly enhanced due to additional collision with the surface and the grain boundaries. This effect has already been described in the literature for various metallic nanostructured materials such as thin polycrystalline metal films,[174,175] metal NP assemblies[176] and also nanocrystalline materials.[177]

The size of crystallites within the NP-based gel structure was determined to be below 5 nm and a high surface area as well as a huge variety of grain boundaries was observed. These properties lead to an increase of the resistivity compared to bulk metals but still reasonable high values of conductivity were quantified. In a review published in 2008 that deals with assemblies of NPs with various organic linkers a highest value of conductivity in Au NP assemblies of $2\cdot10^5\,\Omega^{-1}\cdot cm^{-1}$ obtained by LIU et al. is stated.[176,178] Other studies that were highlighted in the review deal with three-dimensional assemblies of Au NPs linked by dithiols or carbamate derivates[179] and mulitlayer films prepared by assembly of Au and Ag NPs via bifunctional cross-linkers with variable length.[180] They report resistivity values in the range of 10^{-6} to $10^{-4}\,\Omega\cdot m$. With a resistivity of about $10^{-6}\,\Omega\cdot m$ the xerogel films presented here are at the top levels of this range. It shall be underlined that the high conductivity of metallic gels is attributed to the direct coalescence of particles without any linker molecules which markedly reduce junction resistances. Since the structure of nanowires and interconnections are mainly retained during the ambient drying of the xerogel film it is assumed that statements concerning the electrical conductivity are even applicable to aerogel structures.

4.2.3. Ink preparation and coating of glassy carbon electrodes

Metallic aerogels are highly promising electrocatalysts as they provide high surface area without the use of supporting materials and their nanostructuring and particle coalescence are believed to improve their electrochemical performance and long term stability. Also in this case the processability of the aerogels and integration of the materials into electrochemical systems and devices play a crucial role. Thus, the fragile nanostructure of the aerogel has to be transferred to an electrical conductive substrate without causing damaging or collapse of the porous, fragile network and without destroying the particle coalescence. Various studies on the excellent performance of metallic aerogels in electrocatalysis[90,92,94] and bioelectrocatalysis[91,95] have already been performed. In all cases the initial solid aerogels used as electrocatalysts were well characterized regarding their inner surface area, structure of nanochains and appearance of the three-dimensional network in SEM. In a typical experiment the solid aerogel is dispersed in a solvent, dropped on the surface of a glassy carbon electrode, dried under ambient conditions and finally immersed in the electrolyte in order to perform the electrochemical investigations. Nevertheless, no information on the final structure of the metallic compounds in the dispersion as well as on the morphology and porosity of the network after drying on the glassy carbon surface was given. Hence, with regard to the application in electrocatalysis the distribution and morphology of the network after drying on a typical electrode material, namely glassy carbon, are investigated in this subchapter.

For the preparation of the dispersion, termed ink, a typical composition and procedure were used. A Pt_{50}-Pd_{50} aerogel was spread in a solution containing water and isopropanol. Moreover, a small amount of Nafion® was added to the solution since this polymer is widely used to improve the stability of the dispersion as well as the adhesion of the metallic compounds to the glassy carbon surface. In order to homogeneously disperse the aerogel in the solution the mixture was treated with a horn sonicator for at least 15 minutes until a black and clear dispersion without visible fragments of solid was obtained (see Figure 4.5 (c)). Even after this harsh treatment the particle coalescence and structure of nanowires is retained as proven by the TEM analysis (Figure 4.5 (a, b)). In the overview image still an extended network of nanochains is observed and in higher magnification the unchanged morphology of the nanochains as compared to the initial aerogel (see Figure 2.3 (b)) is obvious.
In order to modify the electrode with the aerogel material a small volume of the dispersion was dropped on the polished glassy carbon surface and dried under ambient conditions. The distribution and porosity of the gel network were investigated by SEM directly on the electrode surface (Figure 4.6). A metal loading of 20 $\mu g/cm^2$ was chosen for investigation as it is a typical value used in electrocatalytic experiments. In low magnification images it is obvious that the electrode surface is partially covered with gel fragments. The distribution of the metallic nanostructures is quite homogeneous and only a slightly higher coverage in the center of the electrode was observed. The network fragments show various sizes, ranging from single nanochains up to clusters with several micrometers in diameter. In higher magnification it is observed that also the larger and three-dimensional clusters
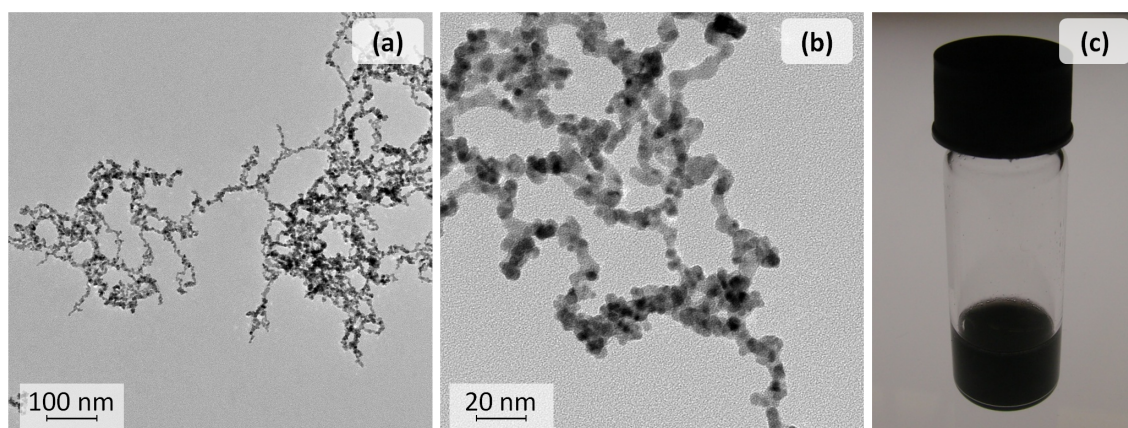
Figure 4.5.: *a, b) TEM images of an ink prepared from a Pt-Pd aerogel. The particle coalescence and structure of nanowires is retained even after the harsh treatment. (c) A black and well dispersed solution of the aerogel sample is obtained with the help of a horn sonicator.*

show a highly porous structure. In summary, it has to be stated that the porous structure and the coalescence of NPs within the nanochains are retained during the preparation of the electrode. For that reasons, the accessibility of the metallic surface and the advantageous properties of the nanostructure are ensured. Nevertheless, some loss of porosity may occur due to dispersing and subsequent ambient drying. Moreover, it shall be noted that the investigated Pt-Pd sample was prepared according to the temperature-controlled approach and the obtained results cannot be simply assigned to metallic aerogels prepared by other techniques since they may differ regarding the stability of the initial network structures.
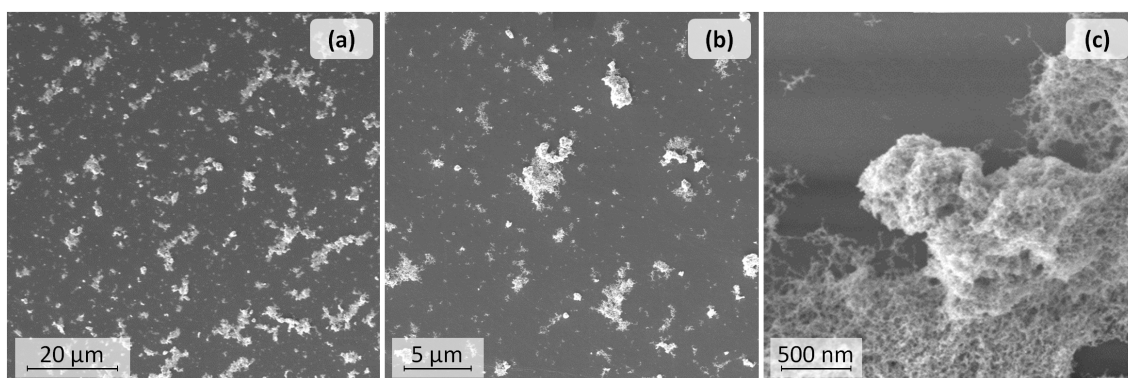
Figure 4.6.: *SEM images of a glassy carbon surface after deposition of a Pt-Pd aerogel dispersion. A metal loading of $20 \, \mu g/cm^2$ was applied. The metallic nanostructures of different size are quite homogeneously distributed on the electrode surface (a, b). In higher magnification the retaining of the porous structure of the three-dimensional clusters is proven (c). Hence, the accessibility of the metallic surface and the advantageous properties of the aerogel nanostructure are ensured after preparation of the modified electrode.*

In addition, also on glassy carbon surfaces continuous xerogel films were obtained by ambient drying of gel dispersions (Figure 4.7). Even though the surface homogeneity suffers from several cracks which can be seen in lower magnification SEM (Figure 4.7 (a)) this may not influence the electrocatalytic performance since the electrical contact to the electrode surface is ensured in all cases. Figure 4.7 (b) illustrates a porous structure throughout the whole cross section of the layer. Although a fine network of nanowires is depicted in higher magnification (Figure 4.7 (c)) a loss of porosity compared to the corresponding aerogel has to be admitted. It is emphasized that the system of open pores and cracks may provide a large and easily accessible surface for electrocatalytic conversion of reactants.
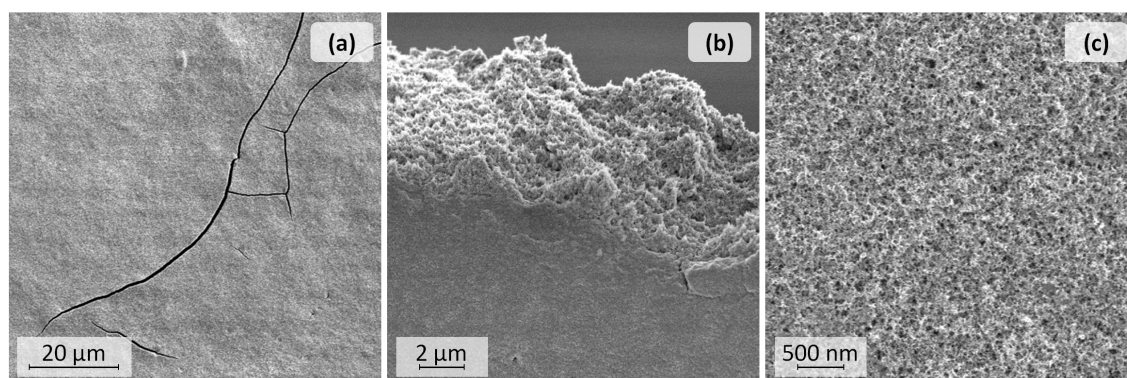

Figure 4.7.: *SEM images of a xerogel film on a glassy carbon surface obtained by ambient drying. (a) Small cracks in the coating may not reduce the electrocatalytic performance as long as electrical contact between the metallic structure and the electrode surface is ensured. (b) The cross section image reveals the porosity of the whole film. (c) In higher magnification the network of nanowires is depicted. Even though a porous structure is observed a slight loss of porosity compared to the initial aerogel is concluded.*

In future experiments the direct surface investigation of the glassy carbon electrode by means of SEM could be adopted to compare the morphology of the metallic catalyst before and after the performance of electrochemical investigations. These results could be correlated with the data from other techniques (e.g. CO stripping voltammetry, cycling voltammetry, TEM, EDX, EXAFS) to gain deeper understanding of the stability and structural changes of the metallic nanostructures during the electrochemical performance and stress.

4.3. Determination of Seebeck coefficients and evaluation of thermoelectric properties

The Seebeck effect describes the phenomena of a voltage difference (dV) between two points of different temperature (dT) in a conductor or semiconductor. The Seebeck coefficient α_S, often also called the thermoelectric power, gauges the magnitude of this effect.

It is a material property that depends on temperature.

$$\alpha_S = \frac{dV}{dT} \tag{4.1}$$

Typical values for α_S in semiconductors are about $200\,\mu V/K$ whereas the effect is much smaller in metals and the corresponding Seebeck coefficients are in the $10\,\mu V/K$ range.[181]
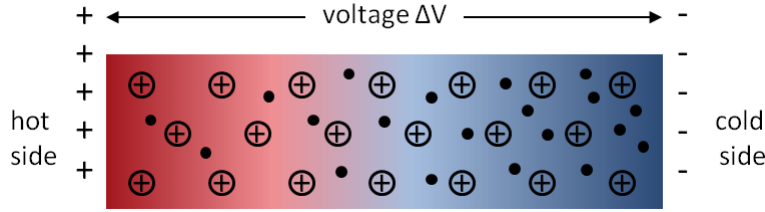

Figure 4.8.: *Schematic representation of the Seebeck effect. Electrons from the hot side have a higher energy and diffuse to the cold side thus a voltage difference between both points is induced. Graphic adapted from reference.[182]*

The thermoelectric effect can be described with the help of a simple model: A piece of metal that is heated on one side is considered. At raised temperature the Fermi-Dirac distribution of the electron energies extends to higher values. Hence, the average energy per electron is increased in the hot region. The more energetic electrons have greater velocities and diffuse towards the cold region. This leads to an excess of electrons on the cold side and consequently to the development of a voltage between the hot and the cold end. This effect is also schematically displayed in Figure 4.8. It is given by convention, that the sign of α_S represents the potential of the cold side with respect to the hot side.[182] Thus, the Seebeck coefficient is negative if electrons diffuse from the hot to the cold side which means that the cold side is negative with respect to the hot side. It shall be noted that this basic explanation assumes that the conduction electrons are free within in the metal. However, since the scattering of the conduction electrons e.g. by interaction with the metal ions and the lattice vibrations has to be considered, the Seebeck coefficient in metals can be both negative and positive. If the mean free path of the electron decreases strongly with increasing energy the electrons will migrate from the cold to the hot side which results in a positive value of α_S. This is true for several metals as for example Au, Ag and Cu in the bulk phase.[182]

The Seebeck coefficient of a new material is commonly determined by measuring the net Seebeck voltage of a thermocouple that is composed from the material of interest and a standard compound. With the knowledge of the α_S value of the reference material also the absolute Seebeck coefficient of the specimen can be calculated. Several techniques were used to evaluate the Seebeck coefficients of metallic NP-based aerogels and corresponding xerogel films. Therefore a temperature gradient was induced in the specimen and the resulting voltage was measured. The applied methods vary with regard to the setup geometry and the technique used for determination of the temperature difference.

It shall be noted that the evaluation of Seebeck coefficients of the fragile, porous and irregular shaped aerogel specimens is a highly challenging task and depends on the use of specialized and adjustable equipment. Therefore, homemade setups designed and installed by the group of Dr. Min Gao from the Cardiff School of Engineering were applied throughout all experiments described in the following.[183,184]

4.3.1. Seebeck coefficients of xerogel films

A setup which is applicable to thin and continuous coatings grafted on substrates was applied to determine the Seebeck coefficients of bimetallic xerogel films deposited on glass substrates. The sample is fixed on a stage and touched with two conductive probes whereas one of it can be heated by applying a current. The induced temperature gradient is analyzed by a temperature mapping microscope while the Seebeck voltage between the hot and the cold probe is measured.[183] In addition, the whole stage can be heated to enable the investigation of the temperature dependence of the Seebeck coefficient. Details concerning the setup and the evaluation of data can be found in the Experimental Section.

The results from different bimetallic xerogel films including average temperature (mean value of temperatures from hot and cold probe), temperature difference between the two probes, Seebeck voltage and calculated Seebeck coefficient are summarized in Table 4.3. The values determined for the bimetallic xerogels are in the same order of magnitude compared to those of the corresponding bulk metals (see Table 4.5). In the case of Pt-Pd xerogel a striking low Seebeck coefficient of about $0.2\,\mu V/K$ was determined which is considerably smaller than the values of the corresponding bulk metals. A damage of the film by scratching or a loose contact due to brittleness of the material cannot be completely excluded since the setup provides only a limited control over the accurate and gently positioning and fixing of the probes.

Table 4.3.: *Average temperature (mean value of temperatures from hot and cold probe), temperature difference between the two probes, Seebeck voltage and calculated Seebeck coefficient for several bimetallic xerogel films on glass substrates (no silver paint contacts where applied for these samples).*

xerogel film on glass substrates	T_a[K]	ΔT [K]	V_S [μV]	α_S [μV/K]
Au-Ag	301.8	8.7	-11	**-1.3**
Au-Pd	302.4	8.5	33	**3.9**
Pt-Pd	305.8	14.7	3	**0.2**

In addition, the temperature dependence of the Seebeck coefficient was evaluated in the case of an Au-Pd xerogel film. Small points from silver paint were placed at the corners of the sample in order to improve stability of the contact and avoid damaging of the sample by scratching. The results at different temperatures are displayed in Table 4.4. In order to avoid possible changes of the nanostructure due to elevated temperatures, the experiments were restrained to a temperature range of 300 to 345 K. Even though a slight decrease of the values with increasing temperature is observed this trend is inconsistent with the value at the highest evaluated temperature.

Table 4.4.: *Results of measurements at different stage temperatures for an Au-Pd xerogel film on glass substrate (small silver paint contacts were applied to ensure electrical contact and the mechanical stability of the touching points).*

xerogel film on glass substrates	T_a[K]	ΔT [K]	V_S [μV]	α_S [μV/K]
	302.4	8.5	19	**2.2**
	313.6	10.0	19	**1.9**
Au-Pd	324.7	11.0	20	**1.8**
	335.1	12.2	17	**1.4**
	344.7	11.0	18	**1.6**

Table 4.5.: *Seebeck coefficients of the corresponding bulk noble metals[182]*

bulk metal	α_S [μV/K]
Au	+1.94
Ag	+1.51
Pt	-5.28
Pd	-9.99

In summary, it has to be stated that within the evaluated temperature range the Seebeck coefficient of the xerogel did not exhibit a strong dependence on the temperature. The data concerning the Seebeck coefficients of the xerogel films are especially valuable since they provide corresponding data to the electrical resistivity measurement described in Chapter 4.2.2. The correlation between these physical properties will be discussed later in this subchapter.

4.3.2. Seebeck coefficients of metallic aerogels

Besides the characterization of xerogel films of course also the physical properties of the highly porous, free-standing aerogels are of great interest. Therefore, suitable setups for the investigation of aerogel monoliths were provided. In these experiments temperatures at the hot and cold side were measured via the Seebeck voltage of a thermocouple consisting of Cu and constantan which is integrated in the probe.[184] Those same conductive probes are also used to measure the Seebeck voltage of the sample. Moreover, one of the probes can be heated by applying a current and is accordingly used to induce a temperature gradient in the sample.

In a first approach aerogel monoliths were gently contacted by the help of sharp probes named micromanipulators which can be moved carefully in all three dimensions via micrometer screws.[184] As displayed in Figure 4.9 (a) metallic aerogels exhibit sufficient mechanical stability to be fixed and electrically contacted by the micromanipulators. This setup was used to measure the Seebeck voltage at several temperature differences between hot and cold probe. An Ag-Pt aerogel monolith was chosen for these investigations. The Seebeck coefficient of the sample can be calculated from each single measurement (see Table in the Experimental Section). Moreover, these data points can be brought into context to each other by fitting them as shown in Figure 4.9 (b). Assuming a constant Seebeck coefficient the voltage between the two probes (V_{DA}) would increase linearly with increasing temperature difference. The Seebeck coefficient can be calculated from the slope of the linear regression and a value of -1.4 μV/K was determined for the Ag-Pt samples. Further details concerning the setup and the calculations are given in the Experimental Section.
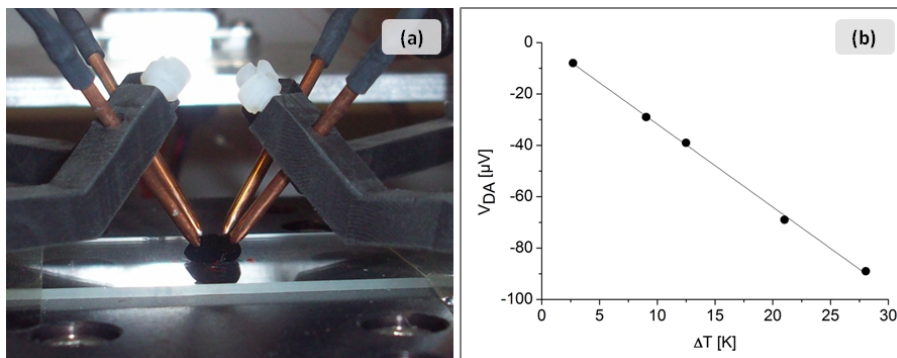
Figure 4.9.: *(a) The micromanipulator setup provides four probes which can be moved in all three dimensions with the help of micrometer screws. Only two of them are applied to determine the Seebeck coefficient. As proven by the experiments metallic aerogels provide sufficient mechanical stability to be fixed in the setup without cracking or deformation. (b) The plot displays the dependence of generated voltage between the two probes in dependence of the applied temperature difference. The Seebeck coefficient of the sample can be calculated from the slope of the linear regression.*

Table 4.6.: *Seebeck coefficients of several metallic aerogels evaluated by the hot probe technique. The numbers given in the sample names express the volume ratio of the initial monometallic NP solutions which were mixed before a joint gel formation was performed. Metal-like Seebeck coefficients were obtained for all aerogels. The deviation of the value in the case of Pd_{100} aerogel was attributed to measurement issues.*

sample (aerogel monolith)	α_S [μV/K]
Ag_{50}-Pt_{50}	-2.7
Ag_{25}-Pt_{75}	-2.3
Au_{50}-Ag_{50}	-1.1
Pt_{50}-Pd_{50}	+2.8
Pt_{33}-Pd_{66}	+3.5
Ag_{50}-Pd_{50}	+8.4
Pd_{100}(prepared without stabilizer according to reference[94])	+10.7
Pd_{100}	+65.4

The most suitable approach for investigation of metallic aerogel monoliths is the so called hot probe technique. The configurations of the setup and the adopted calculations are explained in the Experimental Section. Two plane Cu probes are gently pressed on the sample to ensure electrical contact. Moreover a temperature gradient is induced in the specimen as one of the probes is heated. Several metallic aerogel monoliths with various elemental compositions have been investigated and the results for are given in Table 4.6. The measurements are repeated at least 3 times for each monolith and the results are highly reproducible. Only in the case of the investigated Pd_{100} aerogel a strong fluctuation of the measured Seebeck voltage and a large deviation from Seebeck coefficients of other samples was observed. It is assumed that this behavior is not caused by a real feature of the sample but rather by measurement issues as for example loose electrical contact or unfavorable sample geometry. For that reason the data for Pd aerogels have to be confirmed by further measurements and the respective value is not taken into account for the current evaluation. In summary, also the results from the hot probe technique indicate that the NP-based aerogels provide metal-like Seebeck coefficients.

4.3.3. Discussion and perspective

Actually, Seebeck coefficients of metallic NP-based aerogels and corresponding xerogel films were reported for the very first time. The data obtained by the different techniques are consistent and reveal that Seebeck coefficients of metallic aerogels are in the same range and even below compared to the corresponding bulk metals. This gives rise to the conclusion that metallic properties are preserved within the network of nanochains ob-

tained by gel formation from separated noble metal NPs. Therefore, a strong coalescence and merging of the initial particles within the nanochains is assumed. Moreover, these results are in agreement with the high electrical conductivities of metallic xerogel films that were described in an earlier section. Both the electrical conductivity and the Seebeck effect strongly depend on the charge carrier density and mobility of a material and a correlation between both properties of the nanostructures is expected. Besides, it shall be noted that negative as well as positive values for the Seebeck coefficient were obtained whereas the latter are solely observed in the case of Pd containing samples. Positive values of α_S are assigned to an electron accumulation on the hot side of the temperature gradient and may be caused by strong scattering electrons at higher energies. The details of the structural features that cause the different signs of the Seebeck coefficients of metallic aerogels are still under investigation and not fully understood yet. However, lattice torsions and defects as well as grain boundaries and inhomogeneities of the elemental distribution are supposed to play a major role regarding this issue.

The thermoelectric effect displays the direct conversion of a temperature difference to an electric voltage and vise versa. This is of great interest for the application in power generation devices based on thermocouples of suitable materials. The efficiency of thermoelectric materials is represented by the dimensionless figure of merit ZT which is given in the following equation:

$$ZT = \frac{\alpha_S^2 \sigma}{\kappa} T \tag{4.2}$$

Z = figure of merit, T = average temperature, α_S = Seebeck coefficient, σ = electrical conductivity, κ = thermal conductivity

Thus, a high-performance thermoelectric material would provide a large Seebeck coefficient and a reasonably high electrical conductivity but at the same time a low thermal conductivity. The thermal conductivity is composed of two parts – a lattice thermal conduction via phonons and an electronic contribution due to inelastic scattering of the conduction electrons. In metals the thermal conductivity is dominated by the electrons and the reasonable close relation between the electrical and the thermal conductivity in metals is expressed by the Wiedemann-Franz law

$$LT = \frac{\kappa}{\sigma} \tag{4.3}$$

L = Lorenz number, T = temperature, σ = electrical conductivity, κ = thermal conductivity

Due to this fact and their high charge carrier density which leads to poor Seebeck coefficients pure metals are non-suitable thermoelectric materials even though they provide high electrical conductivity. In contrast, doped semiconductors are among the most promising candidates for developing of suitable thermoelectric materials. But still conventional materials are mainly limited to ZT = 1 at room temperature since the Seebeck coefficient, electrical conductivity and thermal conductivity are interrelated and cannot

be tuned independently. It shall be noted that an improvement of the performance at least to a threshold of ZT = 2 is required to possess performances comparable to that of conventional mechanical machines.[185] One approach to increase ZT values covers the development of low-dimensional thermoelectric materials.[186–189] These nanoscale materials have reached ZT = 2 at 300 K and even ZT = 3 at 450 K.[185] This remarkable improvement is attributed to the possibility of individually tuning the transport coefficients at the nanoscale. This opportunity is based on several effects. On the one hand lattice thermal conductivity is reduced due to scattering of phonons at physical boundaries of the nanosized structure. One the other hand the power factor $\alpha_S^2 \sigma$ was increased or at least retained with decreasing κ through size quantization or energy filtering of the electrons.[185]

Moreover, NP-based aerogels are attractive materials for investigation of their thermoelectric performances due to several reasons.
(1) Silica aerogels are well known for their exceptional low thermal conductivity. Their low density leads to a decrease of the solid thermal conductivity whereas the porous structure minimized the heat transport by the gas phase. Typical values of $0.02 \, \text{Wm}^{-1}\text{K}^{-1}$ are obtained for silica aerogels at 300 K in air.[44]
(2) The partial removal of insulating ligands and interconnection of NPs within the network structure may result in an improvement of the electrical conductivity. At the same time the variety of grain boundaries may lead to scattering of phonons and decrease the thermal conductivity.
(3) For the fabrication of usable devices the corresponding thermoelectric materials needs to be available on a large scale. Preparation pathways which ground on self-assembly of the building blocks and do not aim on highly ordered structures are certainly ahead regarding up-scaling of the process.
(4) The preparation of NP-based aerogels offers the possibility of interesting and manifold structural design. Especially the combination of different building blocks that can be realized by this approach is of high interest.

Apart from the results presented in this chapter only very limited data concerning the thermoelectric properties of NP-based aerogels are available yet. The micromanipulator setup presented in Chapter 4.3.2 was also used to acquire the Seebeck coefficients of metal-semiconductor mixed NP-based aerogels. The obtained values in the range of 100-200 μV/K seem to be dominated by the semiconducting material which is attributed to the inhomogeneous distribution of metal within the nanostructure. However, difficulties arise due to the high resistance and low mechanical stability of these aerogel monoliths which also prevent the use of the hot probe technique for evaluation of their Seebeck coefficients.[116] Moreover, the thermoelectric performance of hot pressed Bi_2Te_3 aerogels was evaluated by use of a physical property setup. Due to the pressing step the materials completely loose porosity and their ZT values are even below the ZT of corresponding Bi_2Te_3 NPs.[190]

It shall be noticed that the thermal conductivity of metallic aerogels was not investigated yet. Even though a relatively high value as typical for metals is expected, these measure-

ments are of great interest due to the remarkably high porosity and variety of grain boundaries offered by the nanostructure. Thus, future investigations aim on the evaluation of the thermal conductivity of thin xerogel (and aerogel) films by the 3ω-method.[191] Regarding their poor Seebeck coefficients it shall be stated that pure metallic NP-based aerogels are less suitable thermoelectric materials. Nevertheless, they provide excellent electrical conductivity which may enhance the performance of mixed metal-semiconductor aerogels. However, achieving a homogeneous mixing of the different building blocks within the porous network and combining the advantageous properties of metals, semiconductors and aerogels in one nanostructured material remain a challenging task.

4.4. Conclusion

NP-based aerogels provide exceptional properties which may allow their application in various fields of research. However, desired handling and technological integration of the fragile, porous and irregular shaped metallic aerogel monoliths into device architectures is crucial for applications but at the same time constitutes a challenging task. Therefore, the field of specific processing of gels and aerogels was promoted in this work by preparation of various kinds of coatings and synthesis of hybrid materials with organic polymers.

The infiltration with polymers provides an improvement of the mechanical stability and might offer shape-forming ability. A piece of multimetallic aerogel was infiltrated with ethyl cyanoacrylate which undergoes an anionic polymerization immediately after contact to air humidity. In the cross section profile gained by FIB cut preparation the complete filling of the pores and the preservation of the percolated metallic network structure within the polymer matrix were proven. Alternatively, the solvent in the pores of a hydrogel was replaced against MMA monomers and subsequent radical polymerization of PMMA was performed. The shape of the monolith remains unchanged throughout the polymerization which underlines the mechanical strength of the metallic NP-based aerogels. The hybridization with functional polymers is assumed to be a general approach albeit individual reaction conditions for each monomer and polymerization process have to be developed.

The processing of multimetallic gels towards functional coatings is an important step with respect to their device integration. Several film preparations methods and film morphologies have been addressed in the chapter. On the one hand transparent thin films of nanochains and network clusters were prepared on glass substrates. In order to enhance the attractive interactions between the glass slide and the metallic nanostructures the glass surface was modified either by esterification with thiol groups and subsequent decoration with Au-NP seeds or by cationic polymers like PDDA. The premodified substrates were immersed in the reaction solution during the hydrogel formation or treated with preformed dispersions of metal nanochains. Moreover, composite multilayer films of Au nanochains and PDDA were prepared by a spray-assisted layer-by-layer deposition approach. Au

nanochain dispersions were prepared either by reduction of Au salt with a low amount of citrate or according to the ion-induced approach by the addition of a limited amount of Ag^+ ions. All described methods succeed in grafting of nanochains and network clusters to the surface of the substrate. Moreover, homogeneous coatings were obtained for PDDA modified glass surfaces coated with preformed nanochains. In the case of the one-step deposition approaches, no measurable electrical conductivity of the coating was obtained and therefore no formation of a percolated network of metal nanochains is assumed. The multilayer film prepared by spray-deposition was further characterized and reveals a sheet resistance of $30\,k\Omega$ and a transmittance of $80\,\%$. Hence, the coating does not meet the requirements for transparent conductive substrates which are suitable for the replacement of ITO. Further efforts are needed to improve percolation of the network in the one-step deposition techniques or interconnection of the metallic structure throughout the multilayers of the composite film.

On the other hand xerogel films with thickness of a few micrometers are in focus of the investigations. They were prepared by ambient drying of gel dispersions either on glass substrates or on glassy carbon electrodes. Even after dispersing the gel in solution and rearrangement of the network during the film formation and drying process no collapse of the porous network or agglomeration of nanowires was observed. Although a fine network of nanowires and an open pore system are depicted in SEM cross section profiles of the xerogel films a certain loss of porosity and pore volume compared to the corresponding aerogels has to be admitted. Nevertheless, for many application fields drying under ambient conditions may already be sufficient since the porosity of the network, the accessibility of the pores and the metallic surface as well as the structure of nanochains is strongly preserved during the ambient drying of micrometer thickness films.

NP-based aerogels from Pt and Pd reveal high performances in electrocatalysis and bioelectrocatalysis. However, the integration of aerogel materials into the electrochemical systems requires harsh methods such as preparation of dispersions by the help of a horn sonicator and drying on the electrode surface under ambient conditions. The TEM analysis of a Pt-Pd aerogel dispersed in water/isoproponal/Nafion reveals preservation of the morphology of nanowires compared to the initial aerogel. Moreover, the surface of a glassy carbon electrode after modification with aerogel dispersion was studied in SEM. The electrode surface is homogeneously covered with gel fragments of various sizes while the porous structure and the coalescence of NPs within the nanochains are retained during the preparation of the electrode. For these reasons, the accessibility of the metallic surface and the advantageous properties of the nanostructure which are important for application in electrocatalysis are ensured.

In addition, physical properties like electrical conductivity and Seebeck coefficients of metallic NP-based gel structures were object of research. Due to their defined macroscopic geometry xerogel films are suitable specimens for determination of electrical resistivity. The sheet resistances were measured by the van der Pauw method and the film thicknesses were determined from profilometer measurements. The specific resistances of the xerogels were calculated from these results to be in the range of 2 to $5\,\Omega\cdot mm^2/m$.

These values are only two orders of magnitude higher compared to the corresponding bulk metals. This display the high electrical conductivity of metallic gels also taking into account the assumed strong enhancement of electron scattering processes in multicrystalline metal nanowires. These low resistances are attributed to the sol-gel preparation technique which provides self-assembly of the NPs and merging of the metallic building blocks and therefore reduces junction resistances. As a result, xerogel films provide porous and at the same time conductive coatings. The determination of Seebeck coefficients was performed for both, xerogel films and aerogel monoliths. Seebeck coefficients of metallic gels are in the order of magnitude of values from corresponding bulk metals. Positive as well as negative values were observed for Pd-containing and Pd-free aerogels, respectively, but correlations to structural features are still under investigation. Although, their high electrical conductivity is favorable, the low Seebeck coefficients of metallic aerogels prevent their use as thermoelectric materials. In order to design high-performance thermoelectric materials the advantageous properties of metallic and semiconductor nanostructures and highly porous aerogels should be combined within one material.

The results of this chapter strongly contribute to the progress of processing NP-based gel networks and handle them in macroscopic dimensions without destroying their structuring on the nanometer scale. A variety of basic approaches for processing of metallic NP-based gels was introduced and examined. Nevertheless, for specific applications still the development of individual processes and parameters are required. The investigation of physical quantities underlines the metallic properties of the material. For example a high charge carrier density is displayed by the high electrical conductivities and low Seebeck coefficients.

Chapter 5.

Summary

New challenges in nanotechnology arise in the assembly of nanoobjects into three-dimensional superstructures, which may carry synergetic properties and open up new application fields. Within this new class of materials nanostructured, porous functional metals are of great interest since they combine high surface area, gas permeability, electrical conductivity, plasmonic behavior and size-enhanced catalytic reactivity. Even though a large variety of preparation pathways for the fabrication of porous noble metals has already been established, several limitations are still to be addressed by research developments.

The new and versatile approach that is presented in this work makes use of a template-free self-assembly process for the fabrication of highly porous, metallic nanostructures. Thereby, nanochains are formed by the controlled coalescence of noble metal NPs in aqueous media and their interconnection and interpenetration leads to the formation of a self-supported network with macroscopic dimensions. Subsequently, the supercritical drying technique is used to remove the solvent from the pores of the network without causing a collapse of the fragile structure. The resulting highly porous, low-weighted, three-dimensional nanostructured solids are named aerogels. The exceptional properties of these materials originate from the conjunction of the unique properties of nanomaterials magnified by macroscale assembly. Moreover, the combination of different metals may lead to synergetic effects regarding for example their catalytic activity. Therefore, the synthesis of multimetallic gels and the characterization of their structural peculiarities are in the focus of the investigations.

In the case of the developed preparation pathways the gelation process starts from preformed, stable colloidal solutions of citrate capped, spherical noble metal (Au, Ag, Pt, Pd) NPs. In order to face various requirements several methods for the initiation of the controlled destabilization and coalescence of the nanosized building blocks were developed and synthesis conditions were optimized, respectively. Multimetallic structures with tunable composition are obtained by mixing different kinds of monometallic NP solutions and performing a joint gel formation. The characterization of the resulting materials by means of electron microscopy reveals the formation of a highly porous network of branched nanochains that provide a polycrystalline nature and diameters in the size range of the initial NPs. Furthermore, synthesis conditions for the spontaneous gel formation of glucose stabilized Au and Pd NPs were investigated.

In order to gain a detailed knowledge of the structural properties of bimetallic aerogel structures a versatile set of characterization techniques was applied. A broad pore size distribution dominated by meso- and macropores and remarkably high inner surface areas were concluded from the N_2 physisorption isotherms and density measurements. As investigated, a specific thermal treatment could be used to tune the ligament size of Au-Ag

aerogels, whereas Au-Pd and Pt-Pd structures provide thermal stability under mild conditions. Further investigations aimed to the enlightenment of the elemental distribution and phase composition within the nanochains of multimetallic gel structures. The different approaches provide complementary and consistent results. Phase analyses based on XRD measurements revealed separated phases of each metal in the case of Ag-Pd and Au-Pd aerogels. They further proved the possibility of temperature induced phase modifications that lead to complete alloying of Au and Pd. In addition, separated domains of Pt and Pd were established from the EXAFS analysis of the corresponding aerogel. STEM EDX high resolution elemental mappings confirmed the separated domains of different metals in the case of Au-Pd and Pt-Pd aerogels. Moreover, a complete interdiffusion and alloy formation of Au and Ag within the corresponding aerogel structure is suggested from STEM EDX results.

Finally, the presented investigations further promote the field of metallic aerogels by addressing the challenging issue of processability and device fabrication. Hybrid materials with organic polymers as well as various kinds of coatings on glass substrates and glassy carbon electrodes were prepared whereas the network structure was preserved throughout all processing steps. Moreover, it was illustrated that the NP-based aerogels carry metallic properties as expressed by their low Seebeck coefficients and high electrical conductivities.

Appendix A.

Experimental section[*]

A.1. Reagents

Tetrachloroauric acid trihydrate ($HAuCl_4 \cdot 3\,H_2O$) (99.9%), chloroplatinic acid hexahydrate ($H_2PtCl_6 \cdot 6\,H_2O$) ($\geq 99.95\,\%$), silver nitrate ($AgNO_3$) (99.9999 %), palladium chloride ($PdCl_2$) (99.999%), nickel(II) nitrate hexahydrate ($Ni(NO_3)_2 \cdot 6\,H_2O$, p.a), sodium citrate (99%), copper(II) nitrate trihydrate ($Cu(NO_3)_2 \cdot 3\,H_2O$, p.a), cellulose (powder, 20 micron), PDDA (20 wt% in water), 4-dimethylaminopyridine (DMAP) (99 %) and APTMS (97 %) were purchased from Sigma-Aldrich. Sodium borohydride ($NaBH_4$) (96 %) received from Fluka. D-glucose (water free) was received from Roth. MMA was purchased from Sigma Aldrich and distilled before use. Rhodamin 6G was bought from Radient dyes Laser. Iron(III) nitrate nonahydrate ($Fe(NO_3)_3 * 9\,H_2O$, p.a), AIBN (> 98 %, p.a.) and acetone ($\geq 99.8\,\%$) were received from Merck. Nafion® perfluorinated ion exchange resin (5 wt% solution in amixture of lower aliphatic alcohols and water) and MPA (< 99 %) were purchased from Aldrich. Solvents were used in p.A. grade and deionized water (MilliQ, $18.2\,\text{M}\Omega$) was used throughout all related experiments.

A.2. Preparation of hydrogels and aerogels

A.2.1. Synthesis of citrate stabilized noble metal NPs

Au NP

All reaction flasks were thoroughly cleaned with aqua regia prior to use. Gold NPs were synthesized in aqueous media at room temperature according to a method adapted from BROWN et al.[192] In a typical synthesis 0.15 mmol of gold(III) chloride trihydrate are dissolved in 500 ml deionized water and stirred in a flask. In a first step 11.6 ml of a sodium citrate solution (1 wt%) are added, followed by a quick injection of 5.8 ml freshly prepared, ice-cold reducing agent solution containing 0.26 mmol of $NaBH_4$ and 0.23 mmol of sodium citrate. After injection of reducing agent the solution turned deep red immediately. The particles show a mean diameter of 4.3($\pm$1) nm and an extinction maximum at 505 to 506 nm.

---

[*]Parts of this section have already been published.[20]

Ag, Pt and Pd NP

All reaction flasks were thoroughly cleaned with aqua regia prior to use. The NPs of silver, platinum and palladium are prepared in aqueous solution at the boiling point. Therefore precursor solution containing the respective metal salt is added to 500 ml of boiling water. Precursor solutions were obtained by dissolving $AgNO_3$ or $H_2PtCl_6 \cdot 6 H_2O$ in pure water and $PdCl_2$ in acid solution. The content of metal in the reaction solution is 0.14 mmol for Ag and Pt but 0.28 mmol in the case of Pd. After 1 minute of stirring 11 ml of a sodium citrate solution (1 wt%) are added. One minute later the freshly prepared, ice-cold reducing agent solution containing 0.11 mmol of $NaBH_4$ and 0.23 mmol of sodium citrate was quickly injected. The solution was kept boiling for another 5 to 10 minutes. Particles with a diameter of 3 to 6 nm (bimodal distribution in the case of Ag NPs with additional particles in the size range from 8 to 15 nm) are obtained by this approach as it was shown in former publications of our group.[26,84,98]

A.2.2. Filter centrifugation

In order to increase the particle concentration of the NP solutions polystyrene centrifuge filters are used (Sartorius, Vivaspin, 20 ml, MWCO 100000 for Au and MWCO 30000 for Ag, Pt and Pd). The centrifuge filters, which are three times washed with deionized water before use, are filled with 20 ml of the NP solution, and put into the centrifuge (3000·g) for two to three minutes in order to reduce the volume to 5 ml. The volume of the NP solution is stepwise reduced from 500 ml to 15 ml in the way described. To minimize the concentration of residual stabilizer and impurities the resulting solution is washed twice by adding 8 times the amount of water and reconcentrating the solution using the centrifuge filter. The final volume of the concentrated and washed colloidal solution is fixed at 10 ml. It should be noted that the centrifugation filter approach allows concentrating by at least a factor of 50 without increasing the ionic strength of the solution. The solutions are filtered with a syringe filter (0.22 μm, PVDF) before further use.

A.2.3. Hydrogel formation by the temperature-controlled approach

For preparation of multimetallic hydrogels the concentrated solutions of NPs were mixed in the desired ratio and shaken for 30 min to ensure complete mixing. In a typical experiment the total volume of the mixed solutions is 1.5 to 2.0 ml and the gel formation takes place at 348 K within several hours. During the gel formation a black monolith is settled down in solution whereas the supernatant becomes colorless. For determining the influence of the temperature on the duration of the gel formation equally prepared samples were stored at 288 K, 294 K, 301 K, 313 K, and 348 K.

A.2.4. Hydrogel formation by the ion-induced approach

For preparation of hydrogels by the ion-induced approach citrate stabilized noble metal NPs were synthesized, concentrated and washed by the use of centrifuge filters as described above. In order to initiate the gel formation solution of 0.2 wt% $AgNO_3$, 0.01 M

Ni(NO$_3$)$_2$, 0.01 M Cu(NO$_3$)$_2$, or 0.01 M Fe(NO$_3$)$_3$ were added stepwise (5 µl or 10 µl) to the NP solution until formation of small agglomerates was observed within several minutes after injection. The final concentration of the transition metal ions in the colloidal solution which is needed to induce the gel formation is typically below 1.5 mM. Some further details on the ion concentration and differences of final concentration for the used transition metal ions are also addressed in Chapter 2.2. For the preparation of bimetallic structures the corresponding NP solutions were mixed before addition of transition metal ions.

A.2.5. Preparation of hydrogels from glucose stabilized NPs

The preparation of nanostructures from glucose stabilized NPs are adopted from the publications of QIN et al.[40,104] but modified in order to fulfill optimal conditions for hydrogel formation. For the preparation of Au network structures first the pH of 80 ml of 0.15 M aqueous solution of β-D-glucose was adjusted to 12.2 by addition of 0.1 M NaOH and stirred for about 20 minutes. In a second step 1.6 ml of 0.05 M aqueous solution of HAuCl$_4$ are added to the reaction flask under stirring. Due to the high concentration of reactants the hydrogel is formed immediately. The reaction can also be performed at lower concentration e.g. 320 µl of 0.05 M HAuCl$_4$ solution are added to 80 ml of 0.03 M glucose solution (pH 12.2) and stirred for another 5 minutes. Here, first color of the solution changes to deep purple and the gel formation is observed after 12 hours.

In order to obtain Pt nanowire networks synthesis conditions are the following: 50 ml of 0.03 M aqueous solution of β-D-glucose containing 0.01 mmol of H$_2$PtCl$_6$ are stirred in an reaction flask for 20 minutes after the pH of solution was adjusted to 9.5 by addition of 0.1 M NaOH. For the reduction of metal ions 170 µl of 0.05 M freshly prepared NaBH$_4$ solution are added and the color of solution turn to brown. These values correspond to a molar ratio [NaBH$_4$]/[Pt^{4+}] of 0.85 which is much lower than described in the publication. After another 2 minutes of stirring the solution is transferred to cylindrical glass ware and stored without shaking until the hydrogel structure settle down on the bottom of the flask. In many cases first a thin, black film is formed which agglomerates to a compact monolith after gently shaking.

A.2.6. Solvent exchange and supercritical drying procedure

Prior to the drying procedure the supernatant of the hydrogel was carefully exchanged against pure acetone for several times. After complete exchange of the solvent the hydrogels were transferred into an autoclave (critical point dryer, 13200J-AB from SPI Supplies) for supercritical CO$_2$ drying. The chamber was flushed with liquid CO$_2$ to exchange the acetone (p $\approx$ 50 bar). After overnight storage of the gels in the autoclave at 15-18 °C the chamber was flushed again. In order to convert the liquid CO$_2$ to the supercritical state the chamber was heated above 31 °C (typically up to 36 °C) accompanied by an increase of the pressure to $\approx$ 80 bar. Finally, the CO$_2$ was slowly discharged by reducing the pressure whilst keeping the temperature constant.

A.3. Preparation of hybrid materials and coatings

A.3.1. Infiltration with organic polymers for preparation of Hybrid materials

For infiltration with methylmethycrylate (MMA) the solvent of an Au-Ag hydrogel was first replaced with acetone and afterwards stepwise replaced with monomer. After complete exchange of solvent with monomer the polymerization was started by the addition of azobisisobutyronitrile (AIBN) with a final concentration of 1 wt%. The radical polymerization occurred within 48 h at 50 °C.

In the case of ethyl cyanoacrylate a small piece of Au-Ag-Pt aerogel sample was soaked with monomer. Air humidity immediately initiates the polymerization. The sample was dried under ambient conditions for several hours before used for the FIB cut preparation.

A.3.2. Modification of glass substrates

Glass substrates were first cleaned by a short treatment in water and acetone in an ultrasonic bath. For decoration of a glass substrate with Au NPs several steps were performed. (1) The substrate is immersed in 3 M KOH for 15 minutes to hydrophilize the surface. Afterward it is rinsed with water carefully. (2) Esterification of the surface is performed in a solution which contains MPA and tetrahydrofuran (volume ratio 1:1) and a small amount of 4-dimethylaminopyridine (DMAP). The substrate is immersed in the solution over night and afterwards rinsed with acetone carefully. (3) Finally the substrate is placed in a highly concentrated Au-NP solution for several hours. After removing from solution and drying the substrate can be used for further preparation of the coating.

In order to premodificate the substrates with PDDA the clean glass slides were immersed in a 0.5 % PDDA solution. In addition the solution provides a 0.1 M NaCl concentration. After 30 minutes the glass slides are removed from the solution and thoroughly rinsed with water before further use.

A.3.3. Preparation of transparent coatings

For preparation of transparent coatings the premodified glass substrates were immersed either in the reaction solution during the hydrogel formation or in a preformed dispersion of nanochains. Nanochains for the coating of PDDA treated substrates were synthesized according to a method described by PEI et al.[106] In order to obtain Au nanochains 20 mg of NaAuCl$_4$ are dissolved in 200 ml of water and heated to 80 °C before 100 µl of 0.1 M sodium citrate solution are added. The solution is kept at 80 °C for 60 minutes before being cooled down to room temperature. Finally a grayish colored solution is obtained. In order to prepare a thin film coating the PDDA modified substrate is placed in the nanochain dispersion for several hours.

For the spray-assisted layer-by-layer deposition Au nanochains were prepared by the ion-induced approach. In order to obtain Au nanochains instead of a compact hydrogel structure the final concentration of Ag$^+$ ions was limited to 0.59 mM. The PDDA solution and the nanochains dispersion were alternately deposited on the surface. Details concerning

the spray-deposition setup, the layer-by-layer deposition and the characterization of the coating can be found elsewhere.[168,169]

A.3.4. Preparation of xerogel films on glass substrates

Glass substrates were prepared by treatment in water and acetone in the ultrasonic bath and dried in an air flow. For the preparation of xerogel films bimetallic hydrogels after acetone exchange were used. The gel was dispersed in solution by short treatment in an ultrasonic bath and the glass substrate was horizontally immersed into the solution in a small vial. The solvent was slowly evaporated without shaking or moving the sample during this time. After complete evaporation of the solvent a homogenous xerogel film was grafted on the substrate.

A.3.5. Preparation of inks and coating of glassy carbon electrodes

1 mg of a Pt_{50}-Pd_{50} aerogel (prepared according to the temperature controlled approach at 75 °C) was spread in 1 ml of solvent which contains 798 µl of water, 200 µl of isopropanol and 2 µl of Nafion®. A horn sonicator (Bandelin SONOPULS HD 2200, equipped with a MS73 tip) was used to disperse the solid aerogel in the solution. After 15 minutes of treatment with 10 % of maximal power a black and clear dispersion was obtained. The freshly prepared ink was used for TEM sample preparation and for modification of the polished glassy carbon electrodes.

A.4. Instruments/preparation of specimens/measurement conditions and parameters

A.4.1. Electron microscopy

Transmission electron microscopy (TEM) was performed on a Zeiss Libra 120 and Libra 200. High Resolution Transmission Electron Microscopy (HRTEM) is performed on a Philips CM 200 FEG/ST-Lorentz 200 kV microscope with field emission gun at the Triebenberg Laboratory for Electron Microscopy and Electron Holography of the TU Dresden. TEM samples are prepared by dispersing a piece of aerogel monolith in methanol by a short sonication step and subsequent drop casting onto a copper grid coated with a thin Formvar-carbon film with subsequent evaporation of the solvent. For the preparation of aqueous samples SiO_2 coated grids or hydrophilised carbon coated grids were applied. Hydrophilisation of the carbon film was achieved by plasma treatment (oxygen plasma, 60 W, 20 s) and the modification was stable for several hours.
STEM imaging and STEM EDX analysis were performed using a Cs probe corrected Titan[3] G2 60-300 electron microscope that is equipped with the ChemiSTEM technology (high-brightness X-FEG electron source in combination with the Super-X EDS detector, which consists of 4 windowless silicon drift detectors). In order to avoid or at least minimize sample damage or influence of the measurement on the elemental distribution, the mappings were obtained at an acceleration voltage of 60 kV and a beam current of about

400 pA. Iterative maps of 512×512 pixels were recorded with a minimal dwell time per pixel of about 16 μs. The quantitative analysis and background correction was performed by use of the mapping tools of Esprit Software. Resolution of the quantitative maps is 0.5 (Au-Ag, Au-Pd) or 1.0 (Pt-Pd). For evaluation of the elemental ratios the following characteristic X-ray emission lines were used: Au M-series and Ag L-series for the Au-Ag sample, Au L-series and Pd L-series for the Au-Pd aerogel, and Pt M-series and Pd L-series in the case of the Pt-Pd aerogel.

During the STEM measurements carbon contaminations of the structure evolve which are attributed to organic impurities caused by the organic stabilizing molecules that are part of the NP synthesis and by the organic solvents that are used to disperse the solid aerogels for TEM sample preparation. These hydrocarbons are destroyed by the electron beam and carbon residues are formed. In general, samples are commonly cleaned by plasma treatment in order to avoid this effect. However, plasma cleaning of the metallic aerogel TEM samples was omitted or shortened to a few seconds in order to avoid changes of the metallic network structure and/or the elemental distribution. However, the reliability of the STEM EDX analysis regarding the noble metals is not affected by the arising carbon contaminations.

SEM imaging and SEM EDX analysis were carried out on a DSM 982 Gemini instrument (Zeiss). The samples for SEM were prepared by deposition of small aerogel pieces on an adhesive carbon film. In order to investigate the surface of glassy carbon after modification with aerogel inks the whole electrode was transferred to the vacuum chamber of the SEM. It was fixed to the sample holder via an adhesive carbon pad and electrical contacts were made by Cu strips.

Focused ion beam preparation was carried out in a Zeiss NEON40 crossbeam SEM/FIB using 100 pA 30 kV Ga$^+$ ion beam.

A.4.2. Thermal treatment of aerogels

For the thermal treatments only solid aerogel samples were used. First, the monoliths or monolith fragments were transferred to a glass tube. In order to create an inert atmosphere the samples were carefully degassed under vacuum and flushed with argon for at least three times prior to heating. During the heating procedure a constant flow of argon to the glass tube was ensured. The samples were heated in a tubular furnace which was stabilized at the final temperature before inserting the sample tube. After finishing the thermal treatment, samples were removed from the furnace and cooled down to room temperature under argon atmosphere.

A.4.3. Thermogravimetric analysis

Thermogravimetric analysis (TGA) was done on NETZSCH STA 409 PC/PG instrument. The samples were put in standard 70 μL α-Al_2O_3 crucibles and degassed prior to heating. The measurements occurred under an argon atmosphere in the temperature range of 25 °C to 1000 °C at a heating rate of 5 °C/min.

A.4.4. N_2 physisorption

Nitrogen physisorption isotherms were acquired at 77 K using a Quantachrome Autosorb 1c apparatus. Prior to the measurement, the samples were degassed in vacuum at 323 K for 24 h. The specific surface area was calculated using the BET equation (p/p_0 = 0.05–0.2). The cumulative pore size distribution was estimated from the desorption branch using BJH theory. Pore volumes were determined at p/p_0 = 0.95 for pores < 40 nm and at p/p_0 = 0.99 for pores < 210 nm.

A.4.5. Powder XRD and Rietveld refinement

For X-ray powder diffraction (XRD), powder samples were fixed as a thin layer on an acetate film. Data were collected in the flat sample transmission mode on a STOE STADI-P powder diffractometer equipped with a 6°-position sensitive detector (PSD) and a Ge(111)-monochromator. All samples were measured with Co $K_{\alpha 1}$-radiation (λ= 1.7903 Å) with a measurement duration of 60 hours. Structure refinements were carried out with FullProf in the program package WinPLOTR[193] according to the Rietveld method.131,132 For the refinements, structure data were used in their standardized setting as provided by the Inorganic Crystal Structure Database.[194] For Pd, Ag, and Au, structure models with the space group (SG) F*m*-3*m* were applied.[195] Same SG was assigned to the found AuPd phase.[196] For Ag_2O a cubic structure model with SG P*n*-3*m*[197] and a tetragonal PdO P42/*mmc*[198] were ascertained. The Pt-Pd aerogel data were fitted with a Pt structure model, SG F*m*-3*m*.[195] The crystallite sizes were refined according to the Y parameter in profile function no.7 (pseudo-Voigt function) in combination with an instrumental resolution file measured with a silicon standard.

A.4.6. Determination of EXAFS spectra and data analysis

X-ray absorption spectroscopy for several Pt-Pd aerogels with different elemental compositions was performed on the X10DA (SuperXAS) beam-line at the Swiss Light Source (SLS) with the storage ring operating at a beam current of 400 mA. The beam-line was equipped with a Si (111) double-crystal monochromator which moved in a continuous mode ("on-the-fly"). 4 mg (or 2 mg in the case of Pt_{80}-Pd_{20}) of the aerogel sample were mixed with 20 mg of cellulose which acts as a binder material. The powder sample was pressed (0.7 − 0.9 bar) to form a pellet with a diameter of 0.5 cm. The XAS spectra were measured in transmission mode by the use of ionization chambers filled with a He/N_2 mixture. The data were collected from 11.46 to 12.48 keV for Pt (Pt L_3-edge 11.565 keV)

and from 24.25 to 25.50 keV for Pd (Pd K-edge 24.350 keV), respectively. The data acquisition of one full EXAFS scan was performed within approx. 15 - 20 min and each measurement was repeated at least two times. To process and analyze the data, Athena and Artemis software which are implemented in FEFF6 and IFEFFIT[199,200] were applied. The following steps of data reduction were adapted: (1) background subtraction and edge-step normalization of the raw data, (2) transformation in k-space and weighting by a factor of 2, (3) Fourier transformation of the k^2-weighted spectra into R-space over a k-range extending from $3 - 15$ Å. Subsequently, a nonlinear least-squares fit was applied to the curves. The k^2-weighted Fourier transformed EXAFS data and the corresponding fits are displayed in Figure 3.9, Figure A.1 and Figure A.2. In order to improve the refinement multi-edge EXAFS fits for Pt and Pd were concurrently performed in the range of approx. $1 - 3$ Å in R-space. Multi-edge fits were performed for a Pt_{50}-Pd_{50} aerogel in the pristine state and after a thermal treatment as well as for a Pt_{20}-Pd_{80} specimen. The characterization of Pt_{80}-Pd_{20} aerogel was performed by the evaluation of the data from the Pt L_3-edge only. The scattering paths for all spectra measured at the Pt edge were calculated using a face-centered cubic (fcc) PtPd structure (space group Fm-3m). Pure Pt and Pd foil were evaluated in order to determine the amplitude reduction factor S_0^2 for Pt and Pd. Assuming a coordination number of 12 the resulting values are 0.83 for Pt and 0.91 for Pd, respectively. The coordination numbers for the Pt-Pd aerogel samples were corrected according to these determined S_0^2 values. Finally the coordination numbers (N), atomic distances (R), degree of disorder (σ^2) were calculated. Moreover, the R-factor (Rf) that expresses the closeness of the fit as well as the energy shift (ΔE_0) were determined to monitor the quality of the fit analysis and the measurement, respectively. The corresponding values are given in Table A.1.

Table A.1.: *R-factor (R_f) and energy shift (ΔE_0) of the EXAFS spectra and fit analyses corresponding to the measurements of Pt-Pd aerogels samples.*

aerogel	R_f	ΔE_0 Pt	ΔE_0 Pt
Pt_{50}-Pd_{50}	0.013	8.8 ± 1.2	-6.7 ± 0.8
Pt_{50}-Pd_{50} 150 °C, 30 min	0.012	7.7 ± 0.8	-7.9 ± 0.7
Pt_{20}-Pd_{80}	0.013	7.9 ± 0.9	-8.1 ± 0.6
Pt_{80}-Pd_{20}	0.004	7.7 ± 0.6	—

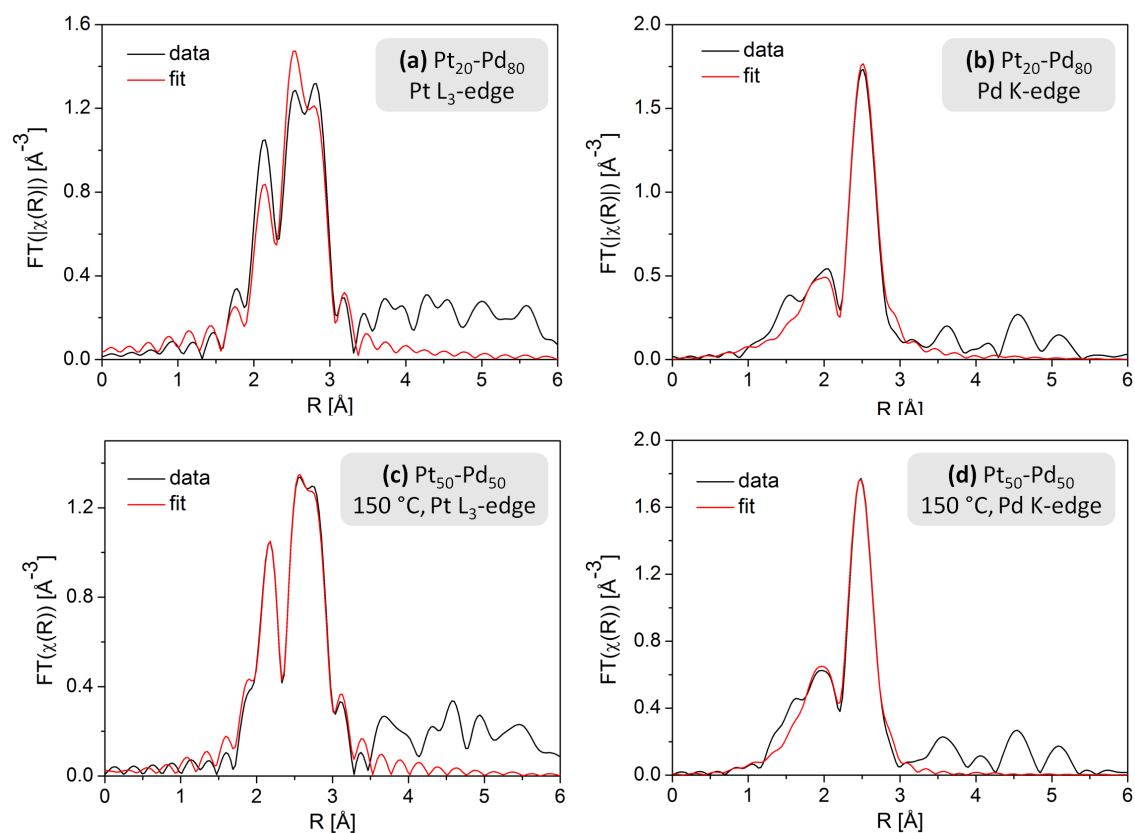***Figure A.1.:*** *k^2-weighted Fourier transformed EXAFS spectra of a Pt_{20}-Pd_{80} aerogel sample (a, b) and of a Pt_{50}-Pd_{50} aerogel after thermal treatment for 30 minutes at 150 °C under inert atmosphere (c, d). Multi-edge fit analyses were performed for these samples.*
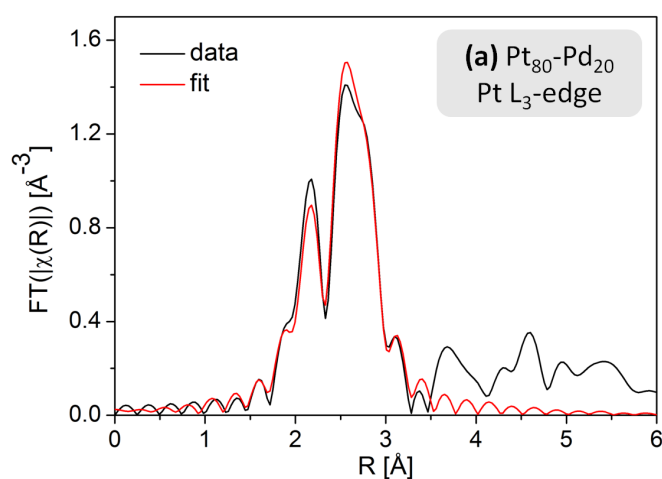

Figure A.2.: *k^2-weighted Fourier transformed EXAFS spectra of a Pt_{80}-Pd_{20} aerogel sample in the energy range of the Pt L_3-edge.*

A.4.7. SERS measurements

The Raman spectra were obtained on a Renishaw RM-2000 Raman microscope using a 532 nm laser. Several concentrations of rhodamine 6G in methanol (minimal concentration 10^{-8} M) were used as test substances. A volume of 4 µl was dropped on the substrate and dried before collection the spectra, respectively.

A.4.8. Van der Pauw measurements

The sheet resistance of xerogel films was measured by a van der Pauw setup.[172,173] It is an appropriate method for determination of the resistance of thin films of arbitrary shape. Four electrical contacts were established at the corners of the coating. Therefore small drops of silver paint were placed on top of the film, directly connected to thin copper wires and finally dried (see Figure A.3). The measurement is performed by applying a current on one side of the sample and measure the voltage between the opposite contacts. For example the resistance named $R_{AB,CD}$ is calculated from voltage between C and D and the corresponding current applied between A and B. All possible combinations are measured and averaged values for the horizontal resistance (R_H) and the vertical resistance (R_V) are calculated by the following equations:

$$R_H = \frac{R_{AB,CD} + R_{BA,CD} + R_{CD,AB} + R_{DC,AB}}{4} \tag{A.1}$$

$$R_V = \frac{R_{AD,BC} + R_{DA,BC} + R_{BC,AD} + R_{CB,AD}}{4} \tag{A.2}$$

For calculation of the specific resistance of the sample the thickness of the film has to be determined. The film thickness was measured by a Veeco Dektak 150 profilometer with a contact pressure of 3 mg. At least three thickness measurements at different positions were averaged in order to calculate the film thickness. In order to consider the irregular geometry of the coating a correction factor f is used which is a function of the ratio R_H/R_V and satisfies the relation

$$\frac{R_H - R_V}{R_H + R_V} = f \cosh^{-1} \left\{ \frac{exp\frac{\ln 2}{f}}{2} \right\} \tag{A.3}$$

For determination of the correction factor at a given R_H/R_V ratio the plot shown in Figure A.3 (c) was used. Finally the specific resistance of the sample was calculated according to

$$\rho = \frac{\pi d}{\ln 2} \frac{(R_H + R_V)}{2} f\left(\frac{R_H}{R_V}\right) \tag{A.4}$$
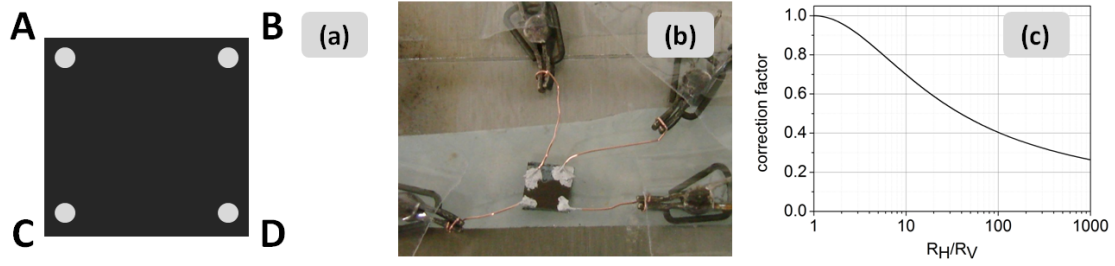
Figure A.3.: *(a) In order to perform van der Pauw measurements four contacts at the periphery of the film are required (b) Xerogel sample placed in the homemade van der Pauw setup. The electrical contacts at the corners of the coating were made from small silver paint droplets and Cu wires. (c) Correction factor f plotted as a function of the R_H/R_V ratio.*

A.4.9. Determination of the Seebeck coefficients

The determination of Seebeck coefficients was performed during a stay at the Cardiff School of Engineering under the supervision of the group of Dr. M. Gao. The setup used for evaluation of Seebeck coefficients of xerogel film is shown in Figure A.4. Electrical contacts were established by conductive probes and a temperature gradient was induced in the sample as one of the probes could be heated by applying a current. Moreover the whole stage can be heated to enable the evaluation of the temperature dependence of the Seebeck coefficient. The temperature gradient of the sample was monitored by an infrared microscope (Infrascope III, Quantum Focus Instruments Corporation). An example of the resulting temperature mappings is shown in Figure A.4 (b). From these data the temperature difference between the two probes as well as the average temperature (mean of the temperatures of the hot and the cold probe) were calculated. Further, the Seebeck voltage was measured between the two conductive tips and the Seebeck coefficient was calculated by

$$\alpha_S = \frac{V_S}{\Delta T} \tag{A.5}$$

For the measurements of the Seebeck coefficients of aerogel monoliths a homemade setup which is schematically depicted in Figure A.5 was used. This equipment uses multifunctional probes which induce the temperature gradient and enable at the same time to measure the temperature as well as the Seebeck voltage of the sample. Thermocouples of Cu and constantan are integrated in the probes in order to measure the temperature by measuring the Seebeck voltages V_{AD} and V_{DF}. Moreover, the sharp probes can be moved discreetly in all three dimensions which allow gently touching of the fragile aerogel samples in order to ensure electrical contact.
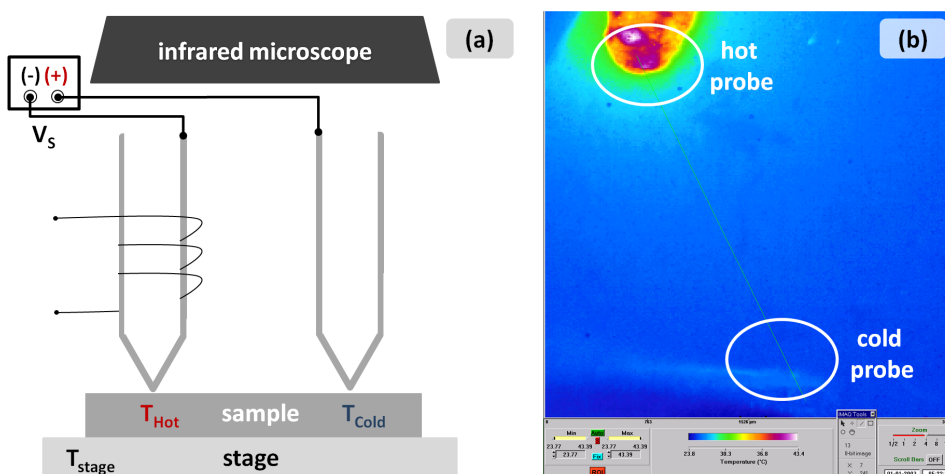
Figure A.4.: *(a) Scheme of the measurement system used for determination of the Seebeck coefficients of xerogel films. The drawing was created in collaboration with S. Gabriel (Physical Chemistry, TU Dresden). (b) Screenshot of the temperature mapping provided by the infrared microscope.*
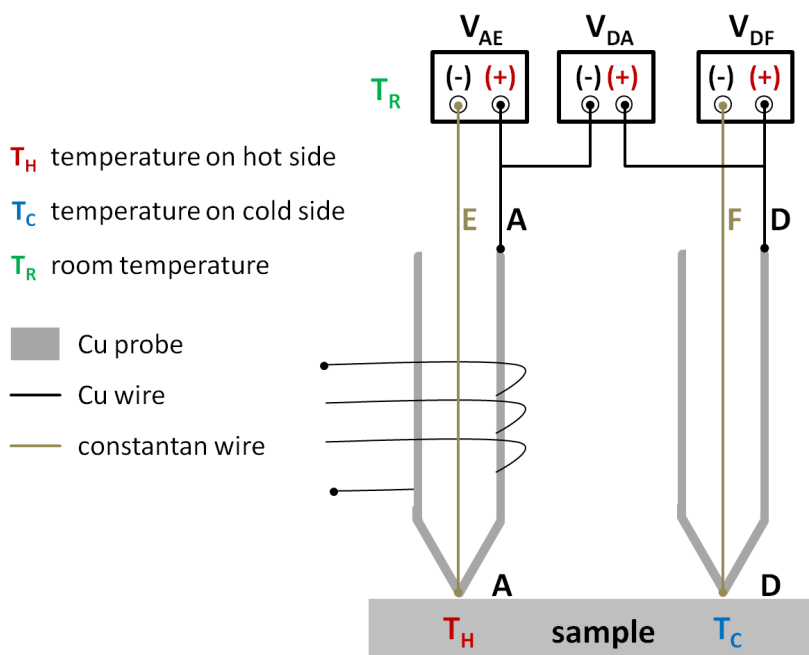

Figure A.5.: *Scheme of the measurement setup which uses multifunctional probes to contact the sample, induce the temperature gradient and measure the temperature as well as the Seebeck voltage of the sample. The drawing was created in collaboration with S. Gabriel (Physical Chemistry, TU Dresden).*

The Seebeck coefficient of the sample has to be calculated by taking into account the following equation and values:

$$\alpha_S = \frac{V_{DA} \cdot 40.6 \frac{\mu V}{K}}{V_{AE} - V_{DF}} + 1.84 \frac{\mu V}{K} \tag{A.6}$$

$$\alpha_{Cu-Constantan} = 40.6 \frac{\mu V}{K} \tag{A.7}$$

$$\alpha_{Cu} = 1.84 \frac{\mu V}{K} \tag{A.8}$$

This setup was applied to investigate the Seebeck coefficient of an Ag-Pt aerogel at several temperature differences and the results are summarized in Table A.2. The measurements of this series can be also combined in order to determine the Seebeck coefficient of the sample. Assuming a stable α_S the voltage between the two probes (V_{DA}) would increase linearly with increasing temperature difference. The experimental data are used to create a linear fitting and the slope of the resulting linear function is equal to α_S(aerogel)- α_S(Cu).

Table A.2.: *Seebeck coefficient of an Ag-Pt aerogel measured at several temperature differences with the help of setup of multifunctional probes.*

ΔT [K]	α_S [μV/K]
2.7	-1.11
9.0	-1.37
12.5	-1.28
21.0	-1.44
28.1	-1.33

The hot probe technique was used to investigate the Seebeck coefficients of several metallic aerogels. The working principle of the setup is depicted in Figure A.6. Also in this case a Cu-constantan thermocouple is used to determine the temperature. The upper Cu probe is gently pressed on the sample to ensure electrical contact. The Seebeck coefficient of the sample is calculated according to:

$$\alpha_S = \frac{V_S}{v_T} \cdot 40.6 \frac{\mu V}{K} \tag{A.9}$$

Figure A.6.: *Scheme of the measurement setup of the hot probe technique. The drawing was created in collaboration with S. Gabriel (Physical Chemistry, TU Dresden).*

Bibliography

[1] R. Feynman, *Eng. Sci.* **1960**, *23*, 22–36.

[2] J. Park, J. Joo, S. G. Kwon, Y. Jang, T. Hyeon, *Angew. Chem. Int. Ed.* **2007**, *46*, 4630–60.

[3] C. Burda, X. Chen, R. Narayanan, M. A. El-Sayed, *Chem. Rev.* **2005**, *105*, 1025–1102.

[4] H. Goesmann, C. Feldmann, *Angew. Chem. Int. Ed.* **2010**, *49*, 1362–1395.

[5] M. D. Bentzon, J. van Wonterghem, S. Mø rup, A. Thölén, C. J. W. Koch, *Philos. Mag. Part B* **1989**, *60*, 169–178.

[6] C. B. Murray, C. R. Kagan, M. G. Bawendi, *Science* **1995**, *270*, 1335–1338.

[7] C. P. Collier, T. Vossmeyer, J. R. Heath, *Annu. Rev. Phys. Chem.* **1998**, *49*, 371–404.

[8] C. B. Murray, C. R. Kagan, M. G. Bawendi, *Annu. Rev. Mater. Sci.* **2000**, *30*, 545–610.

[9] T. Oonishi, S. Sato, H. Yao, K. Kimura, *J. Appl. Phys.* **2007**, *101*, 114314.

[10] J. Kolny, A. Kornowski, H. Weller, *Nano Lett.* **2002**, *2*, 361–364.

[11] R. K. Mallavajula, L. A. Archer, *Angew. Chem. Int. Ed.* **2011**, *50*, 578–580.

[12] L. Wang, L. Xu, H. Kuang, C. Xu, N. A. Kotov, *Acc. Chem. Res.* **2012**, *45*, 1916–1926.

[13] B. C. Tappan, S. A. Steiner III, E. P. Luther, *Angew. Chem. Int. Ed.* **2010**, *49*, 4544–4565.

[14] J. Zhang, C. M. Li, *Chem. Soc. Rev.* **2012**, *41*, 7016–7031.

[15] D. R. Rolison, *Science* **2003**, *299*, 1698–1701.

[16] L. Guczi, *Catal. Today* **2005**, *101*, 53–64.

[17] D. Wang, Y. Li, *Adv. Mater.* **2011**, *23*, 1044–1060.

[18] X. Liu, D. Wang, Y. Li, *Nano Today* **2012**, *7*, 448–466.

[19] C. Zhu, S. Guo, S. Dong, *Adv. Mater.* **2012**, *24*, 2326–2331.

[20] A.-K. Herrmann, P. Formanek, L. Borchardt, M. Klose, L. Giebeler, J. Eckert, S. Kaskel, N. Gaponik, A. Eychmüller, *Chem. Mater.* **2014**, *26*, 1074–1083.

[21] D. Walsh, L. Arcelli, T. Ikoma, J. Tanaka, S. Mann, *Nat. Mater.* **2003**, *2*, 386–390.

[22] F. Khan, M. Eswaramoorthy, C. N. R. Rao, *Solid State Sci.* **2007**, *9*, 27–31.

[23] O. D. Velev, P. M. Tessier, A. M. Lenhoff, E. W. Kaler, *Nature* **1999**, *401*, 548.

[24] H. J. Shin, R. Ryoo, Z. Liu, O. Terasaki, *J. Am. Chem. Soc.* **2001**, *123*, 1246–1247.

[25] D. Wang, H. Luo, R. Kou, M. P. Gil, S. Xiao, V. O. Golub, Z. Yang, C. J. Brinker, Y. Lu, *Angew. Chem. Int. Ed.* **2004**, *116*, 6295–6299.

[26] N. C. Bigall, M. Reitzig, W. Naumann, P. Simon, K.-H. van Pée, A. Eychmüller, *Angew. Chem. Int. Ed.* **2008**, *47*, 7876–7879.

[27] Y. Song, R. M. Garcia, R. M. Dorin, H. Wang, Y. Qiu, E. N. Coker, W. A. Steen, J. E. Miller, J. A. Shelnutt, *Nano Lett.* **2007**, *7*, 3650–3655.

[28] F. Ksar, G. Surendran, L. Ramos, B. Keita, L. Nadjo, E. Prouzet, P. Beaunier, A. Hagège, F. Audonnet, H. Remita, *Chem. Mater.* **2009**, *21*, 1612–1617.

[29] M. Grzelczak, J. Vermant, E. M. Furst, L. M. Liz-Marzán, *ACS Nano* **2010**, *4*, 3591–3605.

[30] R. Klajn, K. J. M. Bishop, M. Fialkowski, M. Paszewski, C. J. Campbell, T. P. Gray, B. A. Grzybowski, *Science* **2007**, *316*, 261–264.

[31] R. Klajn, T. P. Gray, P. J. Wesson, B. D. Myers, V. P. Dravid, S. K. Smoukov, B. A. Grzybowski, *Adv. Funct. Mater.* **2008**, *18*, 2763–2769.

[32] V. Zielasek, B. Jürgens, C. Schulz, J. Biener, M. M. Biener, A. V. Hamza, M. Bäumer, *Angew. Chem. Int. Ed.* **2006**, *45*, 8241–8244.

[33] A. Wittstock, B. Neumann, A. Schaefer, K. Dumbuya, C. Kübel, M. M. Biener, V. Zielasek, H.-P. Steinrück, J. M. Gottfried, J. Biener, A. Hamza, M. Bäumer, *J. Phys. Chem. C* **2009**, *113*, 5593–5600.

[34] Y. Ding, J. Erlebacher, *J. Am. Chem. Soc.* **2003**, *125*, 7772–7773.

[35] H.-J. Jin, X.-L. Wang, S. Parida, K. Wang, M. Seo, J. Weissmüller, *Nano Lett.* **2010**, *10*, 187–94.

[36] B. C. Tappan, M. H. Huynh, M. a. Hiskey, D. E. Chavez, E. P. Luther, J. T. Mang, S. F. Son, *J. Am. Chem. Soc.* **2006**, *128*, 6589–94.

[37] H. Liu, Q. Yang, *J. Mater. Chem.* **2011**, *21*, 11961–11967.

[38] A. Halder, S. Patra, B. Viswanath, N. Munichandraiah, N. Ravishankar, *Nanoscale* **2011**, *3*, 725–730.

[39] P. J. Cappillino, J. D. Sugar, M. a. Hekmaty, B. W. Jacobs, V. Stavila, P. G. Kotula, J. M. Chames, N. Y. Yang, D. B. Robinson, *J. Mater. Chem.* **2012**, *22*, 14013–14022.

[40] G. W. Qin, J. Liu, T. Balaji, X. Xu, H. Matsunaga, Y. Hakuta, L. Zuo, P. Raveendran, *J. Phys. Chem. C* **2008**, *112*, 10352–10358.

[41] K. S. Krishna, C. S. S. Sandeep, R. Philip, M. Eswaramoorthy, *ACS Nano* **2010**, *4*, 2681–2688.

[42] C. Zhu, S. Guo, S. Dong, *Chem. Eur. J.* **2013**, *19*, 1104–1111.

[43] G. W. Nyce, J. R. Hayes, A. V. Hamza, J. H. Satcher, *Chem. Mater.* **2007**, *19*, 344–346.

[44] N. Hüsing, U. Schubert, *Angew. Chem. Int. Ed.* **1998**, *37*, 22–45.

[45] M. A. Aegerter, N. Leventis, M. M. Koebel (Eds.), *Aerogels Handbook*, Springer New York, New York, NY, **2011**.

[46] S. S. Kistler, *Nature* **1931**, *127*, 741.

[47] G. A. Nicolaon, S. J. Teichner, *Bull. Soc. Chim. Fr.* **1968**, *5*, 1900–1906.

[48] B. Heinrichs, F. Noville, J. P. Pirard, *J. Catal.* **1997**, *170*, 366–376.

[49] K. S. Morley, P. Licence, P. C. Marr, J. R. Hyde, P. D. Brown, R. Mokaya, Y. Xia, S. M. Howdle, *J. Mater. Chem.* **2004**, *14*, 1212–1217.

[50] N. Leventis, C. Sotiriou-Leventis, G. Zhang, A. M. M. Rawashdeh, *Nano Lett.* **2002**, *2*, 957–960.

[51] M. A. B. Meador, E. F. Fabrizio, F. Ilhan, A. Dass, G. Zhang, P. Vassilaras, J. C. Johnston, N. Leventis, *Chem. Mater.* **2005**, *17*, 1085–1098.

[52] J. W. Long, D. R. Rolison, *Acc. Chem. Res.* **2007**, *40*, 854–62.

[53] C. A. Morris, *Science* **1999**, *284*, 622–624.

[54] M. L. Anderson, C. A. Morris, R. M. Stroud, C. I. Merzbacher, D. R. Rolison, *Langmuir* **1999**, *15*, 674–681.

[55] A. P. Katsoulidis, J. He, M. G. Kanatzidis, *Chem. Mater.* **2012**, *24*, 1937–1943.

[56] N. Leventis, N. Chandrasekaran, A. G. Sadekar, C. Sotiriou-Leventis, H. Lu, *J. Am. Chem. Soc.* **2009**, *131*, 4576–7.

[57] N. Leventis, N. Chandrasekaran, A. G. Sadekar, S. Mulik, C. Sotiriou-Leventis, *J. Mater. Chem.* **2010**, *20*, 7456.

[58] J. W. Long, M. S. Logan, C. P. Rhodes, E. E. Carpenter, R. M. Stroud, D. R. Rolison, *J. Am. Chem. Soc.* **2004**, *126*, 16879–16889.

[59] J. L. Mohanan, S. L. Brock, *J. Non-Cryst. Solids* **2004**, *350*, 1–8.

[60] J. L. Mohanan, I. U. Arachchige, S. L. Brock, *Science* **2005**, *307*, 397–400.

[61] I. U. Arachchige, J. L. Mohanan, S. L. Brock, *Chem. Mater.* **2005**, *17*, 6644–6650.

[62] A. Eychmüller, *Angew. Chem. Int. Ed.* **2005**, *44*, 4839–4841.

[63] I. U. Arachchige, S. L. Brock, *J. Am. Chem. Soc.* **2006**, *128*, 7964–7971.

[64] I. U. Arachchige, S. L. Brock, *J. Am. Chem. Soc.* **2007**, *129*, 1840–1841.

[65] I. U. Arachchige, S. L. Brock, *Acc. Chem. Res.* **2007**, *40*, 801–809.

[66] S. Bag, P. N. Trikalitis, P. J. Chupas, G. S. Armatas, M. G. Kanatzidis, *Science* **2007**, *317*, 490–493.

[67] S. Bag, M. G. Kanatzidis, *J. Am. Chem. Soc.* **2008**, *130*, 8366–8376.

[68] Q. Yao, I. U. Arachchige, S. L. Brock, *J. Am. Chem. Soc.* **2009**, *131*, 2800–2801.

[69] I. R. Pala, I. U. Arachchige, D. G. Georgiev, S. L. Brock, *Angew. Chem. Int. Ed.* **2010**, *49*, 3661–3665.

[70] L. Korala, L. Li, S. L. Brock, *Chem. Commun.* **2012**, 8523–8525.

[71] L. Korala, S. L. Brock, *J. Phys. Chem. C. Nanomater. Interfaces* **2012**, *116*, 17110–17117.

[72] L. Korala, Z. Wang, Y. Liu, S. Maldonado, S. L. Brock, *ACS Nano* **2013**, *7*, 1215–23.

[73] A. Hitihami-Mudiyanselage, K. Senevirathne, S. L. Brock, *ACS Nano* **2013**, *7*, 1163–70.

[74] S. Ganguly, C. Zhou, D. Morelli, J. Sakamoto, S. L. Brock, *J. Phys. Chem. C* **2012**, *116*, 17431–17439.

[75] N. Gaponik, A. Wolf, R. Marx, V. Lesnyak, K. Schilling, A. Eychmüller, *Adv. Mater.* **2008**, *20*, 4257–4262.

[76] S.-H. Jeong, J. W. Lee, D. Ge, K. Sun, T. Nakashima, S. I. Yoo, A. Agarwal, Y. Li, N. a. Kotov, *J. Mater. Chem.* **2011**, *21*, 11639–11643.

[77] V. Lesnyak, S. V. Voitekhovich, P. N. Gaponik, N. Gaponik, A. Eychmüller, *ACS Nano* **2010**, *4*, 4090–4096.

[78] A. Wolf, V. Lesnyak, N. Gaponik, A. Eychmüller, *J. Phys. Chem. Lett.* **2012**, *3*, 2188–2193.

[79] J. Yuan, N. Gaponik, A. Eychmüller, *Anal. Chem.* **2012**, *84*, 5047–5052.

[80] J. Yuan, D. Wen, N. Gaponik, A. Eychmüller, *Angew. Chem. Int. Ed.* **2013**, *52*, 976–979.

[81] V. Lesnyak, A. Wolf, A. Dubavik, L. Borchardt, S. V. Voitekhovich, N. Gaponik, S. Kaskel, A. Eychmüller, *J. Am. Chem. Soc.* **2011**, *133*, 13413–13420.

[82] T. Hendel, V. Lesnyak, L. Kühn, A.-k. Herrmann, N. C. Bigall, L. Borchardt, S. Kaskel, N. Gaponik, A. Eychmüller, *Adv. Funct. Mater.* **2013**, *23*, 1903–1911.

[83] N. Gaponik, A.-K. Herrmann, A. Eychmüller, *J. Phys. Chem. Lett.* **2012**, *3*, 8–17.

[84] N. C. Bigall, A.-K. Herrmann, M. Vogel, M. Rose, P. Simon, W. Carrillo-Cabrera, D. Dorfs, S. Kaskel, N. Gaponik, A. Eychmüller, *Angew. Chem. Int. Ed.* **2009**, *48*, 9731–9734.

[85] N. C. Bigall, A. Eychmüller, *Phil. Trans. R. Soc. A* **2010**, *368*, 1385–1404.

[86] A.-K. Herrmann, N. C. Bigall, L. Lu, A. Eychmüller in *Complex-shaped Met. Nanoparticles*, T. K. Sau, A. L. Rogach (Eds.), WILEY-VCH Verlag & Co. KGaA, Weinheim, **2012**, pp. 339–360.

[87] K. G. S. Ranmohotti, X. Gao, I. U. Arachchige, *Chem. Mater.* **2013**, *25*, 3528–3534.

[88] J. Biener, A. Wittstock, L. A. Zepeda-Ruiz, M. M. Biener, V. Zielasek, D. Kramer, R. N. Viswanath, J. Weissmüller, M. Bäumer, A. V. Hamza, *Nat. Mater.* **2009**, *8*, 47–51.

[89] A. Mills, *Platin. Met. Rev.* **2007**, *51*, 52–52.

[90] W. Liu, A.-K. Herrmann, D. Geiger, L. Borchardt, F. Simon, S. Kaskel, N. Gaponik, A. Eychmüller, *Angew. Chem. Int. Ed.* **2012**, *51*, 5743–5747.

[91] D. Wen, A.-K. Herrmann, L. Borchardt, F. Simon, W. Liu, S. Kaskel, A. Eychmüller, *J. Am. Chem. Soc.* **2014**, *136*, 2727–30.

[92] A.-K. Herrmann, W. Liu, N. Gaponik, N.-C. Bigall, A. Eychmüller, *ECS Trans.* **2013**, *45*, 149–154.

[93] C. Zhu, D. Wen, M. Oschatz, M. Holzschuh, W. Liu, A.-K. Herrmann, F. Simon, S. Kaskel, A. Eychmüller, *submitted* **2014**.

[94] W. Liu, P. Rodriguez, L. Borchardt, A. Foelske, J. Yuan, A.-K. Herrmann, D. Geiger, Z. Zheng, S. Kaskel, N. Gaponik, R. Kötz, T. J. Schmidt, A. Eychmüller, *Angew. Chem. Int. Ed.* **2013**, *52*, 9849–52.

[95] D. Wen, W. Liu, A.-K. Herrmann, A. Eychmüller, *Chem. - A Eur. J.* **2014**, 1–7.

[96] A.-K. Herrmann, *Bachelor thesis: Synthese und Charakterisierung bimetallischer Aerogele aus Edelmetallnanopartikeln*, TU Dresden, **2008**.

[97] A.-K. Herrmann, *Master thesis: Darstellung und Untersuchung der Eigenschaften sowie Anwendungsmöglichkeiten ungeordneter, poröser Strukturen aus Edelmetallnanopartikeln*, TU Dresden, **2010**.

[98] A. Jantschke, A.-K. Herrmann, V. Lesnyak, A. Eychmüller, E. Brunner, *Chem. Asian J.* **2012**, *7*, 85–90.

[99] P. H. Tewari, A. J. Hunt, K. D. Lofftus, *Mater. Lett.* **1985**, *3*, 363–367.

[100] R. Ferrando, J. Jellinek, R. L. Johnston, *Chem. Rev.* **2008**, *108*, 845–910.

[101] W. Yu, M. D. Porosoff, J. G. Chen, *Chem. Rev.* **2012**, *112*, 5780–817.

[102] C.-J. Zhong, J. Luo, B. Fang, B. N. Wanjala, P. N. Njoki, R. Loukrakpam, J. Yin, *Nanotechnology* **2010**, *21*, 062001.

[103] M. Liu, P. Guyot-Sionnest, *J. Phys. Chem. B* **2005**, *109*, 22192–22200.

[104] G. W. Qin, W. Pei, X. Ma, X. Xu, Y. Ren, W. Sun, L. Zuo, *J. Phys. Chem. C* **2010**, *114*, 6909–6913.

[105] G. Ramanath, J. D'Arcy-Gall, T. Maddanimath, A. V. Ellis, P. G. Ganesan, R. Goswami, A. Kumar, K. Vijayamohanan, *Langmuir* **2004**, *20*, 5583–5587.

[106] L. Pei, K. Mori, M. Adachi, *Langmuir* **2004**, *20*, 7837–7843.

[107] B.-K. Pong, H. I. Elim, J.-X. Chong, W. Ji, B. L. Trout, J.-Y. Lee, *J. Phys. Chem. C* **2007**, *111*, 6281–6287.

[108] H. Ataee-Esfahani, N. Fukata, Y. Yamauchi, *Chem. Lett.* **2010**, *39*, 372–373.

[109] J. Chen, B. Shen, G. Qin, X. Hu, L. Qian, Z. Wang, S. Li, Y. Ren, L. Zuo, *J. Phys. Chem. C* **2012**, *116*, 3320–3328.

[110] H. Yu, S. L. Brock, *ACS Nano* **2008**, *2*, 1563–1570.

[111] A. Pavlišič, P. Jovanovič, V. S. Šelih, M. Šala, N. Hodnik, S. Hočevar, M. Gaberšček, *Chem. Commun. (Camb).* **2014**, *50*, 3732–4.

[112] T. Schmidt, U. Paulus, H. Gasteiger, R. Behm, *J. Electroanal. Chem.* **2001**, *508*, 41–47.

[113] T. J. Schmidt, *ECS Trans.* **2012**, *45*, 3–14.

[114] A. Rabis, P. Rodriguez, T. J. Schmidt, *ACS Catal.* **2012**, *2*, 864–890.

[115] R. Loukrakpam, J. Luo, T. He, Y. Chen, Z. Xu, P. N. Njoki, B. N. Wanjala, B. Fang, D. Mott, J. Yin, J. Klar, B. Powell, C.-J. Zhong, *J. Phys. Chem. C* **2011**, *115*, 1682–1694.

[116] S. Gabriel, Ph.D. thesis, TU Dresden, **2013**.

[117] F. Rouquerol, J. Rouquerol, K. S. W. Sing, *Adsorption by Powders & Porous Solids*, Academic Press, San Diego, **1998**.

[118] K. S. W. Sing, D. H. Everett, R. A. W. Haul, L. Moscou, R. A. Pierotti, J. Rouquerol, T. Siemieniewska, *Pure Appl. Chem.* **1985**, *57*, 603–619.

[119] E. P. Barrett, L. G. Joyner, P. P. Halenda, *J. Am. Chem. Soc.* **1951**, *73*, 373–380.

[120] M. Thommes, *Chemie Ing. Tech.* **2010**, *82*, 1059–1073.

[121] P. I. Ravikovitch, A. V. Neimark, *Langmuir* **2006**, *22*, 11171–9.

[122] S. Brunauer, P. H. Emmet, F. Teller, *J. Am. Chem. Soc.* **1938**, *60*, 309–319.

[123] J. L. Mohanan, S. L. Brock, *J. Sol-Gel Sci. Technol.* **2006**, *40*, 341–350.

[124] P. W. Atkins, *Physikalische Chemie 3rd ed.*, *Vol. 3*, WILEY-VCH Verlag GmbH, Weinheim, **2001**.

[125] L. Vegard, *Zeitschrift für Phys.* **1921**, *5*, 17–26.

[126] W. Kleber, H.-J. Bautsch, J. Bohm, *Einführung in die Kristallographie*, Verl. Technik, Berlin, **1990**.

[127] R. J. D. Tilley, *Understanding solids*, John Wiley & Sons, Ltd, Chichester, UK, **2004**.

[128] P. Scherrer, *Nachrichten von der Gesellschaft der Wissenschaften zu Göttingen, Math. Klasse* **1918**, *1918*, 98–100.

[129] J. I. Langford, A. J. C. Wilson, *J. Appl. Crystallogr.* **1978**, *11*, 102–113.

[130] H. M. Rietveld, *J. Appl. Crystallogr.* **1969**, *2*, 65–71.

[131] L. B. McCusker, R. B. Von Dreele, D. E. Cox, D. Louër, P. Scardi, *J. Appl. Crystallogr.* **1999**, *32*, 36–50.

[132] R. E. Schaak, A. K. Sra, B. M. Leonard, R. E. Cable, J. C. Bauer, Y.-F. Han, J. Means, W. Teizer, Y. Vasquez, E. S. Funck, *J. Am. Chem. Soc.* **2005**, *127*, 3506–3515.

[133] Z. Wang (Ed.), *Characterization of Nanophase Materials*, WILEY-VCH Verlag GmbH, Weinheim, **2000**.

[134] A. Frenkel, *Zeitschrift für Krist.* **2007**, *222*, 605–611.

[135] A. E. Russell, A. Rose, *Chem. Rev.* **2004**, *104*, 4613–35.

[136] J. Cowley, *Phys. Rev.* **1950**, *77*, 669–675.

[137] J. Cowley, *Phys. Rev.* **1960**, *120*, 1648–1657.

[138] J. Cowley, *Phys. Rev.* **1965**, *138*, A1384–A1389.

[139] A. I. Frenkel, Q. Wang, S. I. Sanchez, M. W. Small, R. G. Nuzzo, *J. Chem. Phys.* **2013**, *138*, 064202.

[140] R. Wyckoff, *Crystal structures Vol.1 2nd ed.*, Interscience Publisher, New York, **1963**.

[141] M. Klimenkov, S. Nepijko, H. Kuhlenbeck, M. Bäumer, R. Schlögl, H.-J. Freund, *Surf. Sci.* **1997**, *391*, 27–36.

[142] Y. Sun, A. I. Frenkel, R. Isseroff, C. Shonbrun, M. Forman, K. Shin, T. Koga, H. White, L. Zhang, Y. Zhu, M. H. Rafailovich, J. C. Sokolov, *Langmuir* **2006**, *22*, 807–16.

[143] P. Hawkes, J. Spence (Eds.), *Science of Microscopy*, Springer Science+ Business Media, New York, **2007**.

[144] D. William, C. Carter, *Transmission Electron Microscopy: A Textbook for Material Science 2nd ed.*, Springer Science+ Business Media, New York, **2009**.

[145] J. Thomas, Gemming T., *Analytische Transmissionelektronenmikroskopie*, Springer-Verlag, Wien, **2013**.

[146] S. Utsunomiya, R. C. Ewing, *Environ. Sci. Technol.* **2003**, *37*, 786–791.

[147] D. Wang, A. Villa, F. Porta, L. Prati, D. Su, *J. Phys. Chem. C* **2008**, *112*, 8617–8622.

[148] W. He, X. Wu, J. Liu, X. Hu, K. Zhang, S. Hou, W. Zhou, S. Xie, *Chem. Mater.* **2010**, *22*, 2988–2994.

[149] H. Shi, L. Zhang, W. Cai, *J. Appl. Phys.* **2000**, *87*, 1572.

[150] Q. Zhang, J. Y. Lee, J. Yang, C. Boothroyd, J. Zhang, *Nanotechnology* **2007**, *18*, 245605.

[151] T. Shibata, B. A. Bunker, Z. Zhang, D. Meisel, C. F. Vardeman II, J. D. Gezelter, *J. Am. Chem. Soc.* **2002**, *124*, 11989–11996.

[152] G. Ouyang, X. Tan, C. Wang, G. Yang, *Chem. Phys. Lett.* **2006**, *420*, 65–70.

[153] R. Seshadri, S. L. Brock, A. Ramirez, M. Subramanian, M. E. Thompson, *MRS Bull.* **2012**, *37*, 682–690.

[154] N. Leventis, *Acc. Chem. Res.* **2007**, *40*, 874–84.

[155] D. S. Hecht, L. Hu, G. Irvin, *Adv. Mater.* **2011**, *23*, 1482–513.

[156] J. Zhu, B. S. Shim, M. Di Prima, N. a. Kotov, *J. Am. Chem. Soc.* **2011**, *133*, 7450–60.

[157] D. S. Hecht, A. M. Heintz, R. Lee, L. Hu, B. Moore, C. Cucksey, S. Risser, *Nanotechnology* **2011**, *22*, 169501.

[158] X. Wang, L. Zhi, K. Mullen, *Nano Lett.* **2008**, *8*, 323–327.

[159] J. Meiss, M. K. Riede, K. Leo, *Appl. Phys. Lett.* **2009**, *94*, 13303.

[160] S. Kirchmeyer, K. Reuter, *J. Mater. Chem.* **2005**, *15*, 2077.

[161] Y. Zhou, F. Zhang, K. Tvingstedt, S. Barrau, F. Li, W. Tian, O. Inganäs, *Appl. Phys. Lett.* **2008**, *92*, 233308.

[162] S. De, T. M. Higgins, P. E. Lyons, E. M. Doherty, P. N. Nirmalraj, W. J. Blau, J. J. Boland, J. N. Coleman, *ACS Nano* **2009**, *3*, 1767–1774.

[163] V. Scardaci, R. Coull, P. E. Lyons, D. Rickard, J. N. Coleman, *Small* **2011**, *7*, 2621–8.

[164] A. R. Rathmell, B. J. Wiley, *Adv. Mater.* **2011**, *23*, 4798–803.

[165] C. Sachse, N. Weiß, N. Gaponik, L. Müller-Meskamp, A. Eychmüller, K. Leo, *Adv. Energy Mater.* **2014**, *4*, DOI: 10.1002/aenm.201300737.

[166] P. E. Lyons, S. De, J. Elias, M. Schamel, L. Philippe, A. T. Bellew, J. J. Boland, J. N. Coleman, *J. Phys. Chem. Lett.* **2011**, *2*, 3058–3062.

[167] R. Chen, S. R. Das, C. Jeong, M. R. Khan, D. B. Janes, M. a. Alam, *Adv. Funct. Mater.* **2013**, *23*, 5150–5158.

[168] P. Mundra, Ph.D. thesis, TU Dresden, **2013**.

[169] P. Mundra, T. Otto, N. Gaponik, A. Eychmüller, *Rev. Sci. Instrum.* **2013**, *84*, 074101.

[170] K. Kneipp, H. Kneipp, J. Kneipp, *Acc. Chem. Res.* **2006**, *39*, 443–50.

[171] W. E. Smith, *Chem. Soc. Rev.* **2008**, *37*, 955–64.

[172] L. van der Pauw, *Philips Res. Rep.* **1958**, *13*, 1–9.

[173] L. van der Pauw, *Philips Tech. Rev.* **1958**, *20*, 220–224.

[174] S. Nazarpour, M. Chaker, *Thin Solid Films* **2012**, *520*, 4812–4815.

[175] A. Mayadas, M. Shatzkes, *Phys. Rev. B* **1970**, *1*, 1382–1389.

[176] A. Zabet-Khosousi, A.-A. Dhirani, *Chem. Rev.* **2008**, *108*, 4072–124.

[177] C. Suryanarayana, *Int. Mater. Rev.* **1995**, *40*, 41–64.

[178] Y. Liu, Y. Wang, R. O. Claus, *Chem. Phys. Lett.* **1998**, *298*, 315–319.

[179] J. M. Wessels, H.-G. Nothofer, W. E. Ford, F. von Wrochem, F. Scholz, T. Voss-meyer, A. Schroedter, H. Weller, A. Yasuda, *J. Am. Chem. Soc.* **2004**, *126*, 3349–56.

[180] M. D. Musick, C. D. Keating, L. A. Lyon, S. L. Botsko, D. J. Pena, W. D. Holliway, T. M. McEvoy, J. N. Richardson, M. J. Natan, *Chem. Mater.* **2000**, *12*, 2869–2881.

[181] W. Zeier, M. Panthöfer, J. Janek, W. Tremel, *Chemie unserer Zeit* **2011**, *45*, 188–200.

[182] S. Kasap, *Principles of Electronic Materials and Devices 3rd ed.*, McGraw-Hill Science/Engineering/Math, **2005**.

[183] W. M. N. W. Jaafar, J. E. Snyder, G. Min, *Rev. Sci. Instrum.* **2013**, *84*, 054903.

[184] J. García-Cañadas, G. Min, *Rev. Sci. Instrum.* **2014**, *85*, 043906.

[185] Y. Gogotsi (Ed.), *Nanomaterials Handbook*, CRC Press, **2006**.

[186] L. Hicks, M. Dresselhaus, *Phys. Rev. B* **1993**, *47*, 12727–12731.

[187] M. S. Dresselhaus, G. Chen, M. Y. Tang, R. G. Yang, H. Lee, D. Z. Wang, Z. F. Ren, J. P. Fleurial, P. Gogna, *Adv. Mater.* **2007**, *19*, 1043–1053.

[188] J. R. Sootsman, D. Y. Chung, M. G. Kanatzidis, *Angew. Chemie* **2009**, *48*, 8616–39.

[189] M. G. Kanatzidis, *Chem. Mater.* **2010**, *22*, 648–659.

[190] S. Ganguly, C. Zhou, D. Morelli, J. Sakamoto, S. L. Brock, *J. Phys. Chem. C* **2012**, *116*, 17431–17439.

[191] D. Rowe (Ed.), *Handbook of thermoelectrics*, CRC Press, **1995**.

[192] K. R. Brown, D. G. Walter, M. J. Natan, *Chem. Mater* **2000**, *12*, 306–313.

[193] T. Roisnel, J. Rodríquez-Carvajal, *Mater. Sci. Forum* **2001**, *378-381*, 118–123.

[194] R. Allmann, R. Hinek, *Acta Crystallogr. Sect. A* **2007**, *63*, 412–417.

[195] E. A. Owen, E. L. Yates, *Phil. Mag. Ser. 7* **1933**, *15*, 472–488.

[196] Y. C. Venudhar, L. Iyengar, K. V. K. Rao, *J. Less-Common Met.* **1978**, *58*, 55–60.

[197] P. Niggli, *Z. Krist.* **1922**, *57*, 253–299.

[198] W. J. Moore, L. Pauling, *J. Am. Chem. Soc.* **1941**, *63*, 1392–1394.

[199] M. Newville, *J. Synchrotron Radiat.* **2001**, *8*, 96–100.

[200] B. Ravel, M. Newville, *J. Synchrotron Radiat.* **2005**, *12*, 537–41.

Danksagung

thaltes an der AGH in Krakau sowie bei Prof. Aleksandra Czyrska-Filemonowicz für die Unterstützung dieser Zusammenarbeit. Vielfacher Dank geht zudem an die Mitarbeiter des Arbeitskreises von Dr. Min Gao an der Cardiff School of Engineering, ins besondere an Dr. Jorge García-Cañadas für seine intensive Betreuung und Hilfe bei der Messung von Seebeck Koeffizienten an metallischen Aerogelen.

Aufrichtigen Dank möchte ich auch an Jan Poppe für seine detaillierte und geduldige Hilfe bei meinen ersten Schritten in Sachen Elektrochemie aussprechen. Ich bedanke mich außerdem bei Dr. Paul Mundra für die Herstelllung und Charakterisierung von Schichten mit Hilfe des Sprühverfahrens, bei Matthias Werheid für die Herstellung von Palladiumnanopartikeln mittels keimbasierten Wachstums, bei Stefan Klosz für die Durchführung der Raman Messungen sowie bei Tobias Günther für die Einweisung am Profilometer. Zudem möchte ich mich bei meinen SHK- und Bachelorstudenten Bettina Mamitzsch und Sascha Voigt für ihre engagierte Arbeit bedanken. Außerdem möchte ich mich bei allen fleißigen Korrekturlesern dieser Arbeit für die vielen hilfreichen Hinweise und Korrekturen bedanken.

Mein besonderer Dank gilt meinen Kollegen auf dem Gebiet der Aerogele. Ich danke euch für zahllose ergiebige Diskussionen, den regen Gedankenaustausch und nicht zuletzt für die vielen gemeinsamen Publikationen. Besonders bedanken möchte ich mich hier bei Dr. Wei Liu, Dr. Dan Wen, Thomas Hendel und Dr. Chengzhou Zhu.
Ganz ohne Frage bedanke ich mich außerdem bei dem gesamten Arbeitskreis für Physikalische Chemie. Es ist mir eine Freude mit so vielen fröhlichen, engagierten und hilfsbereiten Kollegen zusammenzuarbeiten.

Aus tiefstem Herzen möchte ich mich auch bei meinen Kollegen und Freunden Susi, Steffi, Lydia, Jan und Gordon bedanken. Ich habe mit euch in den letzten Jahren nicht nur tolle Forschungsideen, Büroräume, Dienstreisen und viele Kannen Kaffee geteilt, sondern auch viele fröhliche, gemeinsame Stunden verbracht, die ich auf keinen Fall missen möchte. Ich danke euch sehr für den Zuspruch und die Motivation in den letzten Monaten und wünsche euch allen bestes Gelingen bei der Verwirklichung eurer beruflichen und privaten Ziele.

Zu meinem großen Glück habe ich aber auch viele Freunde außerhalb des Erich-Müller-Baus, bei denen ich mich an dieser Stelle für zahlreiche entspannte, spannende und fröhliche Erlebnisse bedanken möchte. Mein tiefster Dank für viele tolle gemeinsame Stunden, Urlaubstage und eine unvergessliche WG-Zeit richtet sich dabei vor allem an meine Mädels Nadja, Nicole und an die allerallerbeste Kerstin.

Mein größter Dank gebührt jedoch den wichtigsten Menschen in meinem Leben – meinem Marcel, meinen Eltern und meiner Familie. Ich danke euch aus tiefstem Herzen dafür, dass ihr mich unterstützt wo immer ihr nur könnt, an mich glaubt, mir stets den Rücken freihaltet und mein sicherer Hafen seid. Ich bin sehr glücklich und dankbar dafür, dass es euch gibt.

Erklärung

Hiermit versichere ich, dass ich die vorliegende Arbeit ohne unzulässige Hilfe Dritter und ohne Benutzung anderer als der angegebenen Hilfsmittel angefertigt habe; die aus fremden Quellen direkt oder indirekt übernommenen Gedanken sind als solche kenntlich gemacht. Die Arbeit wurde bisher weder im Inland noch im Ausland in gleicher oder ähnlicher Form einer anderen Prüfungsbehörde vorgelegt.

Diese Dissertation wurde an der Professur für Physikalische Chemie der Fachrichtung Chemie & Lebensmittelchemie der Fakultät Mathematik und Naturwissenschaften an der Technischen Universität Dresden unter wissenschaftlicher Betreuung von Prof. Dr. rer. nat. habil. Alexander Eychmüller angefertigt. Ich versichere weiterhin, dass bislang keine Promotionsverfahren stattgefunden haben.

Ich erkenne die Promotionsordnung der Fakultät Mathematik und Naturwissenschaften an der Technischen Universität Dresden in der Fassung vom 23.02.2011 an.

Dresden, den

Anne-Kristin Herrmann